



 **Universität Trier**

FACHBEREICH VI, GEOGRAPHIE/GEOWISSENSCHAFTEN

FACH UMWELTMETEOROLOGIE

# Diplomarbeit

IM STUDIENGANG ANGEWANDTE PHYSISCHE GEOGRAPHIE

## Quantitative characterisation of sea ice melt stages in the Arctic by means of airborne photographs

*Vorgelegt von:*

**Pascal Schwarz**

Matrikelnummer: 888254

Im Doerrengarten 14, 66453 Herbitzheim

*Eingereicht am:*

06.03.2013

*Gutachter:*

**Univ. Prof. Dr. Günther Heinemann,**

Fach Umweltmeteorologie, Universität Trier

**Univ. Prof. Dr. Markus Casper,**

Fach Physische Geographie, Universität Trier



# Erklärung zur Diplomarbeit

Hiermit erkläre ich, dass ich die Diplomarbeit selbständig verfasst und keine anderen als die angegebenen Quellen und Hilfsmittel benutzt und die aus fremden Quellen direkt oder indirekt übernommenen Gedanken als solche kenntlich gemacht habe.

Die Diplomarbeit habe ich bisher keinem anderen Prüfungsamt in gleicher oder vergleichbarer Form vorgelegt. Sie wurde bisher auch nicht veröffentlicht.

---

Ort, Datum

---

Unterschrift



## **Abstract**

During the melt season, the surface conditions of the Arctic sea ice cover change enormously. The uniform high reflective winter surface transforms to a heterogeneous compound of several surface classes. This change is associated with a strong decrease of the surface albedo, caused by the melting snow cover, the formation of melt ponds and the increase of open water fraction. The goal of this work is to classify images from the MELTEX 2008, NOGRAM 2011 and TIFAX 2010 flight campaigns to determine melt pond parameters, such as concentration, size, size distribution, density, density distribution, shape and shape distribution. These are important quantities for the sea ice atmosphere interaction. A further objective is to evaluate the broadband albedo measurements of the MELTEX campaign. Overall the work gives a quantitative description of the sea ice melt stages by means of the evaluated quantities mentioned above.



## **Zusammenfassung**

Das arktische Meereis unterliegt starken Veränderungen der Oberflächenbeschaffenheit während der Schmelzsaison. Die einheitliche stark reflektierende Oberfläche des Winters wandelt sich zu einem heterogenen Mix aus vielen Oberflächenklassen, was einen starken Abfall der Oberflächenalbedo zur Folge hat. Hierfür verantwortlich sind die schmelzende Schneedecke, die Bildung von Schmelztümpeln auf dem Eis und der Anstieg der offenen Wasserflächen zwischen dem Eis. Ein Ziel der Arbeit ist die Bilderauswertung der Flugkampagnen MELTEX 2008, NOGRAM 2011 und TIFAX 2010 um die verschiedenen Schmelztümpelparameter, wie zum Beispiel Konzentration, Größe, Größenverteilung, Dichte, Dichteverteilung, Form und Formverteilung bestimmen zu können. Diese sind wichtige Größen bei der Wechselwirkung zwischen Meereis und Atmosphäre. Eine weitere Aufgabe ist die Auswertung der Breitbandalbedo Daten der MELTEX Kampagne. Das Hauptziel der Arbeit ist die quantitative Beschreibung der Meereisschmelzphasen mit Hilfe der oben genannten Größen.





# Contents

<b>1</b>	<b>Introduction</b>	<b>1</b>
<b>2</b>	<b>Data and methods</b>	<b>13</b>
2.1	Data description . . . . .	13
2.1.1	MELTEX 2008 . . . . .	13
2.1.2	NOGRAM 2011 . . . . .	16
2.1.3	TIFAX 2010 . . . . .	19
2.2	Data processing . . . . .	22
2.2.1	Preselection of the aerial photographs . . . . .	22
2.2.2	Image classification . . . . .	23
2.2.3	Quality assessment . . . . .	27
2.2.4	Survey of the melt ponds . . . . .	28
2.2.5	Albedo measurements . . . . .	30
<b>3</b>	<b>Results</b>	<b>33</b>
3.1	Image classification . . . . .	33
3.2	Survey of the melt ponds . . . . .	46
3.2.1	Melt pond concentration . . . . .	48
3.2.2	Melt pond size . . . . .	49
3.2.3	Melt pond size distribution . . . . .	49
3.2.4	Melt pond density . . . . .	53
3.2.5	Melt pond density distribution . . . . .	54
3.2.6	Melt pond shape . . . . .	55
3.2.7	Melt pond shape distribution . . . . .	57
3.3	Albedo measurements . . . . .	59
3.4	Quality assessment . . . . .	64
3.4.1	Error calculation . . . . .	64

3.4.2	Geometric Distortion . . . . .	65
<b>4</b>	<b>Discussion</b>	<b>67</b>
4.1	Characterisation of sea ice melt stages . . . . .	67
4.2	Survey of the melt ponds . . . . .	68
4.2.1	Melt pond concentration . . . . .	68
4.2.2	Melt pond size . . . . .	70
4.2.3	Melt pond size distribution . . . . .	72
4.2.4	Melt pond density . . . . .	73
4.2.5	Melt pond density distribution . . . . .	74
4.2.6	Melt pond shape . . . . .	74
4.2.7	Melt pond shape distribution . . . . .	75
4.3	Albedo measurements . . . . .	75
4.4	Quality assessment . . . . .	77
4.4.1	Sources of error . . . . .	77
4.4.2	Geometric Distortion . . . . .	78
<b>5</b>	<b>Conclusions and Outlook</b>	<b>79</b>
	<b>List of Figures</b>	<b>I</b>
	<b>List of Tables</b>	<b>III</b>
	<b>List of Abbreviations and Symbols</b>	<b>V</b>
	<b>Glossary of Ice Terminology</b>	<b>IX</b>
	<b>Acknowledgements</b>	<b>XIII</b>
	<b>References</b>	<b>XV</b>

# Chapter 1

## Introduction

The surface albedo is an important climatological parameter of the arctic sea ice and has been investigated in numerous modeling and observational studies (Grenfell and Maykut, 1977; Morassutti and Ledrew, 1996; Perovich, 1996, 2002a, 2002b; Barber et al., 2001; Skyllingstad et al., 2009). During the melt season, the surface conditions of the arctic ice cover change enormously. The uniform high reflective surface transforms to a heterogeneous compound of several surface classes. This change is associated with a strong decrease of the surface albedo caused by the melting snow cover, the formation of melt ponds and an increasing fraction of open water (Perovich et al., 2002a). Melt ponds are pools of accumulated melt water on the arctic sea ice surface during the melt season (Taylor, 2004). Typical mean melt pond sizes vary between  $15\text{ m}^2$  and  $60\text{ m}^2$  (Perovich et al., 2002a) respectively  $12\text{ m}^2$  and  $300\text{ m}^2$  (Lüpkes et al., 2012) depending on the progress of melt pond evolution. Their size underlies a huge variability (Perovich et al., 2002a). The albedo of melt ponds is low compared to brighter bare ice and so large parts of the shortwave solar radiation get absorbed (Maykut and Grenfell, 1975). Grenfell and Maykut (1977) described the melt pond albedo and its spatial distribution as main factors in the surface radiation balance. The albedo of the sea ice surface gets affected by the snow depth and its degree of weathering, the optical properties of the ice and melt ponds, melt pond distribution and the open water fraction (Grenfell and Maykut, 1977; Grenfell and Perovich, 1984; Barry et al., 1993; Barry, 1996; Perovich et al., 2002a, 2002b; Curry et al., 2002; Skyllingstad et al., 2009).

The optical properties of the ice cover do not change considerably during

the winter months, but there is an immoderate change during the melt season (Grenfell and Maykut, 1977). Grenfell and Maykut (1977) observed a quick deterioration of the bare ice surface and a consequent development of a granular scattering layer whose surface is above the local water table caused by the increasing absorption of short-wave radiation due to the new surface classes like melt ponds and blue ice. Changes in the transparency of the ice caused by internal melting and the consequential increase in brine volume lower the albedo additionally. The stored latent heat act as a significant energy sink of the arctic heat balance. The progressive increase in brine volume follows a decrease of the extinction coefficient of the ice, especially beneath melt ponds (Grenfell and Maykut, 1977). Grenfell and Maykut (1977) described higher brine volumes beneath melt ponds than in young ice for the late summer months. The latent heat gets gradually released when the brine refreezes during freeze-up and early winter. In this period the average albedo and bulk extinction coefficient of the ice increases again (Grenfell and Maykut, 1977). If the ice of frozen melt ponds is solid enough to carry the new snow cover, the melt pond requires until November to freeze completely because of the isolating effect of the snow cover (Fetterer and Untersteiner 1998). Thick ice tends to be conserved and thin ice tends to melt preferably because of the combined effects of superficial melt water and snow cover. Only the thickest first-year ice (FYI) survives summer and becomes second-year ice. Older ice is defined as multi-year ice (MYI) (Fetterer and Untersteiner, 1998). The first drifting snow during next autumn is trapped effectively in mature ponds, so the probability that a new pond will build in the next melt season decreases strongly, because capillary action in the snow filled melt ponds elevates the water level and after that the level of frozen melt ponds (Fetterer and Untersteiner, 1998).

To capture the problem of the spatial and temporal variability of the albedo, several approaches were done (Hanesiak and Barber, 2001). Langleben (1971) described the albedo ( $\alpha$ ) as a linear function, with  $\alpha$  is equal to 0.6 for 0 and  $\alpha$  equal to 0.3 for 70% melt pond coverage. Robinson (1986) calculated a net albedo of 0.53 and Lindsay and Rothrock (1993, 1994) indicated a range from 0.76 to 0.47 from April to August for the Arctic Basin. Barber and Yackel (1999) estimated an albedo range of 0.3 to 0.5 depending on land, ice type and ice roughness. Hanesiak and Barber (2001) tested four methods to estimate the albedo in the

Canadian Archipelago. They performed direct spectral and broadband albedo surface measurements (0.54), direct broadband measurements with a helicopter (0.53), measurements with the AVHRR sensor (0.57) and an indirect measurement by using aircraft aerial survey video that was digitized and classified into albedo categories (0.55).

Grenfell and Maykut (1977) reported that the magnitude and shape of the albedo curves correlate with the amount of liquid water in the upper ice layers. Their measurement (Fig. 1.1) shows that the albedo of compact dry snow (curve a) is high with only weak wavelength dependence. The albedo of wet new snow also reveals little wavelength dependence, but it is constantly 0.05 lower (curve b). Melting snow (curve c) is independent of wavelength in the visible, but showed a spectral gradient in the near-infrared. The spectral albedo of melt ponds (Fig. 1.1, curves e-h) shows a maximum at short wavelengths and a strong decrease between 500 nm and 800 nm. Water is relative transparent for short-wave radiation and appears blueish, because values below 500 nm are mainly influenced by the scattering properties of the ice lying below. Grenfell and Maykut (1977) called the wavelengths between 500 to 800 nm the "transition zone". In this zone water becomes the predominant force and the underlying ice has no effective impact on the albedo. Therefore the visible range is crucial for the differentiations of reflection attributes of different melt ponds.

Another intervention in the radiation budget occurs from the temperature drop below the freezing point during the arctic summer. In this period the melt ponds can refreeze for a few days. Ice layers thinner than 3 cm were observed by Grenfell and Maykut (1977). The albedo of a refrozen melt pond (curve d) is lying inbetween the albedo of an open melt pond and MYI. Grenfell and Maykut (1977) measured a great range for bare ice albedo values. This range can overlap with albedo values for snow and melt ponds (Fig. 1.2).

Two types of bare ice near Point Barrow (71° N, 156° W) were described by Grenfell and Maykut (1977) during the summer months. Blue ice whose color is very similar to melt ponds, and white ice that is composed of a 5 cm to 10 cm thick drained layer. This layer was underlain by clear blue first-year ice (Grenfell and Maykut, 1977). Blue melting FYI (Fig. 1.2, curve d) has no surface

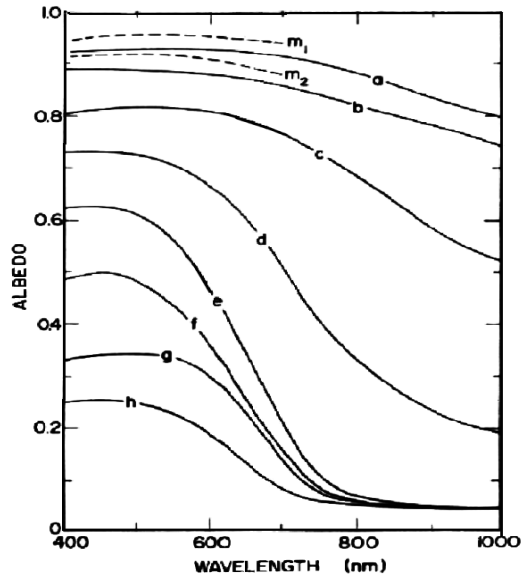


**Figure 1.1:** Spectral albedo observed over snow and melt ponds: a) dry snow ( $\rho = 400\text{kg/m}^3$ ), clear sky with haze,  $\alpha = 0.84$ ,  $\alpha_s = 0.89$ ; ( $\alpha_s =$  spectral albedo), b) wet new snow (5 cm in thickness) over multi-year white ice, overcast,  $\alpha = 0.85$ ; c) melting old snow ( $\rho = 470\text{kg/m}^3$ ), clear,  $\alpha = 0.63$ ,  $\alpha_s = 0.73$ ; (d) partially refrozen melt pond with 3 cm of ice, overcast,  $\alpha = 0.50$ ,  $\alpha_s = 0.55$ ; e) early-season melt pond (cm in depth) with white bottom on multi-year ice, overcast,  $\alpha = 0.37$ ,  $\alpha_s = 0.38$ ; f) mature melt pond (10 cm in depth) with blue bottom on multi-year ice, overcast,  $\alpha = 0.27$ ; g) melt pond (5 cm in depth) on first-year ice, overcast,  $\alpha = 0.2$ ,  $\alpha_s = 0.21$ ; and h) old melt pond (30 cm in depth) on multi-year ice, clear,  $\alpha_s = 0.15$ . Curves m<sub>1</sub> and m<sub>2</sub> were taken from Mellor (1965) and apply to dry snow and wet snow, respectively (Grenfell and Maykut, 1977).

scattering layer and therefore a low albedo. The albedo is roughly 0.1 larger at short wavelengths than that of melt pond covered FYI (Fig. 1.1, curve g), but it decreases more gently for wavelengths larger than 600 nm. The influence of its thin water film on becomes important for wavelengths larger than 1000 nm when the Fresnel limit gets achieved (Grenfell and Maykut, 1977).

For the investigation of sea ice melt stages, FYI and MYI have to be distinguished due to their different attributes. Large amounts of brine is entrapped in FYI and is concentrated at the top and bottom surfaces of the ice, resulting in a C-shaped salinity profile (Grenfell and Maykut, 1977). Melt water begins to drain through the ice during the melt season. Most of the salt from the surface layer is flushed by the draining water. Decreasing salinity takes part in the upper and lower parts of the ice. Beside the salinity, brine volume which is enclosed by the ice also depends on its temperature (Untersteiner, 1961). As a consequence,

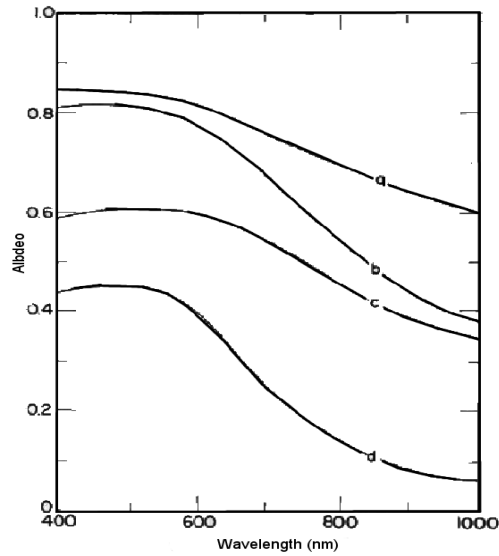


**Figure 1.2:** Spectral albedo observed over bare sea ice: a) frozen multi-year white ice, overcast,  $\alpha = 0.72$ ,  $\alpha_s = 0.74$ ; b) melting multi-year white ice, clear,  $\alpha = 0.57$ ,  $\alpha_s = 0.69$ ; c) melting first-year white ice, clear,  $\alpha = 0.47$ ,  $\alpha_s = 0.54$ ; and d) melting first-year blue ice, clear,  $\alpha = 0.24$ ,  $\alpha_s = 0.27$  (Grenfell and Maykut, 1977).

the brine volume distribution in FYI and MYI are mirrored in salinity and temperature profiles. Furthermore, the vapor-bubble density in MYI is larger than in FYI because of internal melting and freezing over certain annual cycles. FYI and MYI are different in optical properties since the differences in brine volume and bubble density (Grenfell and Maykut, 1977).

Different approaches were made to describe the different melt stages. Fetterer and Untersteiner (1998) used National Technical Means (NTM) data from 1995 to illustrate the development of melt ponds from the onset of melt pond formation to the freeze-up stage. They described the melt pond evolution as follows. The snow cover in May represented almost the entire solid precipitation of the year. Although the average wind velocity in the central Arctic was relatively small with  $4 \text{ ms}^{-1}$  to  $5 \text{ ms}^{-1}$  and storms only occurred infrequently, snow got directly, or shortly afterward snowfall events, shifted by wind (Fetterer and Untersteiner, 1998). Hence, the smooth ice area was often almost snow free with exception of some barchan snow dunes on the ice. The transported snow accumulated at aerodynamical obstacles such as pressure ridges. Typically snowfall was followed by clear and cold periods during which the temperature gradient in the snow

caused vapor diffusion, hardening of the crust and the biggest amount of snow stucked before it melted in June (Male, 1980; Fetterer and Untersteiner, 1998).

Snow thickness for level ice is about  $35 \text{ cm} \pm 17 \text{ cm}$  before melting processes begin to start (Buzueve et al., 1979; Radionove et al., 1996; Warren et al., 1998). Hanson (1980) observed a higher variability because of the collected snow on the leeward side of pressure ridges with typical depths of 1 m.

In the beginning of summer, snow became wet, but still no melt ponds were visible. The begin of melting on 31<sup>st</sup> May could be recognized by means of an increase of the emissivity of the passive microwave measurement. The increasing emissivity is owed by the increasing content of free water and therefore an increasing dielectric constant. A little peak of emissivity was found on 6<sup>th</sup> June. Temperatures above the freezing point were measured for this time period (Fetterer and Untersteiner, 1998).

Meltwater collected in sharply delineated ponds on MYI, with its rolling or hummocked surface (Zubov, 1945; Fetterer and Untersteiner, 1998). Naturally, water always flowed to the lowest elevations and drained into the ocean through cracks or collected on thin ice, whenever the surface topography was suitable for lateral motion, like at floe edges. Thin and flat areas are predestinated for the evolution of huge melt ponds. Untersteiner et al. (1998) estimated that superficial melt water can flow up to hundreds of meters. Ponds deepened and diminished in diameter fast at the beginning and more slowly at the end of their evolution, due to the fact that the melt rate of ice beneath melt ponds is 2-3 times higher than the melt rate of the bare ice surface (Hanson 1965, Untersteiner 1961; Fetterer and Untersteiner, 1998).

The midsummer period began on 13<sup>th</sup> June and first melt ponds were visible at this time. On 15<sup>th</sup> June their number increased and almost every ice floe was covered with them. The form of the melt ponds were mainly round and distinct. This changed on 20<sup>th</sup> June when ponds began to interconnect. They covered large areas between the pressure ridges. The ridges were bordered by bands of high albedo ice or snow. There was a wide range of the melt pond broadband albedo at this time and the pond coverage was between 19% and 32%. Fetterer



and Untersteiner (1998) could not exclude that the measured melt pond fraction was too high because wet snow and melt ponds were hard to distinguish. On 24<sup>th</sup> June round distinct ponds were visible again. The melt pond coverage on floes with ponds was only between 1% and 10% and some floes with a diameter smaller than 3 km were still melt pond free. On 8<sup>th</sup> and 9<sup>th</sup> July melt pond coverage was high again with values between 0 and 40%. Melt pond coverage for flat ice amounted to 40% to 50%.

Fetterer and Untersteiner (1998) had two possible explanations for that phenomena. First possible option is that the melt pond fraction was overestimated for 20<sup>th</sup> June. This theory is propped by the passive microwave measurements. The other possibility is that melt ponds refroze. This theory is propped by the fact that temperature fell below freezing point again after 20<sup>th</sup> June. The next warming event could easily melt the new thin ice layers and the melt pond concentration would increase again easily.

Until the end of June almost the whole snow coverage was gone, except of the deepest drifts. Bare ice and melt ponds covered the majority of the ice surface during that period. Snow accumulated near topographic roughness elements and favored the conservation of thick ice. The lack of an insulating snow cover on smooth, windswept young ice facilitated fast growth in winter. In summer bare ice melted earlier than snow covered ice (Fetterer and Untersteiner, 1998).

In the late summer period melt ponds began to drain and first melt pond "moats" were observed. A moat can arise when large melt ponds began to drain and leave an island of ice in the middle. So the melt pond concentration decreased again because of drainage. The interior island has often a lower albedo than the surrounding ice (Fetterer and Untersteiner, 1998).

On 15<sup>th</sup> August the freeze-up began. Some melt ponds showed a higher albedo because of the new ice layer built on the melt pond. On 27<sup>th</sup> August melt ponds were still visible, although most of them were frozen. On 5<sup>th</sup> September, some ponds were still visible. Finger rafting could be observed in leads (Fetterer and Untersteiner, 1998).

Perovich et al. (2002a) investigated the melt stages of arctic sea ice during the SHEBA (surface heat budget of the arctic ocean) campaign. SHEBA was a coordinated project to investigate the importance of the arctic influence for global change. Primary goals of the campaign were "to measure the radiative properties and microphysical structures of various cloud types in the Arctic, to measure the BRDF [bidirectional reflectance distribution function] and albedos of various surfaces (ice, snow and tundra) and various cloud types, and to obtain these measurements whenever possible either beneath the NASA ER-2 aircraft, over the SHEBA ship, or over the ARM site in Barrow for the purpose of comparing remote sensing and in situ measurements. Considerable data were collected relevant to all of these goals" (Richard, 2012). The case study of Perovich et al. (2002a) presents data from 20<sup>th</sup> May 1998 to 4<sup>th</sup> October 1998 which cover a region from 65°N to 90°N latitude and from 180°W to 120°W longitude.

In May, slightly prior to the onset of melting, the sea ice cover was fairly uniform. The two main surface classes were snow covered ice and occasionally freezing leads. Snow melt processes started at the end of May (Perovich et al., 2002a). Water collected gradually in patches on the sea ice surface. Only a few bright shallow ponds could be found on 10<sup>th</sup> June. The melt pond coverage at this time was less than 2% (Perovich et al., 2002a).

At June 22<sup>nd</sup>, melt ponds were ubiquitous (Perovich et al., 2002a). Perovich et al. (2002a) described the early ponds as wide and shallow with irregular and complex perimeters, paralleling small variations in ice surface topography. As melting continues, ponds got deeper and many of the shallow ponds drained into other ponds which were better defined. The melt ponds built distinct shapes in the early July. Later in July they widened and deepened. While spreading, they connected into large, complex network. For this melt stage a wide range of pond concentration is possible, depending on the underlying ice regime (Perovich et al., 2002a). When sea ice is not thick enough, a few ponds can melt through and drain into the ocean (Perovich et al., 2002a). Zubov (1945) observed draining ponds for sea ice that is thinner than 2 m. In the mid of August fall freeze-up began and a thin ice layer covered most of the melt ponds on 22<sup>nd</sup> August (Perovich et al., 2002a). Freezing leads with a thin snow cover are the result of continuing freezing. Winter conditions were almost recreated on 4<sup>th</sup> October. Large amounts

of young ice in leads and very little open water could be observed (Perovich et al., 2002a).

The melt pond concentration and the depending albedo change is important. However, their geometry and distribution is also relevant due to the fact that the turbulent momentum flux is affected by these parameters. Form drag is generated by floe- and melt pond edges (Lüpkes et al., 2012). Therefore the elevation of the ice surface relative to the water surface is crucial. Neutral drag coefficients can be improved by concerning the geometry of the floes and melt ponds (Lüpkes et al., 2012). Andreas et al. (2010) indicated (based on data of (Uttal et al., 2002)) that for melt pond covered sea ice surfaces the drag also gets affected by form drag. Beside the melt pond fraction, the distribution of open water can influence lateral melting (Perovich, 1983; Perovich and Maykut, 1990; Steele, 1992; Perovich et al., 2002a).

Many applications need more precise statistics for ice floes and melt ponds (Perovich et al., 2002). Lüpkes et al. (2012) made assumptions about the shape and typical size of melt ponds as a function of the sea ice concentration. They used a data set from the National Snow and Ice Data Center (NSIDC) on melt pond statistics (Fetterer et al., 2008). The data contained visible band imagery from high-resolution satellites over three arctic Ocean locations for the melt season in 1999 and four locations for the melt seasons in 2000 and 2001. Melt pond statistics were available for 400 squares with an area of 250,000  $m^2$  per square. Only squares with a lead fraction smaller than 2% were evaluated, due to the lack of statistics for leads.

Statistics of the melt pond density and the pond size distributions are also necessary to improve the understanding and the modelling of the properties of melt ponds and their evolution (Perovich et al., 2002a). Lüpkes et al. (2012) showed the effect of two different pond shapes on the number density of floes in Fig. 4.1, which shows a comparison of observed pond numbers with results of equation

$$\frac{N_p}{S_t} = \frac{A_p}{S_p} = \frac{1 - A}{S_p}, \quad (1.1)$$

with number of ponds and leads ( $N_p$ ), domain area ( $S_t$ ), concentration of ponds and leads ( $A_p$ ), area of an individual pond or lead ( $S_p$ ) and the sea ice fraction

( $A$ ) defined by Lüpkes et al. (2012) with

$$A = 1 - S_p. \quad (1.2)$$

They first assumed a quadratic and then a circular shape and used a linear dependence of the pond length. They got for a sea ice coverage between 40% and 70% a quadratic shape and for a sea ice coverage larger than 70% a circular shape. A possible explanation for this shape modification is the interconnection of melt ponds that effects a divergence from a circular shape (Lüpkes et al., 2012). Of course the shape of melt ponds and leads mostly discern from a quadratic or circular shape but they supposed that other assumptions about the mean shape would modify form drag only by a constant factor again.

Furthermore, the momentum flux  $\tau_d$  depends on the area and shape of the melt ponds. Lüpkes et al. (2012) calculated the momentum flux  $\tau_d$  for the marginal sea ice zones with:

$$\tau_d = \frac{1}{c'_s} \cdot P_d \cdot \frac{h_p}{D'_w} \cdot (1 - A), \quad (1.3)$$

where  $c'_s$  is a shape parameter for floes and melt ponds,  $P_d$  is the dynamic pressure, depending on the square of the wind velocity,  $h_p$  is the elevation of ice surface relative to the water surface in ponds or leads,  $D'_w$  is the cross wind dimension of a melt pond or floe and  $A$  is the sea ice fraction.  $D'_w$  can be calculated with:

$$D'_w = \sqrt{\frac{S_p}{c'_s}} \quad (1.4)$$

$S_p$  is the area of an individual melt pond or lead.  $c'_s$  is calculated by:

$$c'_s = \frac{U^2}{16S_p} \quad (1.5)$$

$U$  is the perimeter of the melt pond.  $c'_s$  is 1 for a quadrat and  $\frac{\pi}{4}$  for a circle.

The foregoing equations show that larger melt ponds mean a larger  $D'_w$  and therefore a smaller momentum flux. A circular pond with  $c'_s = 1$  causes a smaller momentum flux than a square-shaped melt pond with  $c'_s = \frac{\pi}{4}$ .

Different approaches were taken to investigate the different pond parameter.

Cameras that were mounted on towers (Langleben, 1969), ground measurements (Morassutti and Ledrew, 1996; Barber et al., 2001), tethered balloons (Derksen et al., 1997), helicopters (Holt and Digby, 1985; Eicken et al., 1994; Perovich and Tucker, 1997; Tucker et al., 1999; Barber et al., 2001; Perovich et al., 2002a), radar (Scharien and Yackel, 2005; Barber and Yackel, 2010), aircraft (Rothrock and Thorndike, 1984; Yackel et al., 2000; Tschudi et al., 1997, 2001), modelling (Taylor and Feltham, 2004; Skyllingstad et al., 2009) and satellites (Fetterer and Untersteiner, 1998; Barber et al., 2001; Tschudi et al., 2008; Rösel et al., 2011, 2012) have been applied.

Melt parameters that were investigated are melt pond fraction (Fetterer and Untersteiner, 1998; Barber et al., 2001; Perovich et al., 2002a; Barber and Yackel, 2010; Rösel et al., 2011, 2012); melt pond number density (Perovich et al., 2002a), melt pond perimeter (Perovich et al., 2002a), melt pond area (Tschudi et al., 2001; Perovich et al., 2002a), albedo (Grenfell, 1977; Morassutti and Ledrew, 1996; Barber et al., 2001; Skyllingstad et al., 2009), melt pond depth (Morassutti and Ledrew, 1996; Barber et al., 2001; Taylor and Feltham, 2004; Skyllingstad et al., 2009), colour (Morassutti and Ledrew, 1996), brightness (Tschudi et al., 2001) and melt pond shape (Perovich et al., 2002a).

The goal of this work is to classify images from the MELTEX 2008, NOGRAM 2011 and TIFAX 2010 flight campaigns to determine melt pond parameters such as concentration, size, size distribution, density, density distribution, shape and shape distribution. A further objective is to evaluate the broadband albedo measurements of the MELTEX campaign. Overall the work gives a quantitative description of the sea ice melt stages by means of the evaluated quantities mentioned above.



# Chapter 2

## Data and methods

### 2.1 Data description

#### 2.1.1 MELTEX 2008

The aircraft campaign MELTEX 2008 (Impact of melt ponds on energy and momentum fluxes between atmosphere and sea ice) was carried out in the Beaufort Sea (Fig. 2.1) by the Alfred-Wegener-Institute for Polar and Marine Research, the Institute for Atmospheric Physics at the University of Mainz and Environment Canada (Birnbaum et al., 2009).

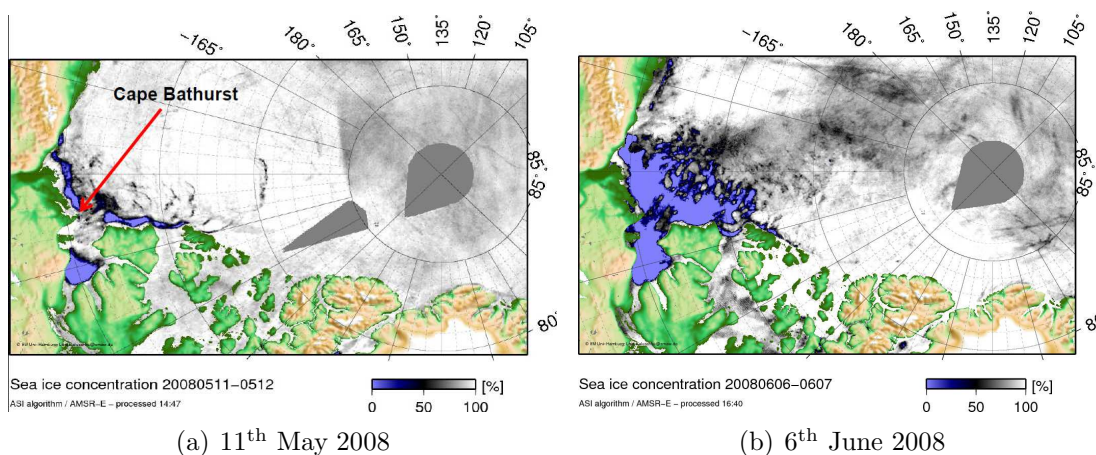


**Figure 2.1:** Sea ice extension for the area of the MELTEX campaign: a) 11<sup>th</sup> May 2008 and b) 6<sup>th</sup> June 2008. The sea ice concentration data have been derived from the AMSR-E passive microwave radiometer (Birnbaum et al., 2009).

## Goals

The primary goal of MELTEX was to enhance the quantitative understanding of the impact of melt ponds on radiation, heat, moisture, and momentum fluxes over arctic sea ice (Birnbaum et al., 2009). Objectives of the MELTEX campaign were the investigation of the melt pond fraction, broadband and spectral surface albedo for pond covered sea ice in the Beaufort Sea. Further goals were the investigation of heat and momentum transport in the atmospheric boundary layer over melting sea ice and the collection of data to upgrade algorithms for the retrieval of sea ice parameters like melt pond fraction from satellite measurements. The embracive instrumentation (Tab. 2.1) of the POLAR 5 (BASLER BT-67 type aircraft) made it possible to investigate the measurement of surface horizontal structure and radiative fluxes, the derivation of basic meteorological quantities, turbulent fluxes, surface temperature and surface topography (Birnbaum et al., 2009).

## Instrumentations

There were several instruments on board to reach the goals of the campaign (Tab. 2.1). The images were taken by the EOS 1D Mark III. This is a professional 10.1 megapixel digital single lens reflex camera produced by Canon. This photo camera had following fixed parameters:

- *focal length* =  $14 \cdot 10^{-3}m$
- *sensor pixel size* =  $0.01 \cdot 10^{-3}m$
- *sensor width* =  $18.7 \cdot 10^{-3}m$
- *sensor length* =  $28.1 \cdot 10^{-3}m$
- *number of pixels* =  $1936 (width) \cdot 1288 (height)$

## Flight tracks

Twelve flights were carried out from the 11<sup>th</sup> May to 7<sup>th</sup> June. Only the 11<sup>th</sup> May, 17<sup>th</sup> May, 26<sup>th</sup> May, 3<sup>rd</sup> June, 4<sup>th</sup> June, 6<sup>th</sup> June and 7<sup>th</sup> June were evaluated, since no further relevant information can be expected from the other flight tracks. The quality of some images is too poor because of the close fog layer under the aircraft during these flight tracks. Other evaluable flight tracks are just similar



to the evaluated ones and no further relevant informations can be expected from them.

**Table 2.1:** Aircraft instruments operated on POLAR 5 during the MELTEX campaign (Data from Birnbaum et al., 2009).

measurement	instrument
position	GPS, INS
height	radar altimeter, laser altimeter, pressure transducer
pressure	Rosemount absolute pressure transducer
air speed	Rosemount differential pressure transducer
wind vector	nose boom, GPS, INS
temperature	PT100
humidity	Lyman-alpha, dew point mirror, Vaisala humicap, CR-2
turbulence	nose boom turbulence probe (5-hole probe)
broadband short-wave radiation	Eppley pyranometer (up and down)
broadband long-wave radiation	Eppley pyrgeometer (up and down)
spectral short-wave radiation	SMART-albedometer
surface temperature	KT15 radiation thermometer, IR-line scanner
sea ice topography	two laser altimeters
sea ice concentration, melt pond concentration	UV/VIS-line scanner, digital photo and video camera
composition and dissociative flux measurements	CPFM-pod

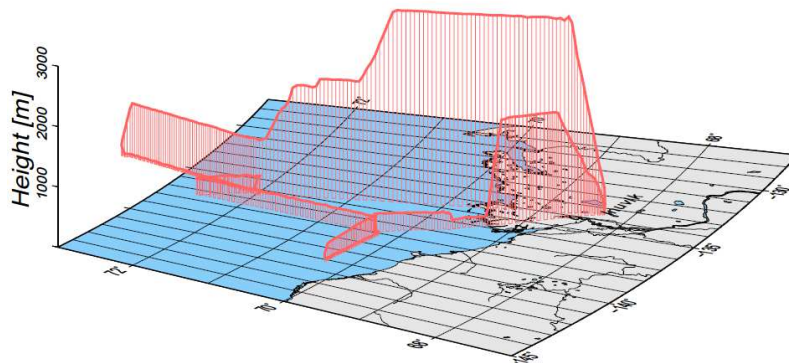


**Figure 2.2:** Example flight track at the MELTEX campaign for the 3<sup>rd</sup> June 2008. Various flight levels were reached for different parts of the flight tracks. The flight level depended mainly on the goals of the flight (Birnbaum et al., 2009).

### **Weather conditions**

Birnbaum et al. (2009) made a detailed description of the weather conditions during MELTEX. They measured an increase of the surface temperature from 11<sup>th</sup> May to 19<sup>th</sup> May 2008 from  $-10^{\circ}\text{C}$  to partially  $0^{\circ}\text{C}$ . They observed a cold-air advection from inner parts of the Arctic towards the coast of the Beaufort Sea after May 19<sup>th</sup>. A second warming event occurred from 23<sup>th</sup> May to 26<sup>th</sup> May. This warming event was responsible for the onset of melt pond formation in a large band along the coast from the Cape Bathurst Polynya (Fig. 2.1) to Alaska. The highest melt pond fraction occurred at the coast, but there were melt ponds along the whole flight track until  $71^{\circ}\text{N}$ . From 27<sup>th</sup> May to 1<sup>st</sup> June 2008, surface temperature decreased again and caused a refreezing of most melt ponds. On 2<sup>nd</sup> June 2008, Birnbaum et al. (2009) observed a thin layer of snow on the refrozen melt ponds.

At the beginning of June a third strong warming event occurred. Warm air was shifted from Alaska to the middle and western Beaufort Sea. Temperatures went above the freezing point. The strong warming event enhanced the development of melt ponds in the investigation area (Birnbaum et al. 2009). Fig. 2.3 shows the 2 m temperature profile for the time period of the investigation.

### **2.1.2 NOGRAM 2011**

The NOGRAM data set was used additionally. It offered a lot of useful images to quantify the onset of melt pond formation and the peak of melt pond evolution of MYI.

#### **Goals**

The main goal of the NOGRAM campaigns was the investigation of the offshore magnetic and gravity anomalies north of the Danish station nord. The NOGRAM 2011 complements the foregoing NOGRAM campaigns (Lehmann, 2012).

#### **Instrumentations**

Following instruments operated on board of the POLAR 5: laser and radar altimeter, 4 GPS receiver, Gravimeter, 2 CS magnetometer, tri-axial fluxgate

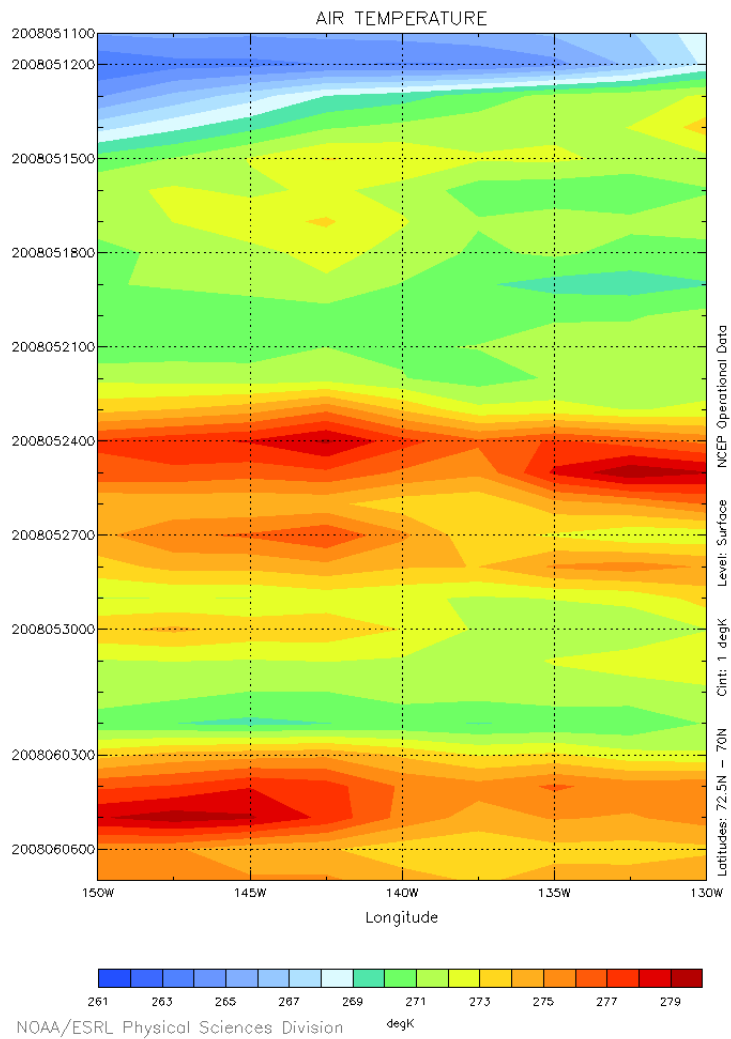


**Figure 2.3:** 2 m temperature profile for the MELTEX investigation area (11<sup>th</sup> May - 7<sup>th</sup> June 2008). Date format of the  $y$ -axis:  $yyyy-mm-dd-hh$  (NOAA-ESRL Physical Sciences Division, 2013).

magnetometer, two Canon EOS 1D Mark III for nadir and zenith photographs (Lehmann, 2012).

### Flight tracks

The NOGRAM 2011 campaign covered one major survey area, the easterly Morris Jessup Rise northly of Greenland (Fig. 2.4). Foregoing NOGRAM campaigns were carried out in the northern Fram Strait, the western MORRIS JESUP RISE and the northeastern Greenlandic ice cap of northern Kong Frederik VIII Land.

17 flights were carried out from the 14<sup>th</sup> June to the 23<sup>th</sup> June. The flight level over sea ice averaged 400 m (Lehmann, 2012). Two flight tracks were used because of their good weather conditions. The evaluated flight tracks were flown mainly over MYI. The images of July 14<sup>th</sup> could improve the characterisation of the onset of melt pond formation and those of 21<sup>st</sup> July were useful to determine the peak of melt pond evolution of MYI.

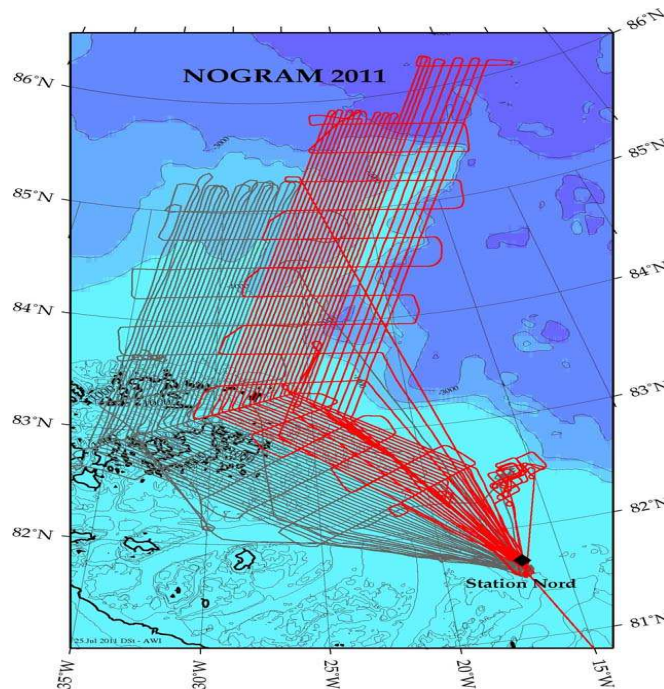


**Figure 2.4:** Investigation area of NOGRAM 1998 (grey lines) and NOGRAM 2011 (red lines) (Lehmann, 2012).

### Weather conditions

Fig. 2.5 shows the 2 m temperature profile for the area of the evaluated flight tracks ( $35^{\circ}W - 15^{\circ}W$ ,  $82.5^{\circ}N - 85^{\circ}N$ ) for the 14<sup>th</sup> to 21<sup>th</sup> July 2011. Temperatures were continuous over the freezing point. A warming event occurred between 15<sup>th</sup> and 16<sup>th</sup> July with an increase in temperature to  $6^{\circ}C$ . This warming event was probably responsible for the high melt pond concentration on 21<sup>th</sup> July.

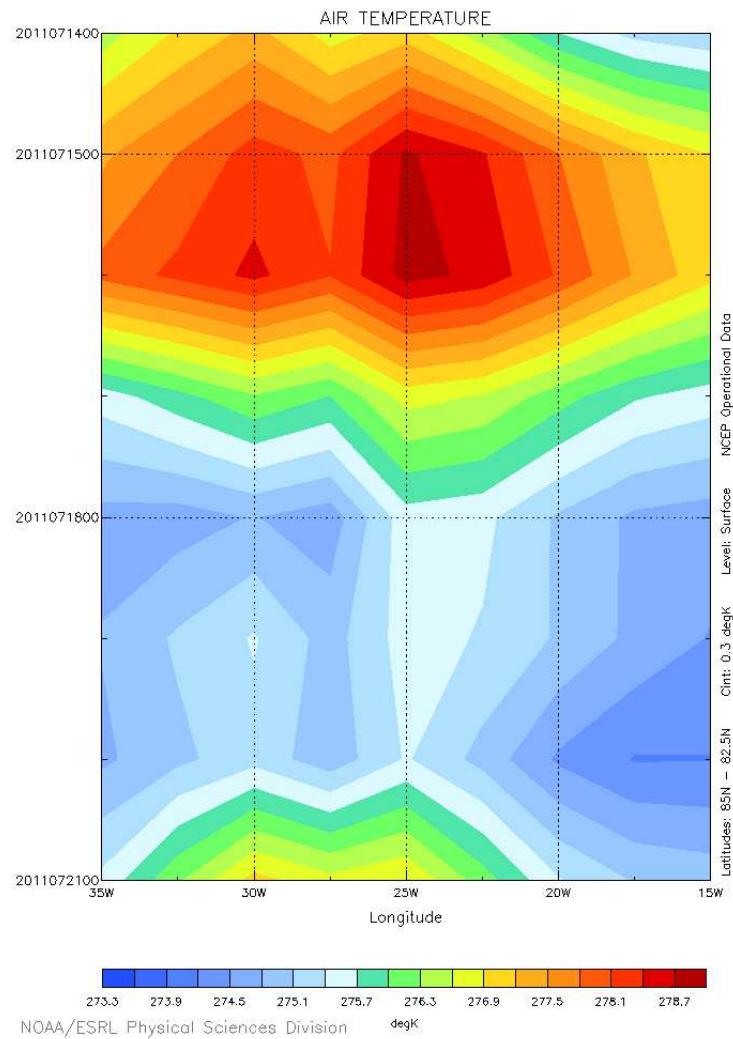


**Figure 2.5:** 2 m temperature profile for the NOGRAM investigation area (14<sup>th</sup> - 21<sup>th</sup> July). Date format of the y-axis: *yyyy-mm-dd-hh* (NOAA-ESRL Physical Sciences Division, 2013).

### 2.1.3 TIFAX 2010

#### Goals

Aim of the TIFAX 2010 (Thick Ice Feeding Arctic Export) campaign was to monitor the thickness of the sea ice which leaves the Arctic through the Fram Strait during summer months. In recognition of this importance, the thickness distribution across the Fram Strait and in the area north of Greenland was measured during the that field campaign (Krumpen and Hendricks 2010). TIFAX complements the early spring sea ice surveys.

## Instrumentations

An airborne electromagnetic system (EM BIRD) measured the ice thickness. The instrument was towed under the POLAR 5 15 meters above the ice surface. The distance to the ice-water interface can be determined by means of the contrast of electrical conductivity between sea water and sea ice. The distance to the topmost reflecting surface was measured by a second laser altimeter. Therefore ice thickness is put together as ice- and snow thickness from the difference between the laser range and the electromagnetic system derived distance (Krumpen and Hendricks 2010). Additionally, the Canon EOS 1D Mark III was on board to take pictures of the ice surface.

## Flight tracks

Four flights were carried out from the 19<sup>th</sup> August to the 22<sup>th</sup> August across the Fram Strait and in the area of north Greenland. Three flight tracks were evaluated. The evaluated flight tracks were flown mainly over MYI. The images of 19<sup>th</sup>, 20<sup>th</sup> and 21<sup>th</sup> August were useful to describe the freeze-up stage.

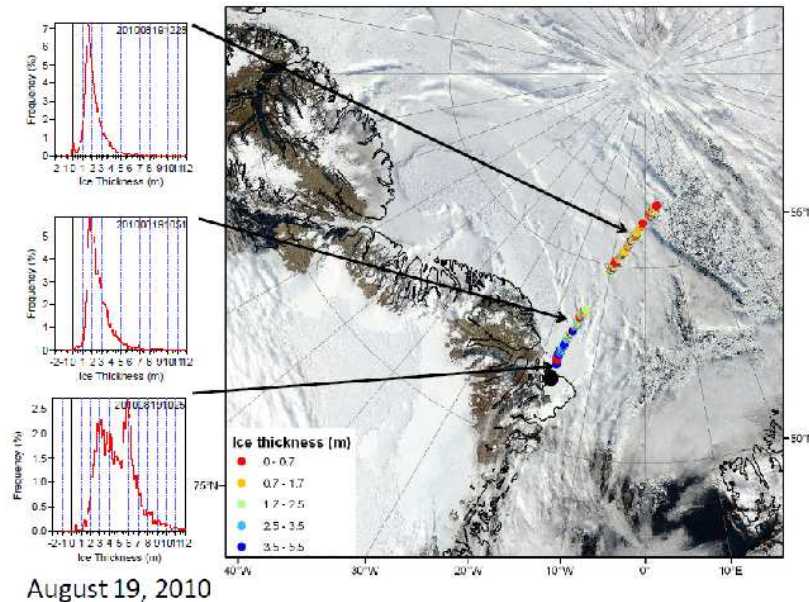


**Figure 2.6:** TIFAX-Example flight track for the 19<sup>th</sup> August. Additionally, the ice thickness distribution is shown. The maximum ice thickness reached 5.5 m near the coastline. Here this is probably MYI and the thinner ice in the north FYI (Krumpen and Hendricks 2010).

### Weather conditions

The 2 m temperature profile for the area of the evaluated flight tracks of the TIFAX campaign ( $30^{\circ}W - 0^{\circ}$ ,  $80^{\circ}N - 85^{\circ}N$ ) for the time period from 19<sup>th</sup> to 21<sup>st</sup> August 2010 is shown in Fig. 2.7. Temperature was constant below  $0^{\circ}C$  easterly of  $20^{\circ}W$  and caused the refreezing of the melt ponds. Westerly temperatures below  $0^{\circ}C$  were responsible for the melting of the frozen melt pond surfaces.

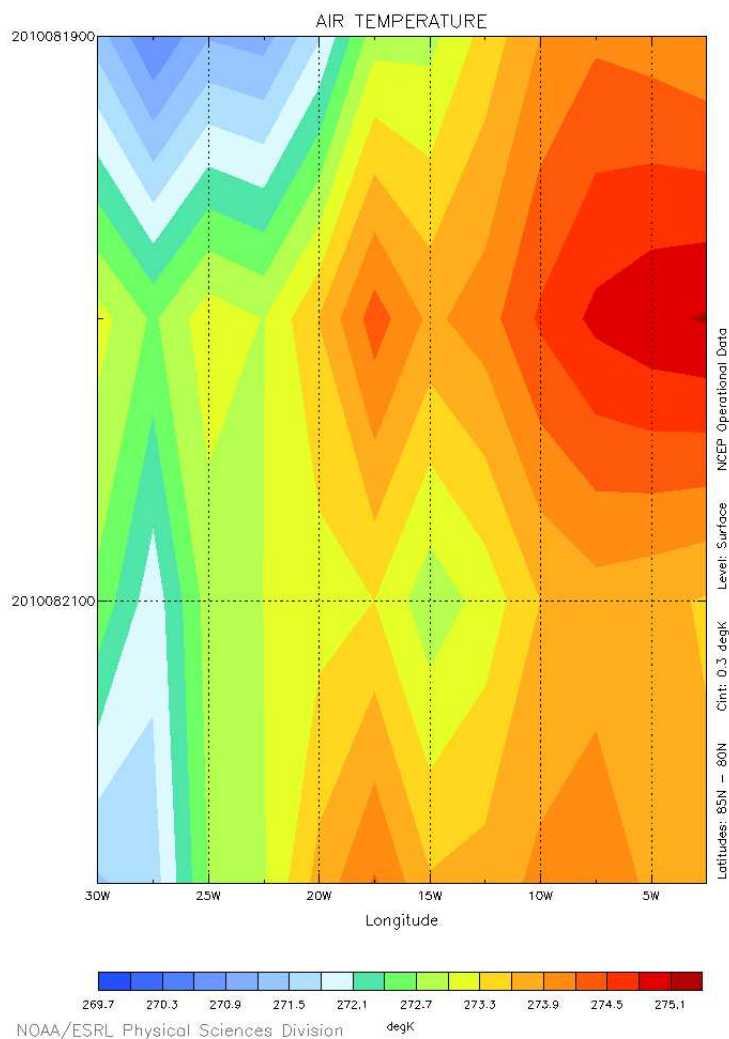


**Figure 2.7:** Temperature profile for the investigation area of TIFAX (19<sup>th</sup> to 21<sup>th</sup> August 2010). Date format of the y-axis: *yyyy-mm-dd-hh* (NOAA-ESRL Physical Sciences Division, 2013).

## 2.2 Data processing

### 2.2.1 Preselection of the aerial photographs

More than 10,000 aerial photographs were recorded during the MELTEX campaign on the different flight tracks. The quality of the images was not uniform and a lot of them were useless for an automated classification. For that reason, only high quality images were chosen. The following conditions had to be complied. Only horizontal flight tracks were used to minimise the geometric distortions. Only clear sky flight tracks were chosen to prevent a wrong classification because of fog, clouds and shadows of the clouds. The camera were operated with a non-constant exposure, so the images with a big amount of water were overexposed and useless for further evaluation. To simplify the automated classification each day was separated into different flight tracks with similar exposure, ice conditions and same flight level. Nevertheless almost 3000 images were classified and evaluated for the MELTEX campaign.

Two suitable flight tracks of the NOGRAM campaign that contain about 1000 images were chosen to complement the quantification of the melt stages. Three flight tracks with about 300 images of the TIFAX campaign were selected to describe the freeze-up stage. The automated classification was a lot easier for these two data sets. The surface of the underlying ice was much more homogeneous. Altogether 4300 images were classified and evaluated for the three flight campaigns. Depending on the flight level the images covered an area between  $0.2 \text{ km}^2$  and  $3 \text{ km}^2$ . Therefore a large area of sea ice could be investigated with the classified images.

For the characterisation of sea ice melt stages, four types of sea ice were investigated (Fig. 2.8). Thin and thick FYI as well as fast ice (FI) for the MELTEX images, FYI and MYI for NOGRAM and MYI for the TIFAX campaign. Ice thickness measurements were not available to distinguish thin and thick FYI for MELTEX. Therefore, no quantitative distinction is possible, but each ice regime has typical features which allows to distinguish qualitatively between thin and thick FYI. Most of the investigation area of the MELTEX campaign were covered by thin FYI or fast ice (FI). Only on 07<sup>th</sup> June, the most northerly part of the flight track contained a namable amount of thick FYI. This part showed a differ-



ent behaviour during the melting process and contained different surface classes than the thin FYI or FI.

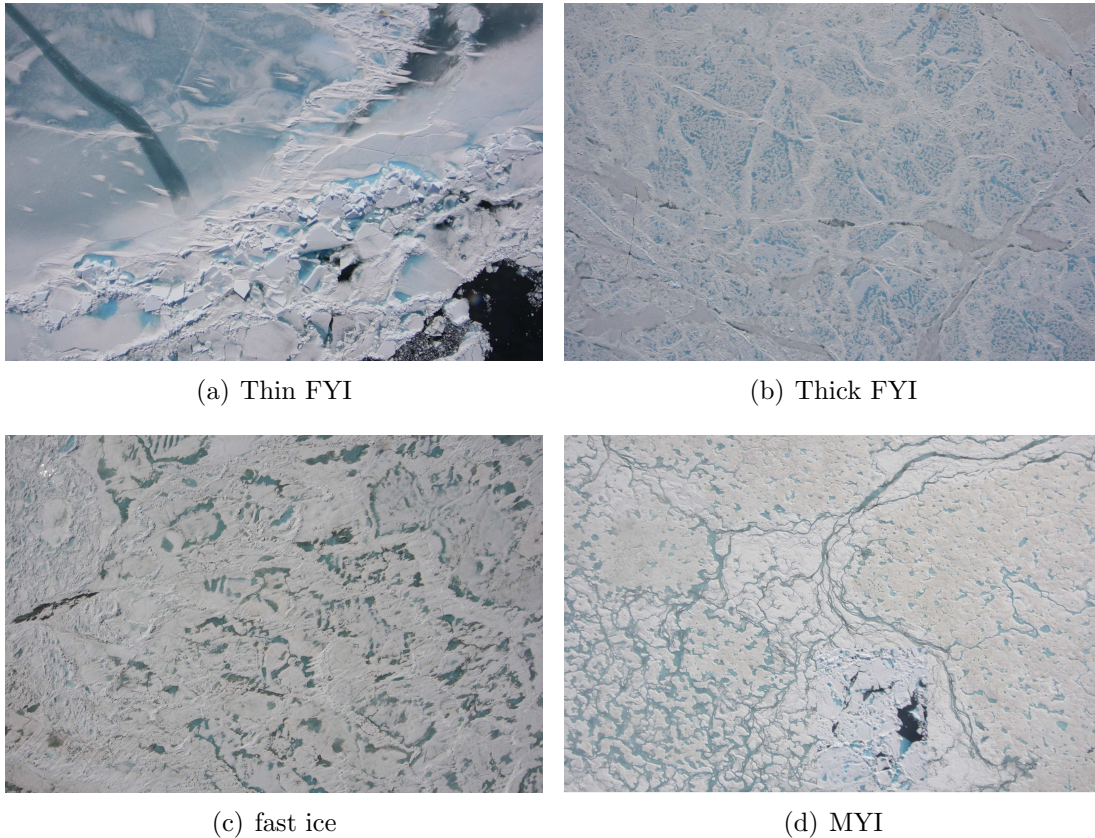


**Figure 2.8:** The four different ice regimes identified in the data. The images were taken at a) 3<sup>rd</sup> June 2008 (MELTEX), b) 7<sup>th</sup> June 2008 (MELTEX), c) 3<sup>rd</sup> June 2008 (MELTEX) and d) 21<sup>th</sup> July 2011 (NOGRAM).

### 2.2.2 Image classification

Computer-based classifications pursue the goal to determine thematic maps quantitatively. There are several assumptions for a digital classification. The reflection of determined objects differs from other objects. Same objects show the same spectral signature for similar illumination and photographic conditions. Objects that are hard to classify due to spectral similarity can be distinguished by means of artificial channels (Hildebrandt 1996).

Difference in the signature caused by varying illumination could be minimised by appropriate methods. Because of the statistical assumptions, classifications

can only deliver approximate results. By preprocessing the data prior to the classification, confounding factors like different illumination because of different relief or atmospheric influence, can be minimised. Another problem is the spectral similarity of some signatures. There are methodical and mathematical approaches for the numerical classification (Hildebrandt, 1996) which are discussed below.

### **Supervised classification**

The supervised classification is very helpful for the quantitative analysis of digital remote sensing data. The groundwork for this kind of classification is the use of algorithm to classify pixel values which belong to a certain kind of class. Lillesand and Kiefer (2004) split the supervised classification into 3 steps:

1. Definition of the region of interest (training data),
2. Classification of every pixel,
3. Generation of a thematic map and the usage of GIS.

For this kind of classification, a good knowledge about the study area is indispensable. The performer must be able to distinguish the different classes, with a preferably homogenous structure, in the picture. First, the objects have to be visually apprehended on the monitor. These objects are the so called training data or region of interests. The area of the training data should have the right size and they should be representative for the object class. At this, it is very important to estimate the variability of the object class and the consequential variance. After defining the training data, every pixel will be compared to all data classes and assigned to the right class. Thereby problems could come up for the distinction and the separability of the classes. For the accomplishment of the supervised classification different methodical approaches exist (Lillesand and Kiefer, 2004).

### **Maximum Likelihood**

Other supervised classifiers like the minimum distance or nearest neighbor are primarily based on identifying decision boundaries in feature space based on training class multispectral distance measurements. The maximum likelihood estimator is based on probability (Jensen, 2008). For every pixel  $x$ , the probability belonging

to every defined class  $c$ , is calculated. The pixels get assigned to the class with the highest probability (Jensen, 2008). Wu and Shao (2002) and McIver and Friedl (2002) described the maximum likelihood classifier as one of the most used supervised classification algorithms.

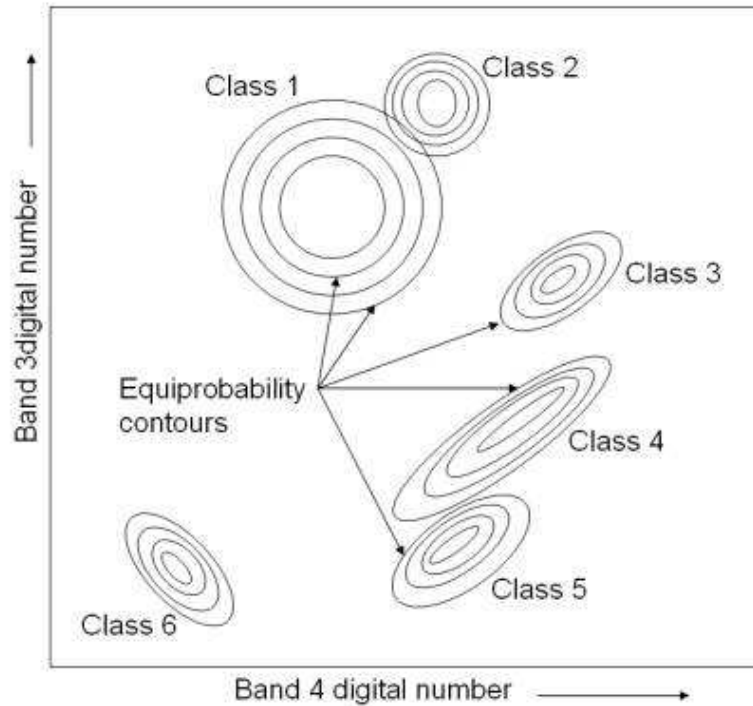


**Figure 2.9:** Equiprobability contours defined by a maximum likelihood classifier (Lillesand and Kiefer, 2004).

For this kind of classification, the training data statistics has to be normally distributed. The equation for the maximum likelihood is as follows (Erdas image field guide, 2012):

$$D = \ln(a_c) - [0.5 \ln(|Cov_c|)] - [0.5(X - M_c)^T (Cov_c^{-1})(X - M_c)] \quad (2.1)$$

with:

$D$  = quantities weighted distance (likelihood)

$c$  = a particular class

$X$  = the measurement vector of the candidate pixel

$M_c$  = the mean vector of the sample of class  $c$

$a_c$  = percent probability that any candidate pixel is a member of class  $c$  (defaults to 1.0, or is entered from a priori knowledge)

$Cov_c$  = the covariance matrix of the pixels in the sample of class  $c$

$|Cov_c|$  = determinant of  $Cov_c$

$Cov_c^{-1}$  = inverse of  $Cov_c$

$\ln$  = natural logarithm function

$T$  = transposition function

A big advantage of the maximum likelihood classifier is that it considers the variability of classes by using the covariance matrix. But if the covariance matrix contains too large values, for example when the training data has a huge scatter, then it tends to overclassify these classes (Erdas image field guide, 2012).

The maximum likelihood classification appeared to be the best classification method for the images of the three campaigns. Most flight tracks of the campaign were subdivided in several subflight tracks. For every subflight track a representative image was chosen, which contained all classes. Mostly, there were no representative images with all classes in a subflight track. Therefore, two or more images were merged for the determination of the training data. The threshold for the maximum likelihood method was set to 0.95. This means that the probability belonging to every defined class must be 0.95 or higher. Otherwise the pixels were not classified.

Fig. 2.10 shows a scatter plot of the training data for the flight track over thick FYI on 7<sup>th</sup> June 2008 (MELTEX) and the corresponding image. Plotted are the red band against the blue band. The red class represents water. Grey values are very low for both bands. Higher grey-scale values are shown by blue ice (blue) and melt ponds (cyan). The greyscale values of the blue band are little bit higher than for the red for melt ponds and blue ice. The highest greyscale values are shown by the yellow melting snow/ bare ice class.

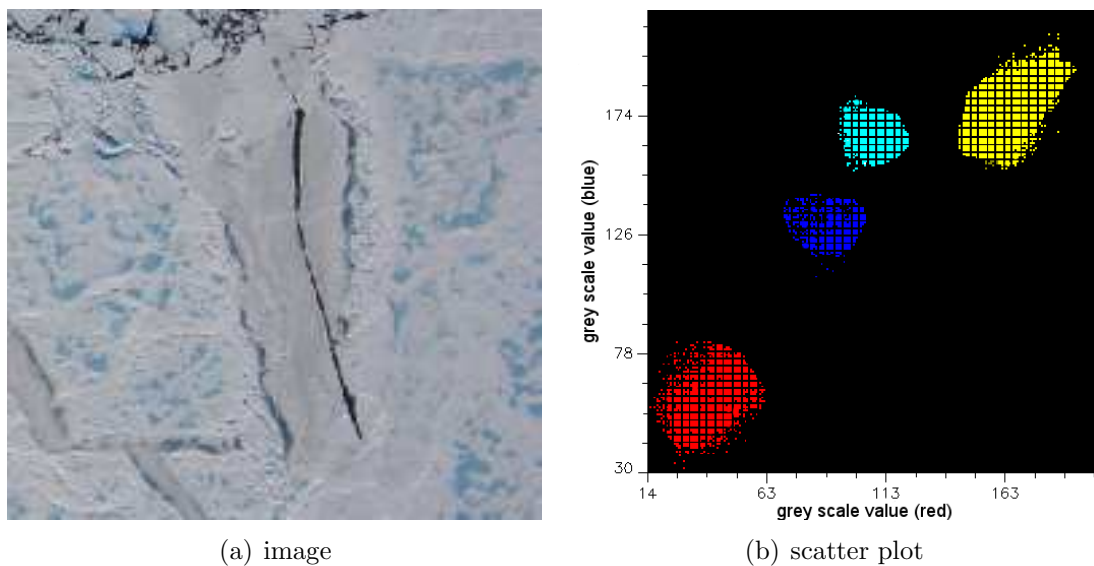


**Figure 2.10:** a) Image corresponding to b) the scatter plot of the training data for the flight track over thick FYI on 7<sup>th</sup> June 2008 (MELTEX). Plotted are the red band against the blue band: yellow = weathered snow/bare ice, cyan = melt pond, blue = blue ice, red = water.

### 2.2.3 Quality assessment

Because there is no control dataset to verify the classification results, a manual classification with high accuracy was performed. Approximately 5% of the classified images for heterogenous flight tracks were classified manually. Heterogenous flight tracks were all MELTEX flight tracks except of the dry snow images and fast ice images on 6<sup>th</sup> June. Less than 2% of the classified images were classified manually for homogenous flight tracks. All dry snow images, as well as the most images from the NOGRAM and the TIFAX campaign, were homogenous.

The manual classification was controlled manyfold. There is no way to quantify an exact error value for the control data set, but it is assumed to be very small. The rate of incorrect classified pixels is calculated by

$$E = \frac{n_c}{n_a}, \quad (2.2)$$

with  $n_c$  the number of correct classified pixels and  $n_a$ , the number of all pixels. The goal was to classify every flight track with an accuracy of at least 80%.

### 2.2.4 Survey of the melt ponds

The pixel size of each image had to be calculated for the survey of the melt ponds.

#### Calculations

The images were scaled by the following calculations. The image scale ( $I_s$ ) was calculated by

$$I_s = \frac{h}{fl}, \quad (2.3)$$

with the flight level ( $h$ ) and focal length ( $fl$ ). The image width ( $I_w$ )

$$I_w = I_s \cdot s_w, \quad (2.4)$$

with the sensor width ( $s_w$ ). The image length ( $I_l$ )

$$I_l = I_s \cdot s_l, \quad (2.5)$$

with the sensor length ( $s_l$ ). The image size ( $I_s$ ) with

$$I_s = I_w \cdot I_l. \quad (2.6)$$

The image pixel size ( $I_{ps}$ ) is calculated by

$$I_{ps} = \frac{I_l}{n_{pl}} = \frac{I_w}{n_{pw}} \quad (2.7)$$

with  $n_p$ , the number of pixels (length) and  $n_{pw}$ , the number of pixels (width). The melt pond perimeter  $U$  is calculated by

$$U = U_{un} \cdot I_{ps}, \quad (2.8)$$

with  $U_{un}$  the unscaled perimeter. The melt pond size ( $S_p$ ) with

$$S_p = S_{pun} \cdot (I_{ps})^2, \quad (2.9)$$

where  $S_{pun}$  is the unscaled melt pond area. The melt pond size and perimeter were calculated by means of arcgis 10.0 and envi 5.0. The Circularity ( $C$ ) was calculated to determine the shape of the melt ponds.

$$C = \frac{4\pi * S_p}{U^2} \quad (2.10)$$

The calculation of the melt pond shape is slightly different, from the shape calculation of Lupkes et al. (2012) (Equation 1.5) to get a value range from 0-1.

The melt pond density (PD) was computed by

$$PD = \frac{N_{mp}}{A}, \quad (2.11)$$

with  $N_{mp}$  the number of melt ponds and  $A$  the size of the investigation area.

### Geometric distortion

Airborne photographs usually contain internal (predictable) and external (unpredictable) geometric errors. Interesting for the aerial photographs taken at the three flight campaigns are external errors. Incalculable aircraft movements, initiated through atmospheric up- and downdrafts, head-, tail-, and cross-winds, can change the pitch, yaw, roll or altitude of the aircraft (Jensen 2008). Roll emerges when the aircraft fuselage is stable but the wings move up or down (rotating about the x-axis angle). The occurrence of pitch implies stable wings but the nose or the tail of the aircraft is moving in vertical direction (rotating about the y-axis angle). Yaw occurs when the wings, nose and tail are stable in height, but the fuselage is moving to the right or left side (rotating about the z-axis angle). That means that the remote sensor is displaced from the initial flight track (Lillesand and Kiefer 2004; Jensen, 2008). A constant flight level is necessary to get a uniform image scale along the whole flight track.

Large surface heights causes the topographic relief displacement (Fig. 2.11), but large differences in surface height could not be expected for sea ice surfaces. The only elevations on the sea ice surface are pressure ridges and hummocks. But they are not exuberant high and their surface fraction is very small. Therefore the topographic relief displacement is negligible for the investigated aerial photographs.

Geometric distortions introduced by the external errors mentioned above (roll, pitch, yaw or altitude change) can be corrected with ground control points (GCP) and corresponding mathematical models. A GCP is a good identifiable point on the image, which is easily to find on a map. Crossroads are a good example for a good GCP (Lillesand and Kiefer 2004; Jensen, 2008). Due to the lack of a control data set, no geometric distortions could be corrected. The only possibility was

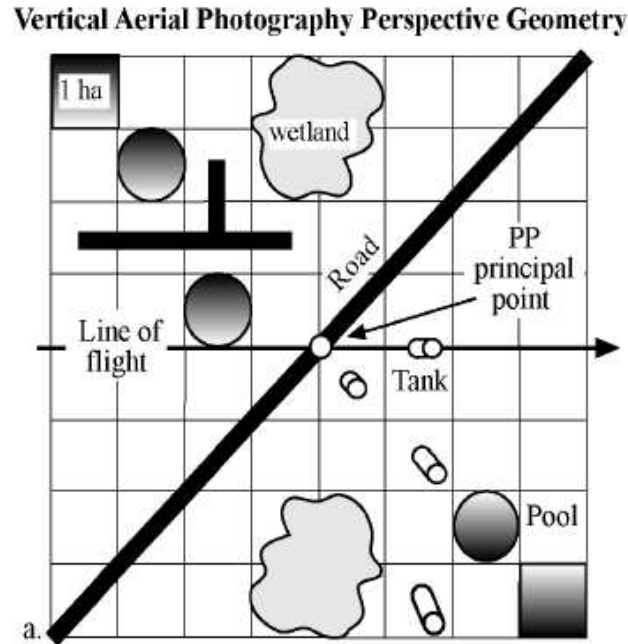


**Figure 2.11:** A vertical aerial photograph obtained over level terrain. Four equal tanks are distributed throughout the landscape and experience varying degrees of radial relief displacement the farther they are from the principal point (Jensen, 2008).

to quantify an error range.

## 2.2.5 Albedo measurements

The shortwave surface albedo ( $\alpha$ ) is generally defined as the instantaneous ratio of surface-reflected radiation flux ( $S \uparrow$ ) to incident radiation flux ( $S \downarrow$ ) of the shortwave spectral domain (Grenfell et al., 1984). The albedo is dimensionless. The broadband downward and upward short-wave radiation was measured with an Eppley pyranometer. It is calculated with:

$$\alpha = \frac{S \uparrow}{S \downarrow}. \quad (2.12)$$

The area of the measured shortwave radiation is not equal to the area of the aircraft photographs. So, errors can arise when the classification results were equalized with the albedo calculation. A typical error occurs for aircraft flights along a ice floe edge which was too far away to get caught on image, but near enough to be measured by the Eppley pyranometer. For this case, albedo values appear uncommonly low for the classified surfaces. Only the flight campaign



MELTEX included radiation shortwave measurements. No albedo data were available for NOGRAM and TIFAX flight tracks. As a further restriction, only clear sky tracks could be used for shortwave radiation measurements. After all, the investigated images must be complete free of water pixels and the previous and the following images must not contain large water areas. Dark water areas would falsify the results. As a result, only a small fraction of the investigated images were useful for further analysis.



# Chapter 3

## Results

It is not possible to illustrate an exact temporal process for the different melt stages because the flight tracks do not overlap. So every flight track investigated a different area. Nevertheless a general overview can be given.

### 3.1 Image classification

Six melt stages could be distinguished. The dry snow stage (DSS), melting snow stage (MSS), onset of melt pond formation (OMPF), melt pond evolution stage (MPES), peak of melt pond evolution (PMPE) and the freeze-up stage (FUS). The description of the peak of melt pond evolution was only possible for MYI and FI, but not for FYI. The MELTEX data set during the mid of the melt season. The six stages can be distinguished with the reflection values of the images, so this is a good segmentation because there is no need for physical measurements on the ground.

#### **Dry snow**

High sea ice surface albedo values up to 0.9 were typical for the dry snow stage. The surface temperature was almost constantly below 0°C. Hence, there was practically no melting in progress. In the photographs, four surface classes could be identified: snow covered ice, grey ice, thin black ice and open water (leads) (Fig. 3.1 and Fig. 3.2). thin black ice appeared black because of the underlying dark water body. The average dry snow cover at this time was 77.6%. 11.9% of the surface were covered by the slightly darker weathered snow, 3.3% of thin grey ice, 2.9% of black thin ice and 1.1% of water. 3.2% of the images could

not be classified (Tab. 3.1). The dry snow phase can be found for the 11<sup>th</sup> and 17<sup>th</sup> May 2008 (MELTEX), whereby almost the whole weathered snow occurred on May 17<sup>th</sup>. The ice surface cover of the 11<sup>th</sup> May almost consisted to 100% of dry high reflective snow. The images for the dry snow stage were taken over thick and thin FYI.

**Table 3.1:** Class distribution of the dry snow stage. The dry snow stage occurs on May 11<sup>th</sup> and May 17<sup>th</sup> 2008 (MELTEX).

Dry snow stage	mean	stdv	max	min
unclassified	0.032	0.010	0.040	0.001
dry snow	0.776	0.335	1	0.005
weathered snow/bare ice	0.118	0.293	0.94	0
saturated snow	0	0	0	0
melt pond	0	0	0	0
blue ice	0	0	0	0
sediment	0	0	0	0
thin grey ice	0.033	0.061	0.516	0
thin black ice	0.029	0.076	0.555	0
water	0.011	0.047	0.500	0

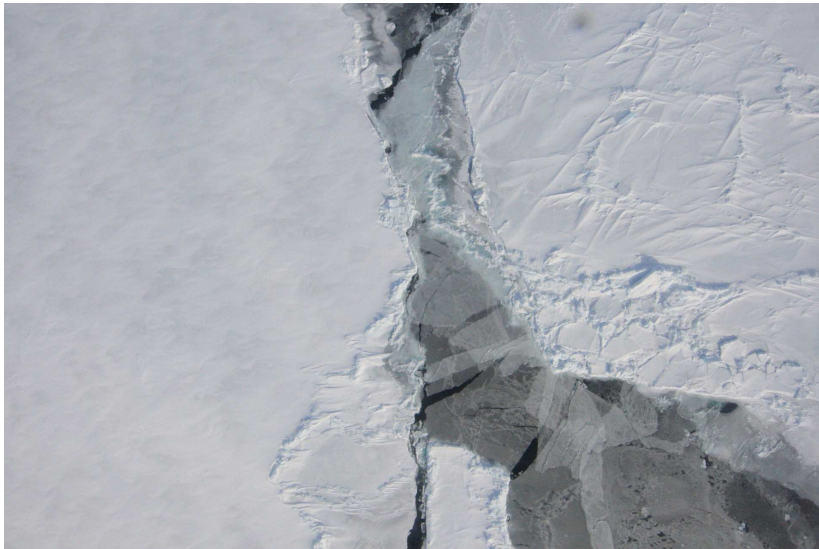


**Figure 3.1:** Example image for the dry snow stage. Example image for the dry snow stage with the four surface classes: snow covered ice, grey ice, thin black ice and open water. The image was taken at the 11<sup>th</sup> May 2008 over FYI (MELTEX).

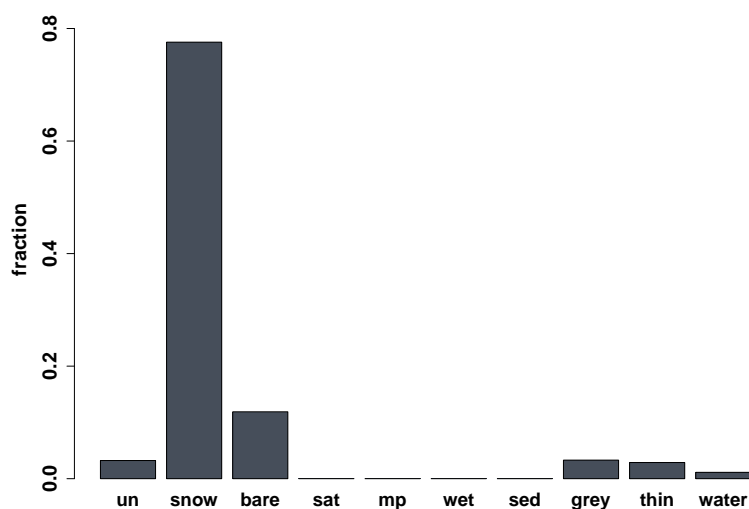


**Figure 3.2:** The surface class distribution for the dry snow stage. The dry snow class is clearly dominant. un = unclassified, snow = dry snow, bare = weathered snow or bare ice, sat = saturated snow, mp = melt pond, wet = wet blue ice, mp = melt pond, sed = sediment, grey = thin grey ice, thin = thin black ice, water = water.

### Melting snow

In the Beaufort Sea, masses of warm air warmed the snow covered ice at the beginning of summer. Snow began to melt when temperature rised above 0 °C. This implied an increase of the grain size and a decrease of the surface albedo and the resulting higher absorption of short-wave radiation. The number of surface classes although increased. Additional to the prior classes, bare ice and the blue ice (Fig. 3.3) could be observed. The bare ice and weathered melting snow class were merged to the "snow/bare" class, because there is no clear spectral difference between these classes for the RGB images. The average dry snow cover for this stage decreased strongly to 5.5% (Tab. 3.2) for dry high reflective snow, which can be found especially on pressure ridges. For this purpose there was a strong increase of the weathered snow/ bare ice class to 72.2%. The surface fraction of the wet dark blue ice class, amounted to 11.7%. This class was responsible for a strong decrease of the shortwave albedo. It appeared darker as shallow ponds, and absorbed probably as many shortwave radiation as dark melt ponds. The dark appearance resulted from the small ice thickness. In this way, it was possible that the dark underlying water body was visible at the surface. So this class only showed up for thin FYI and for FI. Relatively unchanged were the thin grey ice

(2.5%), the black thin ice (1.4%) and water classes (2.8%) (Fig. 3.4). The small changes of the last three classes were most likely because of the different flight tracks and not because of temporal change. The melting snow stage can be found for almost every MELTEX day since May 25<sup>th</sup>. The images for the melting snow stage were mainly taken over thin FYI and FI.

**Table 3.2:** Class distribution for the melting snow stage. Additionally to the foregoing classes, the wet blue ice class appeared for the first time.

Melting snow stage	mean	stdv	max	min
unclassified	0.030	0.012	0.472	0.002
dry snow	0.055	0.040	0.212	0
weathered snow/bare ice	0.722	0.130	0.906	0.322
saturated snow	0	0	0	0
melt pond	0	0	0	0
wet blue ice	0.117	0.098	0.462	0.007
sediment	0	0	0	0
thin grey ice	0.025	0.030	0.138	0
thin black ice	0.014	0.016	0.086	0
water	0.028	0.040	0.175	0

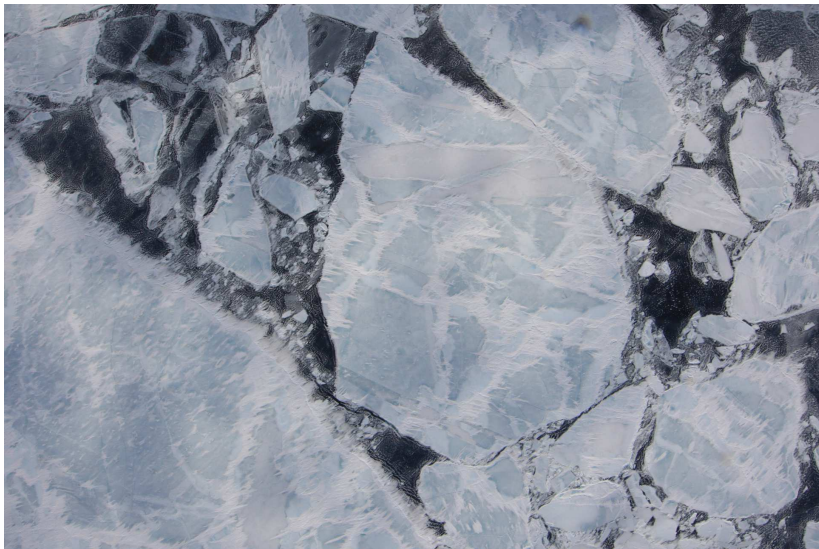


**Figure 3.3:** Example image for the melting snow stage with the new blue melting ice class. The image was taken at the 26<sup>th</sup> May 2008 over thin FYI (MELTEX).

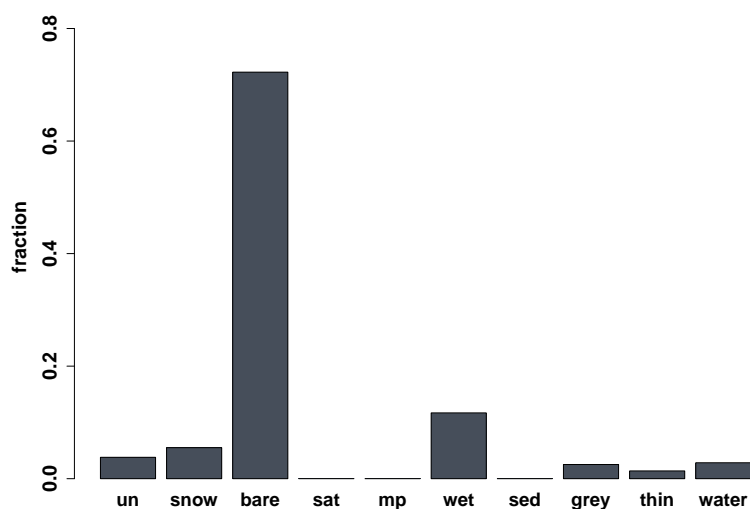


**Figure 3.4:** The surface class distribution for the melting snow stage. Blue melting ice appeared for the first time. Dry snow strongly decreased, therefore the weathered snow/bare ice class increased strongly. For further description see Fig. 3.2.

### Onset of melt pond formation

Small ponds began to build as melting processes continued with time (Fig. 3.5). The shape of the ponds was complicated and irregular. The ponds were very small and shallow and there was effectively no interconnection between different ponds. The bright melt pond class, the bright blueish appearing saturated snow class and the sediment class, came in addition to the prior classes. Melt ponds and saturated snow were not always easy to distinguish, because their spectral reflectance is merely slightly different. Sometimes sediment covered snow, ice or melt ponds and changed their shortwave reflection.

Furthermore, the dry snow concentration decreased to 3.9% (Tab. 3.3). The weathered snow bare/ ice class slightly increased to 79.4%. This increase was probably caused by the different flight tracks and because of increasing temperature. The surface fraction of the new saturated snow class amounted to 4.8%. This class was very similar to melt ponds and often hard to differentiate. The melt pond concentration at this stage was very small with an areal fraction of about  $1.6\% \pm 2\%$  with a maximum of 18%, similar to (Perovich et al., 2002a). The other classes changed slightly because of spatial reasons: blue melting bare ice with a concentration of 3.8%, sediment with 0.4%, thin grey ice with 0, thin

black ice with 1.8% and water with 1.7% (Fig. 3.6). 2.8% of the images could not be classified accurately enough.

**Table 3.3:** The surface class distribution for the onset of melt pond formation.

Onset of melt pond formation	mean	stdv	max	min
unclassified	0.028	0.011	0.048	0.001
dry snow	0.039	0.079	0.481	0
weathered snow/bare ice	0.794	0.196	0.997	0.089
saturated snow	0.048	0.091	0.59	0
melt pond	0.016	0.019	0.175	0
wet blue ice	0.038	0.068	0.488	0
sediment	0.004	0.025	0.277	0
thin grey ice	0	0	0	0
thin black ice	0.018	.0467	0.495	0
water	0.017	0.044	0.427	0

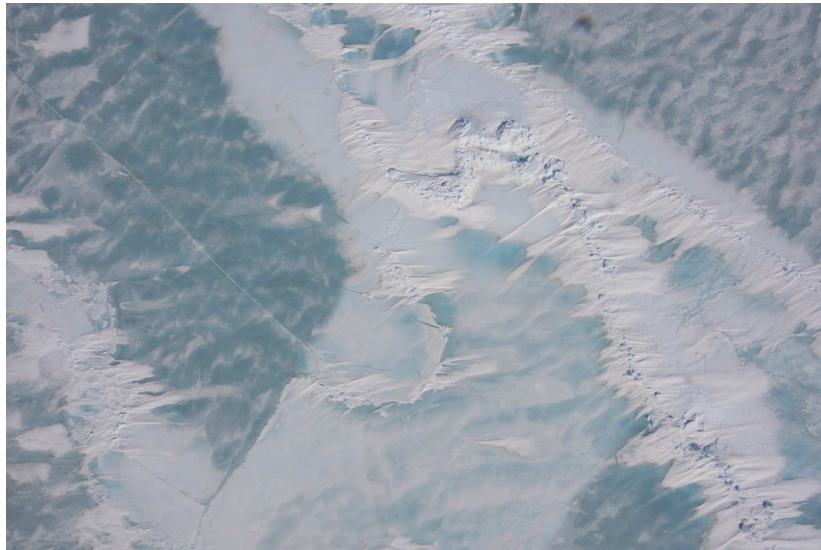


**Figure 3.5:** Example image for the onset of melt pond formation. Melt ponds mainly formed next to pressure ridges. The dark blue areas are blue melting ice. The image was taken at the 26<sup>th</sup> May 2008 over thin FYI (MELTEX).

The onset of melt pond formation can be found for 25<sup>th</sup> May, 3<sup>rd</sup> June and 4<sup>th</sup> June and also the 14<sup>th</sup> July of NOGRAM. For the NOGRAM evaluation, melt pond concentration was slightly higher ( $1.8\% \pm 0.015$ ). For the NOGRAM data set there was no melting blue ice because of the thicker ice. The images for the onset of melt pond evolution were mainly taken over thin and thick FYI, FI and MYI.



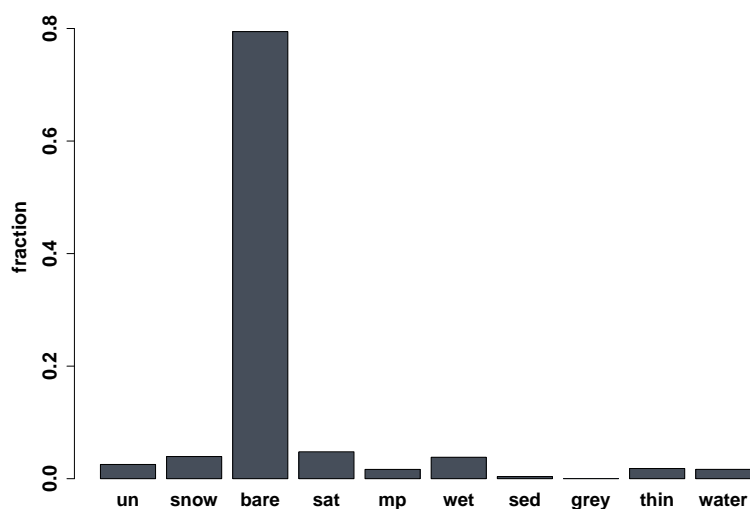


**Figure 3.6:** The surface class distribution for the onset of melt pond formation. For further description see Fig. 3.2.

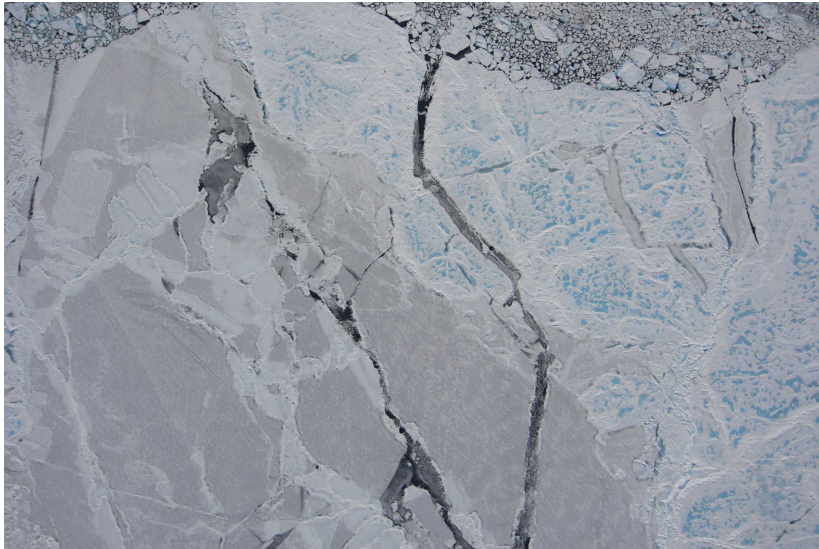
### Melt pond evolution

Later in the season on 7<sup>th</sup> June 2008, a fast increase of the melt pond size was observed for thick FYI in the Beaufort Sea (Fig. 3.7 and Fig. 3.8). Pond concentrations per ice floe were about  $10.7\% \pm 7\%$  with a maximum of 28%. First interconnections of melt ponds could be observed. The brightness of the melt ponds depends more on the thickness of the underlying ice, than on the depth of the melt ponds. Thinner ice floes were covered by darker melt ponds. A depth comparison of the melt ponds by means of the pond colour was only possible for floes with the same thickness. But there is no absolute prediction possible about the pond depth. There were no bright dry snow cover at this stage, the weathering snow bare ice class remained constant with 77.5%. The saturated snow class although dropped to 0. Melting blue ice slightly increased again to 8.7%. The surface fraction of sediment is 0, for thin grey ice 1.1%, black thin ice 0 and water 1.0%. About 1.0% of the pixels could not be classified (Tab. 3.4).

The melt pond evolution stage could be observed for the most northern part of the flight track on 07<sup>th</sup> June 2008 (MELTEX). This part was mainly flown over thick FYI. Therefore, no wet blue ice can be found for this melt stage, because the underlying water could not shine through the thicker ice. For this stage, it was much easier to circumscribe the single classes.

**Table 3.4:** Surface class distribution for the melt pond evolution.

Melt pond evolution	mean	stdv	max	min
unclassified	0.010	0.006	0.045	0.003
dry snow	0	0	0	0
weathered snow/bare ice	0.775	0.079	0.891	0.61
saturated snow	0	0	0	0
melt pond	0.107	0.068	0.285	0.034
wet blue ice	0.087	0	0	0
sediment	0	0	0	0
thin grey ice	0.011	0.023	0.113	0
thin black ice	0	0	0	0
water	0.010	0.024	0.109	0

**Figure 3.7:** Example image for the melt pond evolution with first interconnections of the melt ponds. The image was taken at the 07<sup>th</sup> June 2008 over thick FYI (MELTEX).

### Peak of melt pond evolution

Distinct ponds connected into large complex networks and they got deeper and wider. There are two possibilities for the further evolution. Melt ponds which are on thinner ice can melt through the ice and the water will drainage into the sea. If the ice is thick enough, melt ponds will grow further. It is not possible to say how thick the ice was during the MELTEX campaign, because ice thickness was not measured for these. Eicken et al (2002) described for the case that summer ice is porous enough, drainage occurs within melt ponds that are above sea level at a rate dictated by the pressure head that they create. This process is supposed

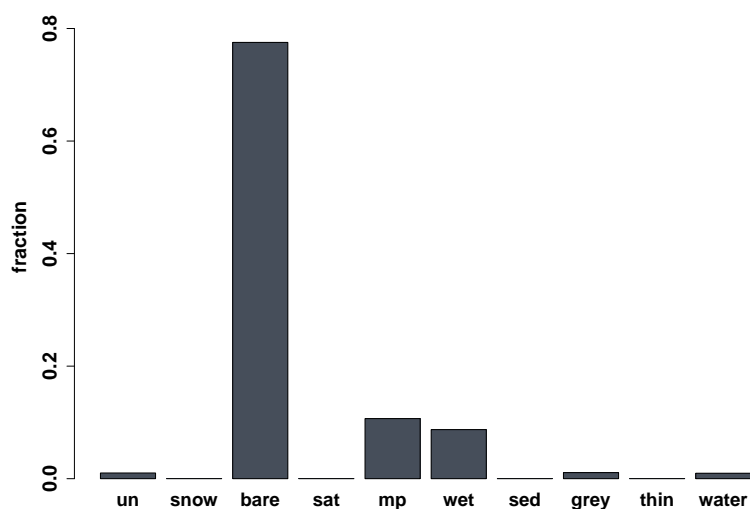


**Figure 3.8:** The surface class distribution for the melt pond evolution stage. The single classes are delimited sharper. For further description see Fig. 3.2.

to be responsible for desalination on MYI (Cox and Weeks, 1974; Untersteiner, 1968). Taylor and Feltham (2004) assumed that the effective sea level melt pond drainage has a constant rate of about 1.75 cm/day.

For this stage only bare ice, melt ponds and open water occurred. Melt ponds and bare ice were often contaminated with sediment for fast ice images. They both appeared brown and are hard to distinguish for the classification algorithm. For a higher accuracy, light and dark melt ponds were merged to one class.

**Table 3.5:** The surface class distribution for the peak of melt pond evolution of MYI.

Peak of melt pond evolution MYI	mean	stdv	max	min
unclassified	0.024	0.011	0.039	0.003
dry snow	0	0	0	0
weathered snow/bare ice	0.764	0.116	0.897	0.231
saturated snow	0	0	0	0
melt pond	0.191	0.093	0.75	0.025
wet blue ice	0	0	0	0
sediment	0	0	0	0
thin grey ice	0	0	0	0
thin black ice	0	0	0	0
water	0.021	0.004	0.048	0

Fig. 3.7 and Fig. 3.10 show example images for the PMPE of MYI and FI. Melt pond concentrations of about  $19.1\% \pm 9.3\%$  with a maximum of  $75\%$  were observed for MYI (Fig. 3.9, Tab. 3.6). Non existent were the classes dry snow, saturated snow, blue melting ice, sediment, thin grey ice, thin black ice. Water fraction was low with  $0.21\%$ . The weathered snow bare ice class was still constant with  $76.4\%$ .  $2.4\%$  of the pixels could not be classified (Fig. 3.11).

**Table 3.6:** Surface class distribution for the peak of melt pond evolution of fast ice.

Peak of melt pond evolution FI	mean	stdv	max	min
unclassified	0.024	0.016	0.411	0.003
dry snow	0	0	0	0
weathered snow/bare ice	0.536	0.164	0.954	0.057
saturated snow	0	0	0	0
melt pond	0.393	0.176	0.926	0.024
wet blue ice	0	0	0	0
sediment	0.047	0.054	0.422	0
thin grey ice	0	0.000	0.001	0
thin black ice	0	0	0	0
water	0	0	0	0

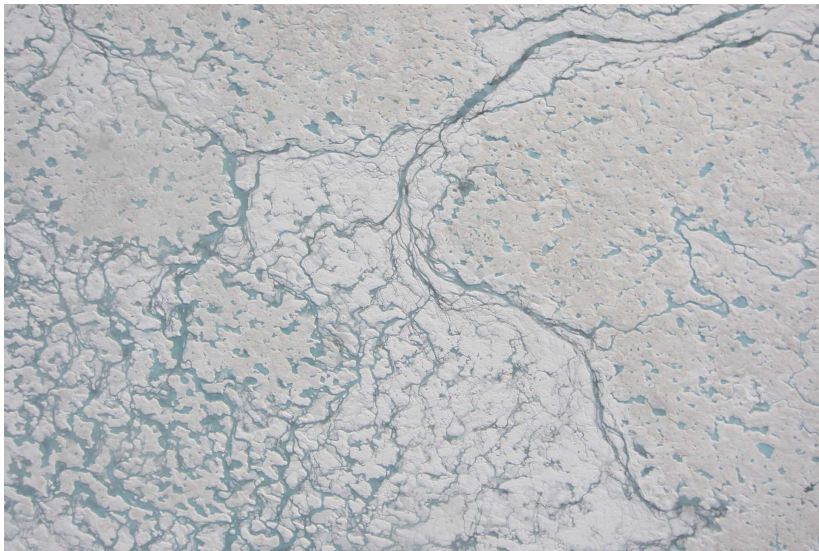


**Figure 3.9:** Example image for the peak of melt pond evolution of MYI. The image was taken at the 21<sup>st</sup> July 2010 over MYI (NOGRAM).

An average melt pond concentration of  $39.3\% \pm 17.6\%$  with a maximum of  $93\%$  were observed for fast ice (Fig. 3.10). Fig. 3.12 shows the surface class

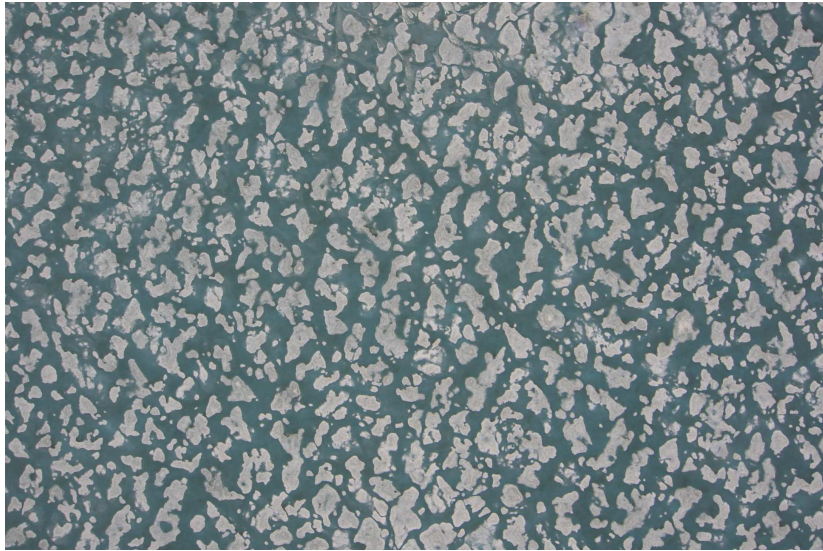


**Figure 3.10:** Example image for the peak of melt pond evolution for fast ice. The image was taken at the 06<sup>th</sup> June 2008 over FI (MELTEX).

distribution. The fraction of the classes dry snow, saturated snow, blue melting ice, thin grey ice, thin black ice and water was 0. The weathered snow bare ice class strongly decreased to 53.6% for the benefit of the increasing melt pond class with 39.3%. 4.7% of the surface were covered by sediment which can cover melt pond or ice. 2.4% of the pixels could not be classified (3.12).

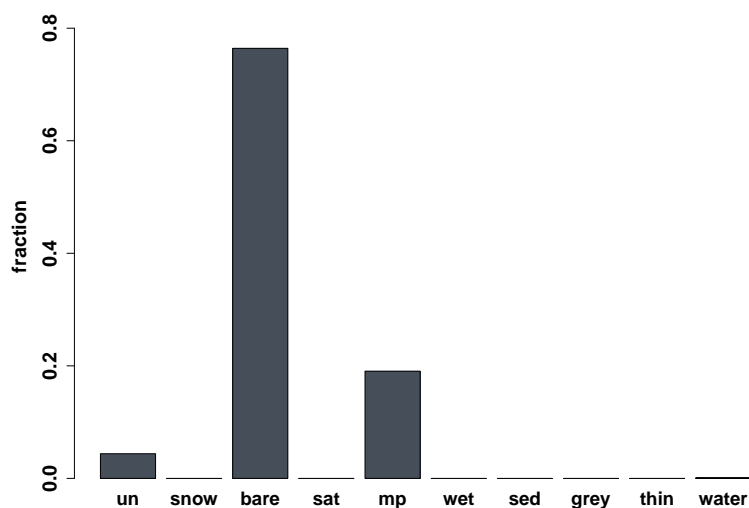


**Figure 3.11:** The surface class distribution for the peak of melt pond evolution for MYI. For further description see Fig. 3.2.

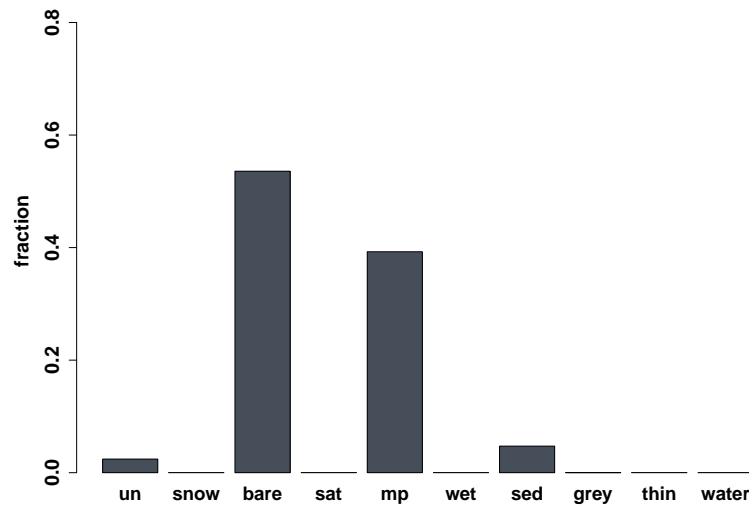


**Figure 3.12:** The surface class distribution for the peak of melt pond evolution for fast ice. For further description see Fig. 3.2.

No images were available for FYI for this melt stage. It could be expected that the melt pond concentration for FYI is higher than that for MYI. Melt pond fractions up to 0.5 were observed (Langleben and Maykut, 1977; Fetterer and Untersteiner, 1998; Naggar et al., 1998).

### freeze-up

When temperature was low again, an alternating freezing and remelting of the ponds was observed. Some frozen ponds had a light snow cover, because of snow-fall or wind drift. Most ponds were frozen. Surface classes were snow, frozen melt ponds with and without snow cover, thin black ice and water. Frozen melt ponds with snow cover are normally slightly brighter than the surrounding snow (Fig. 3.13). But there is no accurate possibility to distinguish dry snow from refrozen melt ponds with snow cover for the automated classification. The same applies to differentiation of open and refrozen ponds. The data set is only available until 21<sup>st</sup> August and no predictions about the further evolution can be made. Perovich et al. (2002a) described that at the beginning of October winter conditions dominate the sea ice surface again.

87.5% of the pixels were classified as weathered snow bare ice. The refrozen

melt pond fraction amounted to 7.7%. 0.2% of the pixels were classified as thin black ice and 2.7% as water. 1.9% of the pixels could not be classified (Fig. 3.7, Tab. 3.7).

**Table 3.7:** Surface class distribution for the freeze-up stage. Refrozen melt ponds with snow cover were classified as snow.

Freeze-up stage	mean	stdv	max	min
unclassified	0.019	0.011	0.047	0.001
dry snow	0	0	0	0
weathered snow/bare ice	0.875	0.086	0.994	0.666
saturated snow	0	0	0	0
melt pond	0.077	0.055	0.926	0
wet blue ice	0	0	0	0
sediment	0	0	0	0
thin grey ice	0	0	0	0
thin black ice	0.002	0.003	0.01	0
water	0.027	0.042	0.235	0



**Figure 3.13:** Example image for the freeze-up melt stage. The slightly brighter areas are refrozen snow covered melt ponds. The image was taken at the 20<sup>th</sup> August 2010 (TIFAX).

An interesting fact is that it is almost impossible to separate sharply between the stages. A single flight track can have several stages, even a single image can contain two stages, for the case that there are two completely different floes with different ice regimes on it.

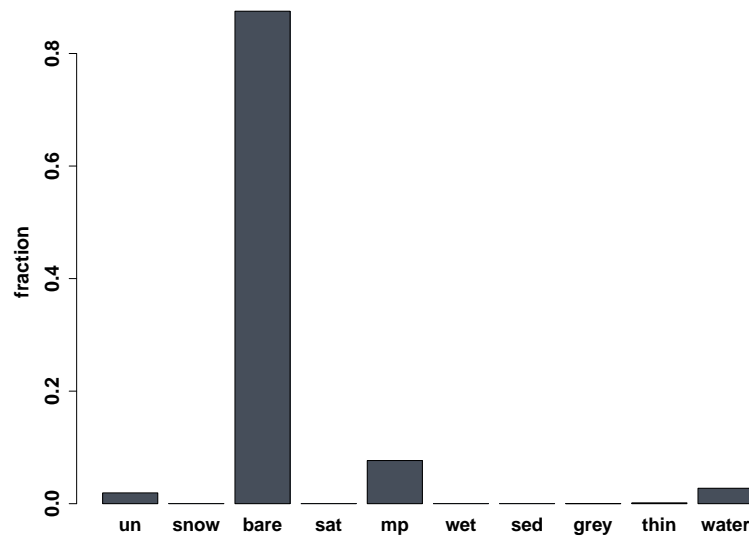


**Figure 3.14:** The surface class distribution for freeze-up stage. For further description see Fig. 3.2.

## 3.2 Survey of the melt ponds

Overall 47 images with an area of  $49.7 \text{ km}^2$  and about 105,000 melt ponds were inspected for the onset of melt pond formation, the melt pond formation, the peak of melt evolution and freeze-up stage (Tab. 3.8). The melt pond concentration, size, size distribution, density, density distribution, shape and shape distribution was evaluated. In this section, the calculated values refer only to the surveyed images. That is the reason why the melt pond concentration in Tab. 3.8 can differ from the melt pond concentration calculated for all flight tracks (Chapter 3.2.1). All images were classified manually to improve the result.

To investigate the onset of melt pond evolution stage it was necessary to use images with concentration up to 6%. On these images, it was much easier to delimit the melt ponds from the surrounding area. Hence, number of melt ponds, pond area, pond perimeter and the melt pond distribution are probably a little bit too high. The calculated circularity could be slightly too low. The flight level data was not available early enough for the TIFAX 2010 campaign. Therefore only the melt pond concentration could be calculated for the freeze-up stage.

The minimum size of the surveyed melt ponds was  $1 \text{ m}^2$  (Tab. 3.8). That



**Table 3.8:** Calculated melt pond quantities for the onset of melt pond formation, melt pond evolution, peak of melt pond evolution for MYI and peak of evolution for fast ice. Here, the melt pond concentration refers only to the surveyed images.

parameter	OMPF	MPES	MPES MYI	MPES FI
area total [ $m^2$ ]	40,403,790	8,625,830	384,874	237,389
area melt ponds [ $m^2$ ]	1,414,133	1,017,848	76,975	97,329
pond concentration	0.035	0.118	0.2	0.41
number of ponds	60,482	41,765	1795	686
<i>ponds/km<sup>2</sup></i>	1497	4842	4664	2890
area mean [ $m^2$ ]	24	24	43	142
area stdv [ $m^2$ ]	61	77	1124	1646
area min [ $m^2$ ]	1	1	1	1
area max [ $m^2$ ]	1917	4443	47,562	40,643
area median [ $m^2$ ]	7	7	4	4
area skewness	10	18	42	22
area kurtosis	172	632	1774	536
perimeter mean [ $m$ ]	19	21	43	95
perimeter stdv [ $m$ ]	22	34	896	846
perimeter min [ $m$ ]	5	4	4	4
perimeter max [ $m$ ]	575	1325	37,910	20,718
perimeter median [ $m$ ]	12	13	10	13
perimeter skewness	7	13	42	22
perimeter kurtosis	79	305	1772	516
circularity mean	0.57	0.54	0.40	0.30
circularity stdv	0.13	0.17	0.14	0.15
circularity min	0.06	0.01	0.00	0.00
circularity max	0.91	0.94	0.78	0.71
circularity median	0.57	0.56	0.41	0.31
circularity skewness	-0.4	-0.5	-0.2	0.2
circularity kurtosis	0.2	-0.2	-0.4	-0.4

corresponds to the size of four pixels of the images with lowest resolution and 16 pixels for low flight tracks with higher resolution. The melt pond density and melt pond concentration is defined in terms of ice and melt pond area, not the total area. That means that open water areas were excluded. The average difference between pond concentration per ice floe and pond concentration per total area is marginal with maximal a tenth of percent.

### 3.2.1 Melt pond concentration

In this section, the measured melt pond concentration refers to all classified images. Fig. 3.15 shows a boxplot of the melt pond concentration for the different melt stages. The bottom and top of the box are the 25<sup>th</sup> and 75<sup>th</sup> percentile, and the band near the middle of the box is the 50<sup>th</sup> percentile which is adequate to the median. The ends of the whiskers represent the lowest data point still within 1.5 interquartile range of the median of the lower quartile, and the highest data point still within 1.5 interquartile range of the median of the upper quartile. The points represent outliers.

As it was expected, the concentration of the melt ponds increased from the OMPF to the MPES stage to the PMPE for MYI and FI. (Fig. 3.15). The melt pond concentration is highly variable in time and space, even for the OMPF melt pond concentrations up to 17.5% were observed. For the MPES concentrations from 3.4% up to 28.5% are possible. An even higher variability is shown on the PMPE MYI with a range from 2.5% to 75% and for PMPE FI with a range from 2.4% to 92.6%. The PMPE FI ice exhibits a higher average melt pond concentration with 39.3% than for PMPE MYI with 19.1%.

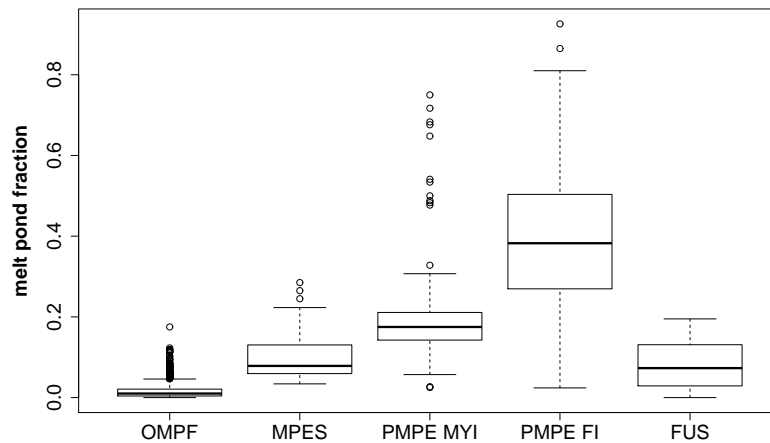


**Figure 3.15:** Boxplot of the melt pond concentration for the different melt stages. The bottom and top of the box are the 25<sup>th</sup> and 75<sup>th</sup> percentile, and the band near the middle of the box is the 50<sup>th</sup> percentile which is adequate to the median. The ends of the whiskers represent the lowest data point still within 1.5 interquartile range of the median of the lower quartile, and the highest data point still within 1.5 interquartile range of the median of the upper quartile. The points represent outliers.

### 3.2.2 Melt pond size

The size of the melt ponds for the MPES, especially for the PMPE MYI and the PMPE FI were underestimated, because some of the evaluated images were from a low flight track, and therefore, some ponds were only partially recorded. This problem also applied for higher flight tracks, although the effect gets smaller. This problem could not be solved, there are no overlapping images for low flight tracks. This impact should be negligible for the onset of melt pond evolution.

Logically melt ponds grew bigger the more progressed the evolution of melt pond was. The mean melt pond size was about  $24 \text{ m}^2 \pm 60.91 \text{ m}^2$ , for the onset stage,  $24 \text{ m}^2 \pm 77 \text{ m}^2$  for the melt pond evolution stage,  $43 \text{ m}^2 \pm 1124 \text{ m}^2$  for the peak of melt pond evolution for MYI and  $142 \text{ m}^2 \pm 1646 \text{ m}^2$  for the peak of melt pond evolution for fast ice (Fig. 3.16a and Fig. 3.16b). The biggest measured melt ponds had a size of  $47,562 \text{ m}^2$  for MYI and  $40,643 \text{ m}^2$  for fast ice. Consequently, the mean melt pond size was highly variable, especially for the peak of melt pond evolution of MYI and the peak of melt pond evolution of FI. The standard deviation exceeded 26 times the mean of the melt pond size for the peak of melt pond evolution of MYI. For the peak of melt evolution of FI it amounted to almost 12 times the mean melt pond size. Interestingly the median of the melt pond area was significantly smaller. The median for the OMPF and the MPES was  $7 \text{ m}^2$  and it got even smaller for the PMPE MYI and the PMPE FI with  $4 \text{ m}^2$  (Fig. 3.16c).

The biggest amount of melt pond growth came from the interconnections of different melt ponds. It must be assumed that the melt ponds for the onset of melt pond evolution stage were on average a little bit smaller. They should be somewhat overestimated, because the investigation area contained images with slightly higher melt pond concentration for a better distinction of the melt pond from the surrounding ice (Section 3.2).

### 3.2.3 Melt pond size distribution

The melt pond size distribution is important, to get the information, if there are many small, or a few big melt ponds. Four size classes were defined. Small melt ponds that are smaller than  $10 \text{ m}^2$ . The minimum size of the surveyed melt

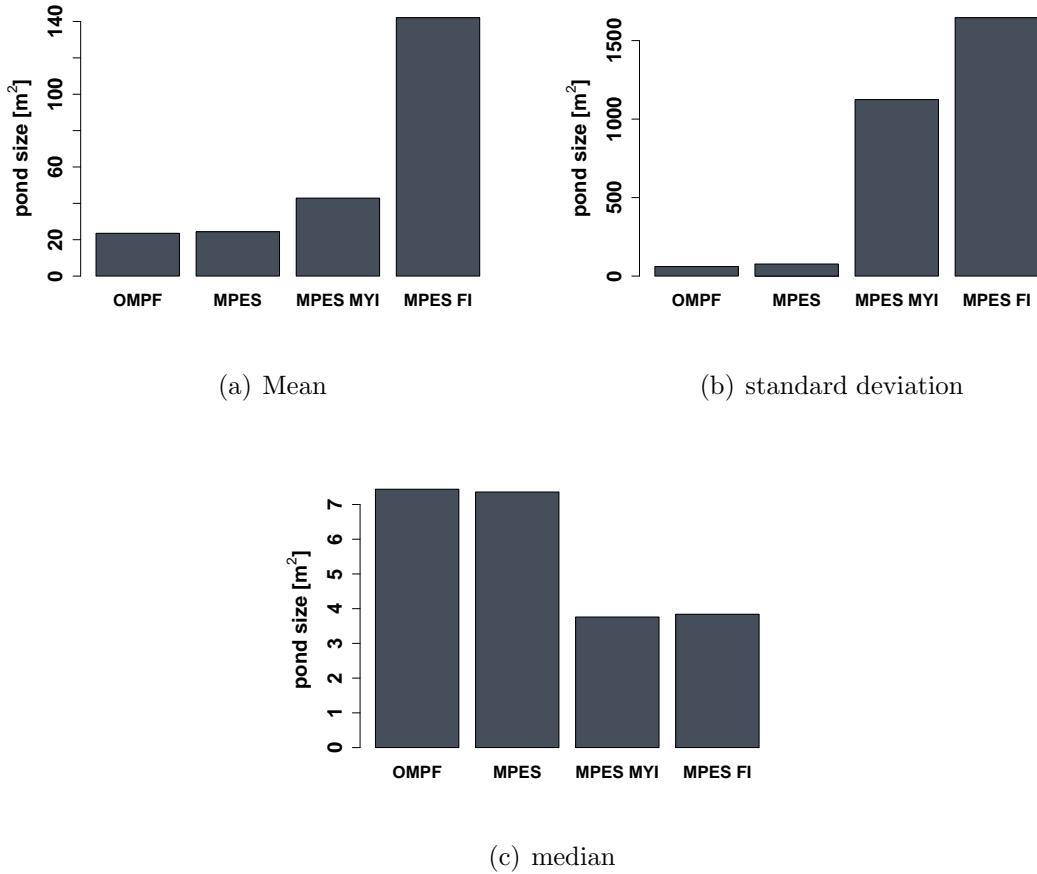


**Figure 3.16:** a) Mean melt pond size, b) standard deviation and c) median of the melt pond size for the different melt stages.

ponds was  $1 m^2$  (4 to 16 image pixels in dependency of the resolution). Medium melt ponds are equal or larger than  $10 m^2$  but smaller than  $100 m^2$ . The area of large melt ponds is equal or bigger than  $100 m^2$  and smaller than  $10,000 m^2$ . Melt ponds that are equal or bigger than  $10,000 m^2$  are defined as very large melt ponds.

57.8% of the surveyed melt ponds were small melt ponds for the onset of melt pond formation. 37.6% were medium sized and only 4.5% were bigger than  $100 m^2$ . In this early stage no very large melt ponds were present (Fig. 3.17a). The melt pond size distribution for the melt pond evolution (Fig. 3.17b) was very similar. 57.9% were small melt ponds, 37.7% were medium sized melt ponds and only 4.4% of the melt ponds were large melt ponds. The amount of very large melt ponds was 0.

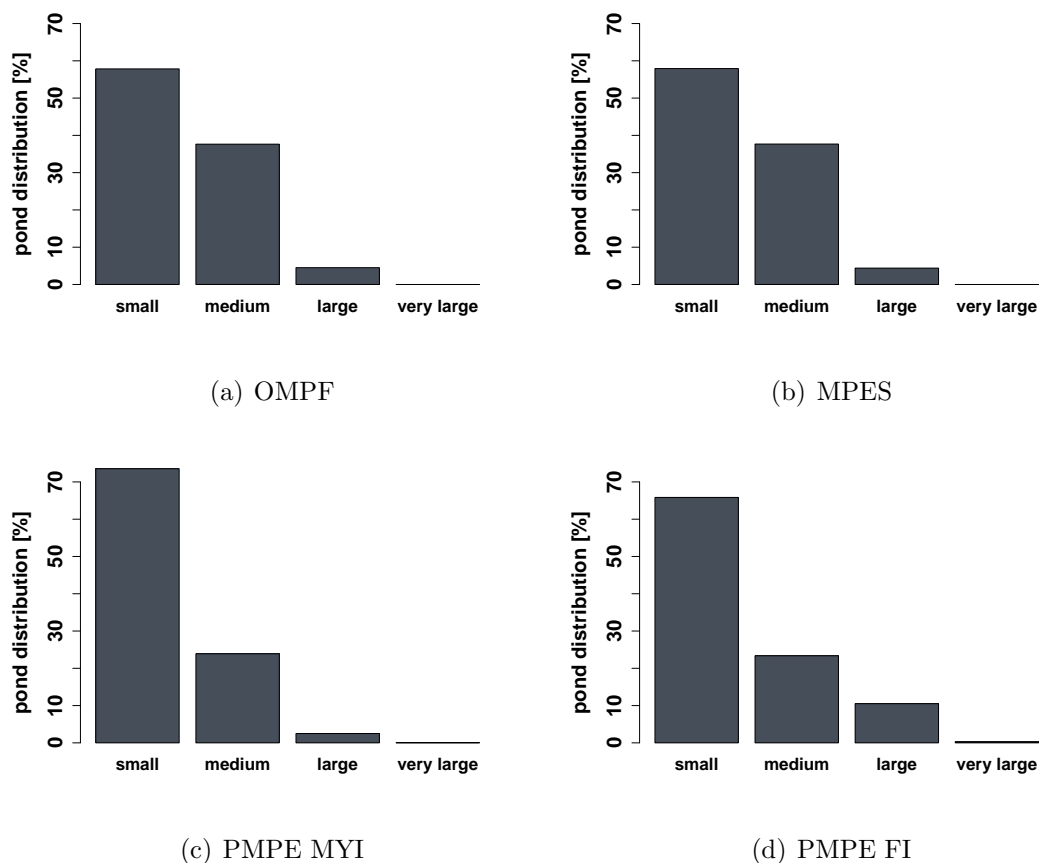
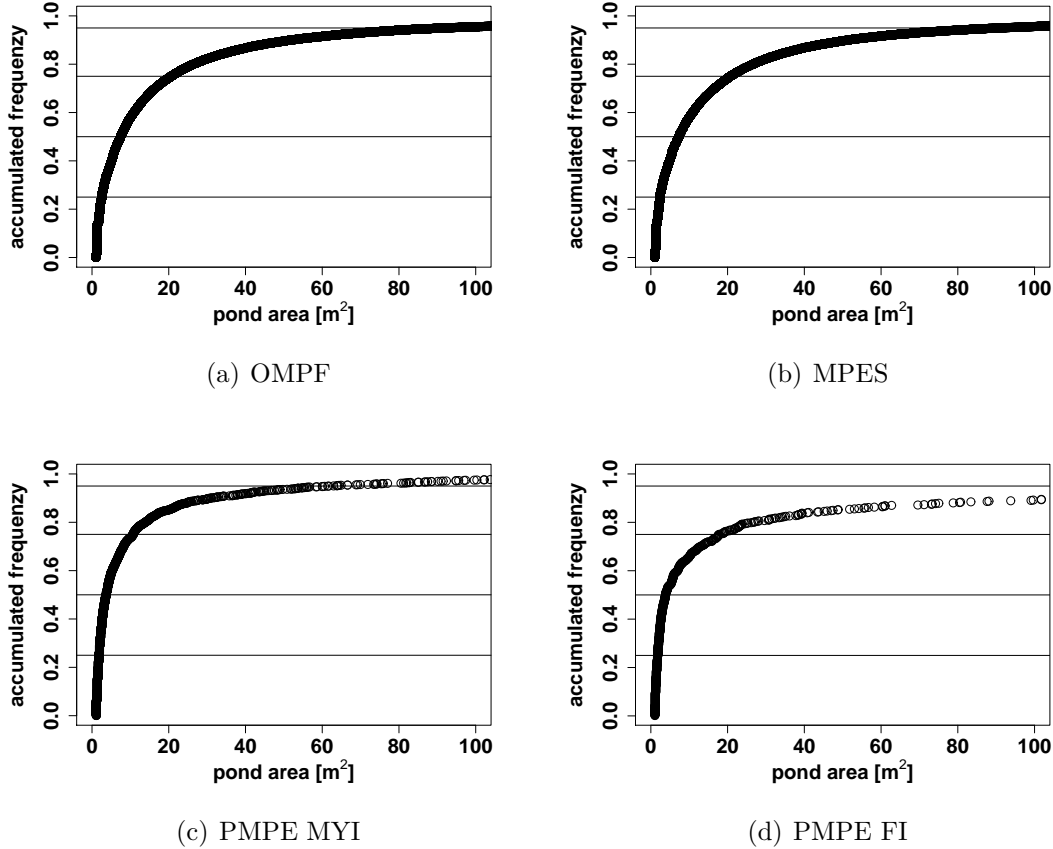


**Figure 3.17:** Melt pond size distribution for a) the onset of melt pond formation b) melt pond evolution stage c) peak of melt pond evolution (fast ice) d) peak of melt pond evolution (MYI).

For the peak of melt pond evolution of MYI the percentage of small ponds was about 16% higher than for the two earlier stages. It amounted to 73.5%. Therefore, the percentage of medium sized ponds decreased to 23.9%. The relative amount of large melt ponds also decreased a little bit to 2.5%. For the first time in the observation period, melt ponds with areas of  $10,000 \text{ m}^2$  and more appeared. Their percentage amounted to 0.1% (Fig. 3.17c).

The melt pond size distribution for the peak of melt pond evolution of fast ice was also similar. On a percentage basis, there were small melt ponds than for the onset of melt pond formation and the melt pond evolution stage, but with 65.8% about 8% less than for the peak of melt pond evolution for MYI. The percentage of medium sized melt ponds was with 23.4% very similar to the

peak of melt pond evolution of MYI. 10.5% of the melt ponds for this stage were large melt ponds that were larger than  $100 \text{ m}^2$ , but smaller than  $10,000 \text{ m}^2$ . The percentage of very large melt ponds amounted to 0.3% (Fig. 3.17d).



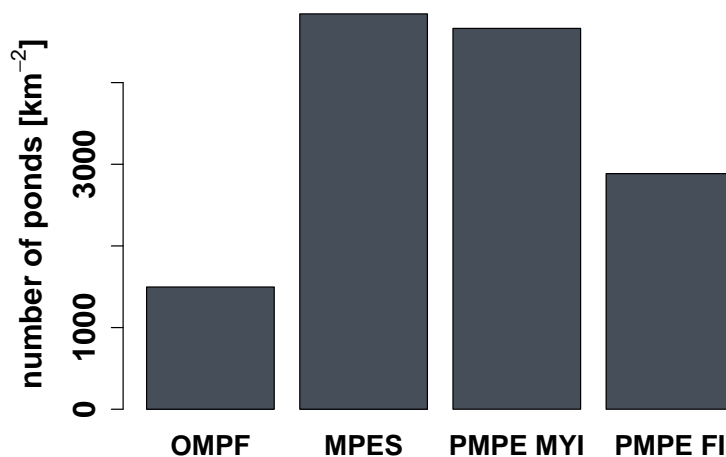
**Figure 3.18:** Melt pond size (accumulated frequency) for a) the onset of melt pond formation b) melt pond evolution stage c) peak of melt pond evolution (fast ice) d) peak of melt pond evolution (MYI). The vertical black lines are the 25%, 50%, 75% and 95% quantiles.

Fig. 3.18 showed that for the OMPF 25% of the melt ponds were smaller than  $3 \text{ m}^2$ , 50% were smaller than  $7 \text{ m}^2$ , 75% were smaller than  $21 \text{ m}^2$  and 95% of them were smaller than  $92 \text{ m}^2$ . For the MPES 25% of them were smaller than  $3 \text{ m}^2$ , 50% were smaller than  $7 \text{ m}^2$ , 75% were smaller than  $21 \text{ m}^2$  and 95% were smaller than  $91 \text{ m}^2$ . For the PMPE MYI 25% of the melt ponds were smaller than  $2 \text{ m}^2$ , 50% were smaller than  $4 \text{ m}^2$ , 75% were smaller than  $11 \text{ m}^2$  and 95% were smaller than  $62 \text{ m}^2$ . For the PMPE FI 25% of the melt ponds were smaller than  $2 \text{ m}^2$ , 50% were smaller than  $4 \text{ m}^2$ , 75% were smaller than  $18 \text{ m}^2$  and 95% were smaller than  $279 \text{ m}^2$ .

The size distribution of the melt ponds showed an extreme dominance of small melt ponds. Furthermore, this can be shown by analysing the skewness and the kurtosis of the melt pond size (Tab. 3.8). The melt pond size is positively skewed and the kurtosis is heavily leptokurtic.

### 3.2.4 Melt pond density

The melt pond density describes the number of melt ponds per area (eq. 2.11). The melt pond density amounted to  $1497 \text{ km}^{-2}$  for the onset of melt pond formation with a melt pond coverage of 3.5% . When the melting progressed the melt pond density increased to  $4842 \text{ km}^{-2}$  for the melt pond evolution stage with an average melt pond coverage of 11.8%. Higher melt pond concentrations led to decrease of melt pond density. The mean melt pond concentration amounted to 20% for the PMPE MYI, and 41% for the PMPE FI. The melt pond density amounted to  $4664 \text{ km}^{-2}$  for the PMPE MYI and only  $2886 \text{ km}^{-2}$  for the PMPE FI (Fig. 3.19).

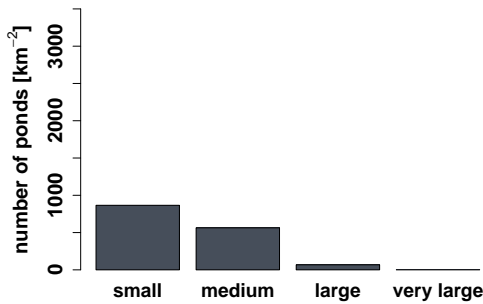


**Figure 3.19:** The melt pond density for the different melt stages. The melt pond concentration were 3.5% for OMPF, 11.8% for MPES, 20% for PMPE MYI and 41% for PMPE FI.

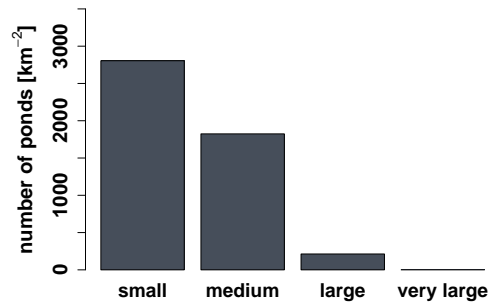
### 3.2.5 Melt pond density distribution

There were  $866 \text{ km}^{-2}$  small melt ponds for the onset of melt pond formation stage. The number of medium sized melt ponds was slightly less with  $563 \text{ km}^{-2}$ . Only 68 melt ponds per  $\text{km}^2$  were bigger than  $100 \text{ m}^2$ . No melt pond reached a size larger than  $10,000 \text{ m}^2$  at this early stage (Fig. 3.20a).

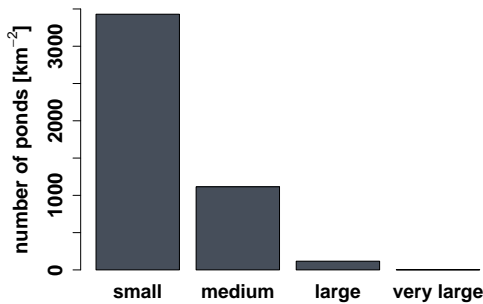
The number of small melt ponds per  $\text{km}^2$  increased strongly to 2805 for the melt pond evolution stage. The number of medium sized melt ponds per  $\text{km}^2$  also increased rapidly to 1824, as well as the melt pond density of large melt ponds increased to  $213 \text{ km}^{-2}$ . Even at this melt stage, no very large melt ponds were observed (Fig. 3.20b).



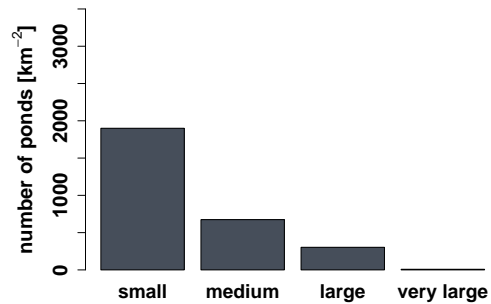
(a) OMPF



(b) MPES



(c) PMPE MYI



(d) PMPE FI

**Figure 3.20:** The melt pond density distribution for the different melt stages.

The melt pond density for the peak of melt pond evolution of MYI was even



higher with 3430 small melt ponds per  $km^2$ . However, the melt pond density for medium sized and for large melt ponds was lower with  $1115 km^{-2}$  and  $117 km^{-2}$ . Almost 3 melt ponds per  $km^2$  could be identified as very large melt ponds (Fig. 3.20c).

For the peak of melt pond evolution of fast ice the number of small melt ponds  $km^{-2}$  only amounted to 2000. Although the melt pond density of medium sized melt ponds was smaller with  $674 km^{-2}$ . Therefore, there were 303 melt ponds  $km^{-2}$  whose size were larger than  $100 m^2$  and smaller than  $10,000 m^2$ . Over eight melt ponds  $km^{-2}$  were observed whose size were bigger than  $10,000 km^2$  (Fig. 3.20d).

### 3.2.6 Melt pond shape

The circularity ( $C$ ) was calculated using eq. 2.10. The circularity for

- a circle:  $C = 1$ ,
- a square:  $C = \pi/4 \approx 0.785$ ,
- a rectangle with an aspect ratio of 1:2:  $C = 2\pi/9 \approx 0.698$ ,
- a rectangle with an aspect ratio of 1:4:  $C = 4\pi/25 \approx 0.503$ ,
- a rectangle with an aspect ratio of 1:8:  $C = 8\pi/81 \approx 0.310$ ,
- a rectangle with an aspect ratio of 1:16:  $C = 16\pi/281 \approx 0.174$ ,
- a line:  $C = 0$ .

The smaller the values for  $C$  get, the more the melt pond shape approaches to a line. The average circularity (Fig. 3.21) dropped from 0.57 (OMPF) to 0.54 (MPES) to 0.40 (PMPE MYI) to 0.30 (PMPE FI).

Fig. 3.22 shows the circularity of the melt ponds as function of their perimeter. The highest circularity values were reached for the onset of melt pond formation with an average circularity of  $0.57 \pm 0.13$  (Fig. 3.21, Tab. 3.8). With further melt pond evolution the average circularity decreased to  $0.54 \pm 0.17$ . For the peak of melt pond evolution, circularity decreased to  $0.4 \pm 0.14$ , for MYI, and to

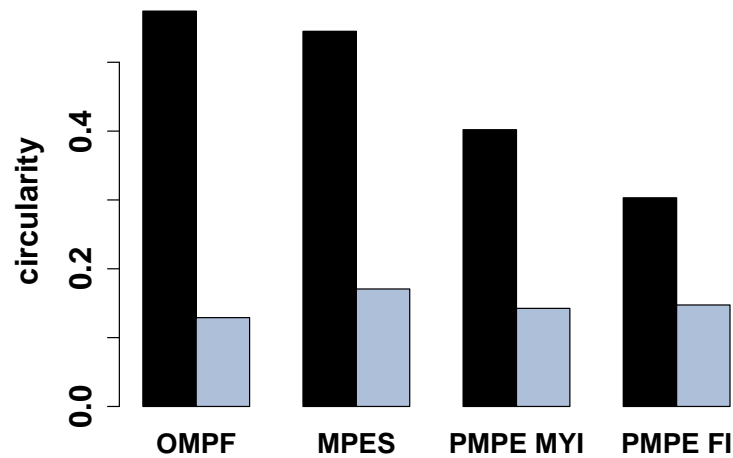


**Figure 3.21:** Average circularity (black) and the standard deviation (grey) depending on the melt stage

$0.3 \pm 0.15$ , for FI. For the peak of melt pond evolution the maximum circularity only amounted to 0.78 for MYI and 0.71 for fast ice, while the maximum circularity for the foregoing stages reaches values over 0.9.

For smaller melt ponds, all kind of circularity were existent and for melt ponds which were bigger than a certain threshold, there were only small circularity values (Fig. 3.22). This was because of the interconnection of certain melt ponds to linear shaped ponds. The data set was smoothed by means of the Nadaraya-Watson kernel regression (Fig. 3.22, blue lines). The used Bandwith was 10 and a gaussian kernel was used. For further information about the Nadaraya-Watson kernel regression see Nadaraya (1964). For the kernel smoothed data, melt pond perimeters which were larger than 183 m, became below the threshold for a rectangle with an aspect ratio from 1:16 for the OMPF. In this case, the pond shape approached the shape of a line. For the melt pond evolution stage, a 124 m perimeter was sufficient to become below that threshold. For the peak of melt pond evolution of MYI, ponds with a perimeter larger than 89 m undercut the threshold, and for fast ice, ponds with perimeters larger than 65 m were reaching the threshold. The maximum circularity for the smoothed data got reached for pond perimeters larger than 10 m (OMPF, MPES). The explanation is probably that small melt ponds with a low resolution of 4 pixels can not get a higher

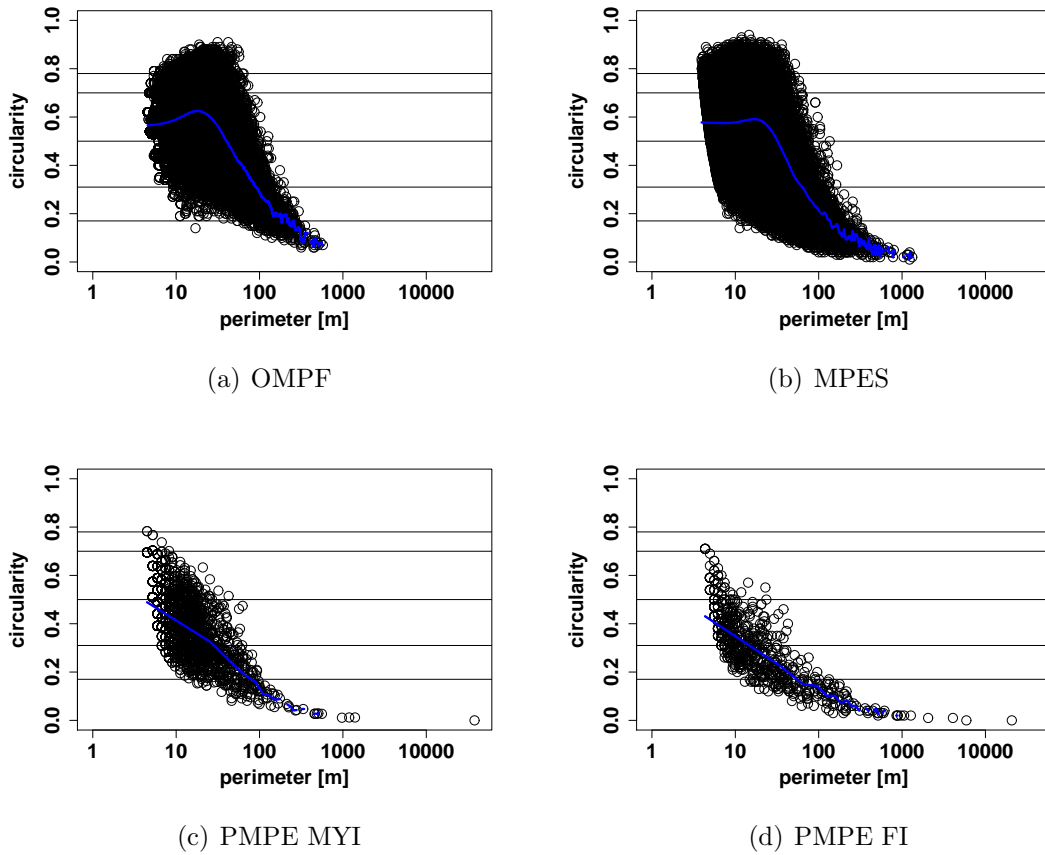


**Figure 3.22:** Circularity of the melt ponds depending on their perimeter for the different melt stages. The x-axis is log scaled. The blue lines are smoothed by Nadaraya-Watson kernel regression (bandwidth = 10, kernel = gaussian). The black lines illustrates the different shapes of C mentioned above.

circularity than a square (Pixel = square). This problem get reduced for larger ponds. This problem do not occur for the peak of melt pond evolution of MYI and FI. Small melt ponds had the highest smoothed circularity for this stages.

### 3.2.7 Melt pond shape distribution

The percentage circularity distribution is shown in Fig. 3.24 and in Tab. 3.9. Six shape classes were defined. The first class concludes all melt ponds whose circularity is higher than or equal to 0.785. So, that class includes all shapes that lie between a circle and a square. All melt ponds whose circularity is smaller than 0.785 or higher than 0.698 are sorted into the second class. This class contains all shapes that lie between a rectangle with an aspect ratio of 1:2 and a square. The

third shape class contains all kind of shapes lying between a rectangle with an aspect ratio of 1:2 and a rectangle with an aspect ratio of 1:4. The fourth shape class contains all kind of shapes lying between a rectangle with an aspect ratio of 1:4 and a rectangle with an aspect ratio of 1:8. The fifth shape class contains all kind of shapes lying between a rectangle with an aspect ratio of 1:8 and a rectangle with an aspect ratio of 1:16. The last shape class contains all kind of shapes lying between a rectangle with an aspect ratio of 1:16 and a line. So, the circularity gets smaller from class 1 to class 6.

For the OMPF class 1 contained 3.2% of the melt ponds, class 2 17.6%, class 3 55.3%, class 4 20.4%, class 5 3.0% and class 6 0.5% of the melt ponds. So most melt ponds corresponded to class 3 which contained all kind of shapes lying between a rectangle with an aspect ratio of 1:2 and a rectangle with an aspect ratio of 1:4. For the melt pond evolution stage class 1 contained 5.0%, class 2 contained 16.7%, class 3 contained 43.9%, class 4 contained 23.4%, class 5 contained 7.5% and class 6 contained 3.6% of the melt ponds. For the peak of melt pond evolution of MYI class 1 contained 0, class 2 contained 2.1%, class 3 contained 26.0%, class 4 contained 43.6%, class 5 contained 21.9% and class 6 6.4%. For the peak of melt pond evolution of fast ice class 1 contained 0, class 2 0.7%, class 3 6.9%, class 4 39.3%, class 5 29.3% and class 6 23.8%. For OMPF and MPES most melt ponds corresponded to class 3. Most melt ponds corresponded to class 4 for the PMPE MYI and the PMPE FI. The number of melt ponds in class 5 and class 6 also increased heavily. Fig. 3.23 and Tab. 3.10 show the shape distribution in absolute numbers.

For the onset of melt pond formation class 1 contained 1913 melt ponds, class 2 contained 10,642 melt ponds, class 3 contained 33,476, class 4 contained 12,322, class 5 contained 1820 and class 6 contained 309 melt ponds. For the melt pond evolution stage class 1 contained 2077 melt ponds, class 2 contained 6971, class 3 contained 18,320, class 4 contained 9775, class 5 contained 3139 and class 6 contained 1483 melt ponds. For the peak of melt pond evolution of MYI class 1 contained 0, class 2 contained 38, class 3 contained 466, class 4 contained 782, class 5 contained 394 and class 6 contained 115 melt ponds. For the peak of melt pond evolution of fast ice class 1 contained 0, class 2 contained 5, class 3 contained 47, class 4 contained 269, class 5 contained 201 and class 6 contained

163 melt ponds.

**Table 3.9:** Circularity distribution in absolute numbers. For further description see Tab. 3.9

Melt stage	class 1	class 2	class 3	class 4	class 5	class 6
OMPF	1913	10,642	33,476	12,322	1820	309
MPES	2077	6971	18,320	9775	3139	1483
PMPE MYI	0	38	466	782	394	115
PMPE FI	0	5	47	269	201	163

**Table 3.10:** Circularity percentage distribution. class 1 = first shape class ( $C > 0.785$ ), class 2 = second shape class ( $0.698 < C < 0.785$ ), class 3 = third shape class ( $0.503 < C < 0.698$ ), class 4 = fourth shape class ( $0.310 < C < 0.503$ ), class 5 = fifth shape class ( $0.174 < C < 0.310$ ) and class 6 = sixth shape class ( $C < 0.174$ ).

Melt stage	class 1 [%]	class 2 [%]	class 3 [%]	class 4 [%]	class 5 [%]	class 6 [%]
OMPF	3.2	17.6	55.3	20.4	3.0	0.5
MPES	5.0	16.7	43.9	23.4	7.5	3.6
PMPE MYI	0	2.1	26.0	43.6	21.9	6.4
PMPE FI	0	0.7	6.9	39.3	29.3	23.8

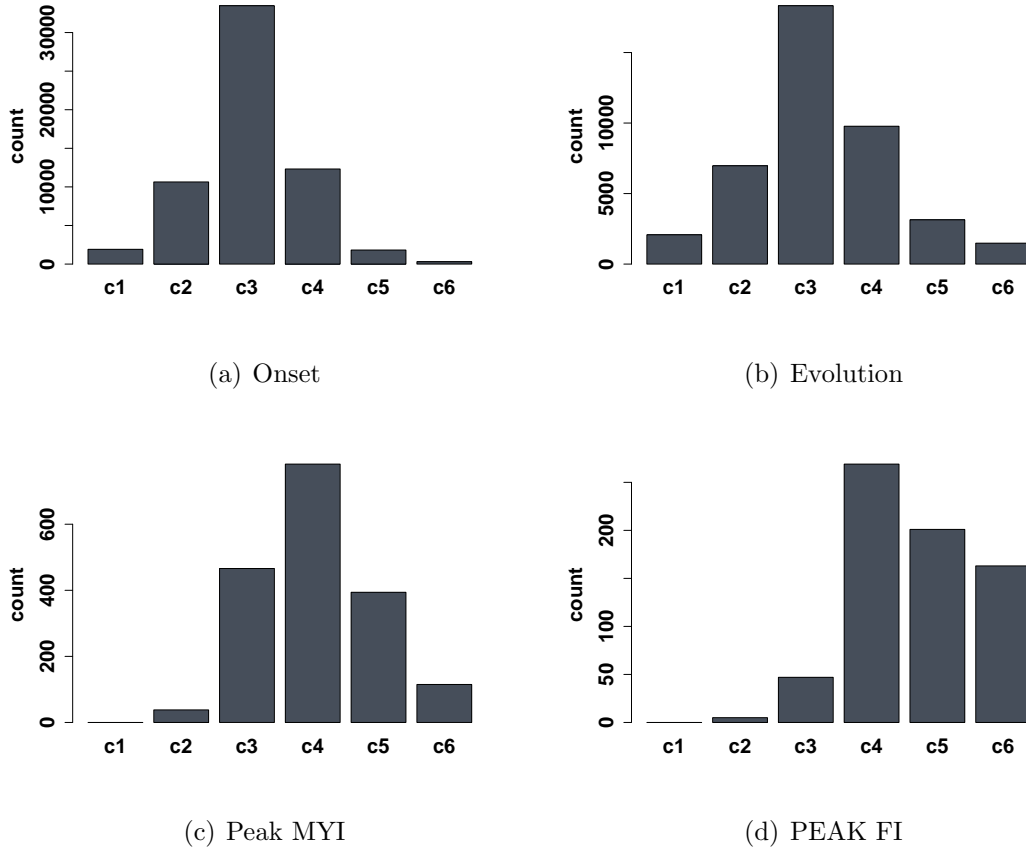
### 3.3 Albedo measurements

Fig. 3.25 shows the shortwave broadband albedo as function of the melt pond fraction for a) the melt pond evolution stage and b) for the peak of melt pond evolution of fast ice. As mentioned before, only the MELTEX campaign included radiation shortwave evaluated data. Thus, no albedo data were available for NO-GRAM and TIFAX flight tracks. As a further restriction, only clear sky tracks could be used for shortwave radiation measurements. So, albedo data were only available sufficiently for the melt pond evolution stage and the peak of melt pond evolution stage of FI.

The red line in Fig. 3.25a were calculated with:

$$\alpha = 0.63 - 0.18 \cdot A_P, \quad (3.1)$$

and in Fig. 3.25b with



**Figure 3.23:** Circularity distribution in absolute numbers. For further description see Fig. 3.24

$$\alpha = 0.49 - 0.35 \cdot A_P. \quad (3.2)$$

$A_P$  describes the melt pond concentration. A almost linear relation between the melt pond concentration and the broadband albedo can be seen for these two melt stages (Fig. 3.25). The outlier with lower albedo can possibly be explained by dark water areas nearby the image who has been measured by the pyranometer. These images were verified to exclude classifications errors.

A mean albedo of  $0.81 \pm 0.01$  was measured for the clear sky flight track on 17<sup>th</sup> May 2008. This flight track correspond to the dry snow stage. On May 26<sup>th</sup>, the measured albedo decreased to  $0.54 \pm 0.05$ . Mainly responsible for this phenomena is the dark blue ice and areas of darker ice. The low melt pond concentration could only be responsible for a very small amount of the decreasing

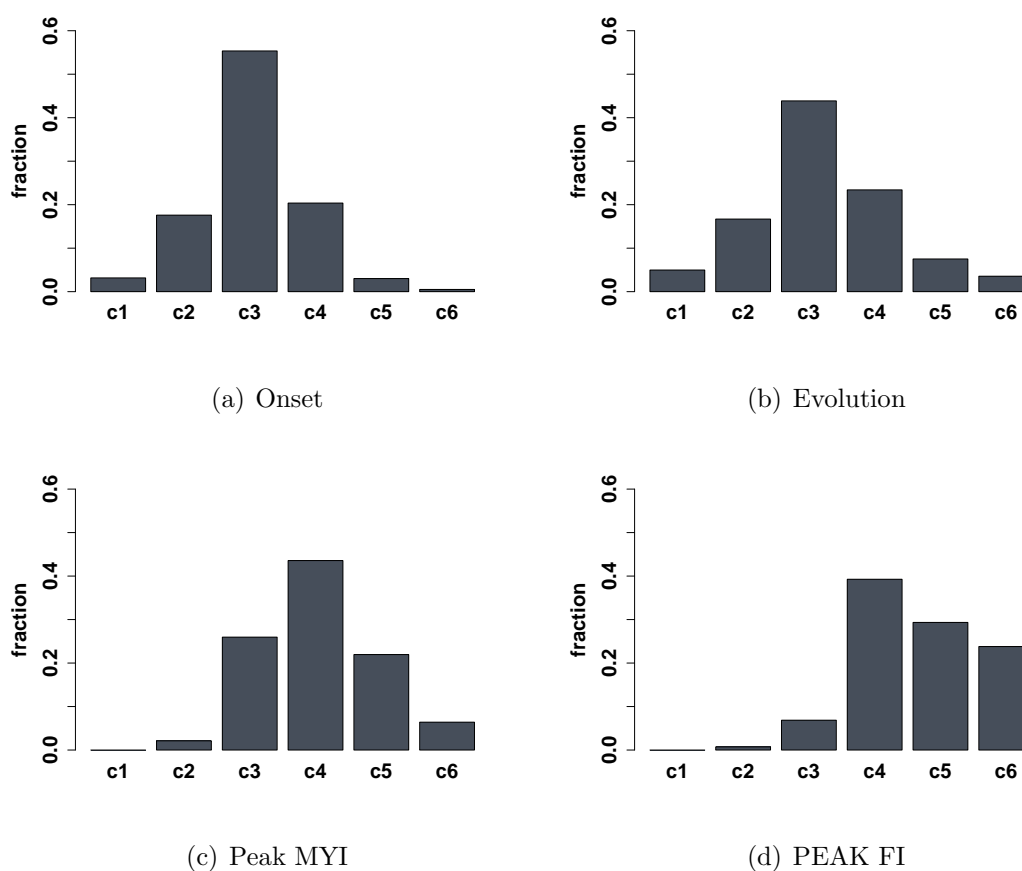


**Figure 3.24:** Circularity percentage distribution. c1 = first shape class ( $C > 0.785$ ), c2 = second shape class ( $0.698 < C < 0.785$ ), c3 = third shape class ( $0.503 < C < 0.698$ ), c4 = fourth shape class ( $0.310 < C < 0.503$ ), c5 = fifth shape class ( $0.174 < C < 0.310$ ) and c6 = sixth shape class ( $C < 0.174$ ).

albedo. Although the mean melt pond coverage amounts to more than 11%, the observed albedo for the 07<sup>th</sup> June is higher with  $0.61 \pm 0.01$ . There were by far less blue or dark ice floes, because the investigated ice floes are thicker than these from the foregoing days. The broadband albedo for 6<sup>th</sup> June over highly ponded and with sediment covered fast ice is very low with  $0.34 \pm 0.05$ .

Fig. 3.26 shows typical histograms of ice floes without leads or only a very small lead fraction for the different melt stages. The absolute grey-scale values can not be compared because the images had a different exposure time. For the OMPF there is a uniform distribution with a peak between 160 and 170 for all three channels (Fig. 3.26a). The influence of the blue ice can be observed for the grey-scale values of the MPES (Fig. 3.26b). Here, the values for the blue channel

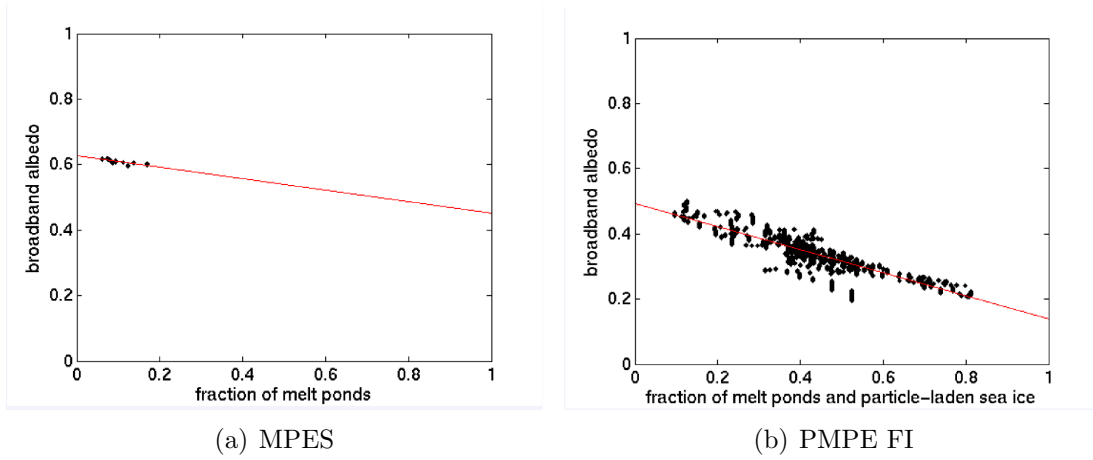


**Figure 3.25:** Albedo measurements for a) the melt pond evolution stage on 7<sup>th</sup> June 2008 over thick FYI (MELTEX) and b) the peak of melt pond evolution stage of FI for 6<sup>th</sup> June 2008 (MELTEX).

(green curve) are higher than for the green- (red curve) and the red channel (black curve). But every channel is still relatively uniform and has only one peak. Later melt stages show a second peak for smaller grey-scale values because of the impact of melt ponds (Fig. 3.26c-f). This second peak is extremely distinct for the PMPE FI with its high melt pond coverage (Fig. 3.26f).



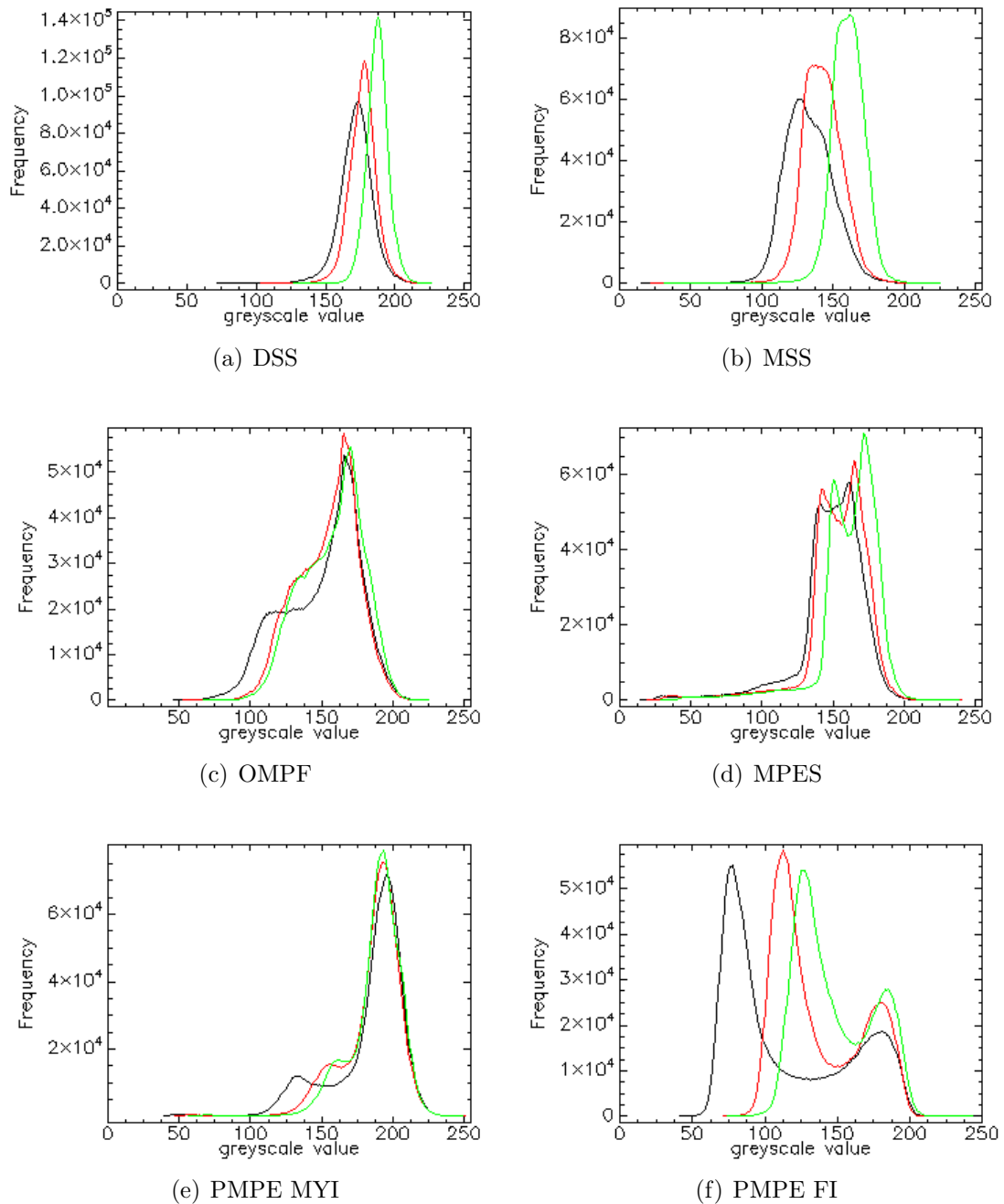


**Figure 3.26:** Histogram plot for a all melt stages. The absolute grey-scale values can not be compared because the images had a different exposure time. Black lines = red channel, red lines = green channel, green lines = blue channel.

## 3.4 Quality assessment

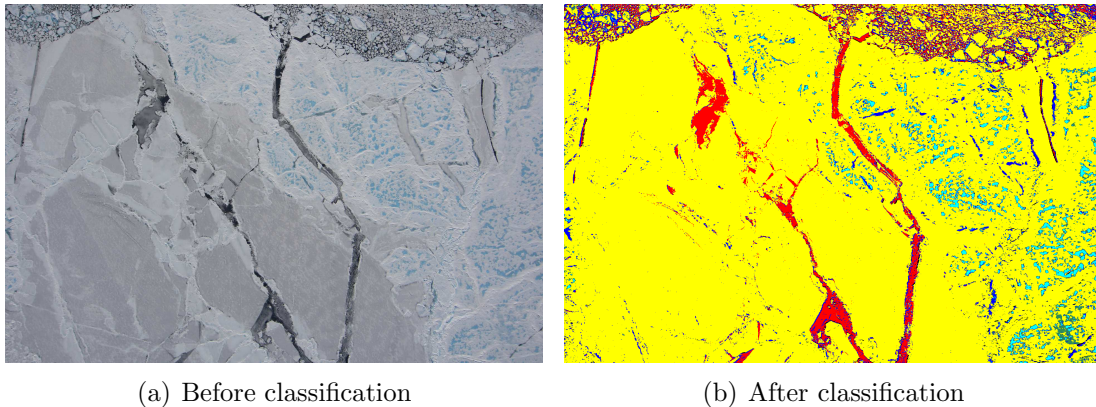
### 3.4.1 Error calculation

Table 3.11 conveyed that some flight tracks were predestinated for a automated classification. These were all homogenous flight tracks with an assessable amount of surface classes. Homogenous flight tracks are mainly all flight tracks, prior to the onset of melt. Furthermore, the fast ice flight track (06<sup>th</sup> June), because it contains only three classes (bare ice, melt ponds, sediment) and most of the flight tracks of the NOGRAM and TIFAX data set. The accuracy of these flights is high, with an error ( $E$ ) smaller than 5%.

**Table 3.11:** Quality assessment of the classified flight tracks.

date	flight track	correct classified pixels	stdev
11.05.2008	complete flight	0.97	0.022
17.05.2008	complete flight	0.96	0.029
26.05.2008	h01	0.86	0.074
	l01	0.84	0.014
	l02	0.88	0.111
03.06.2008	complete flight	0.95	0.223
04.06.2008	h01	0.80	0.103
	l01	0.70	0.205
06.06.2008	complete flight	0.96	0.035
07.06.2008	h01	0.77	0.154
	l01	0.92	0.090
	l02	0.86	0.017
20.08.2010	complete flight	0.97	0.012
20.08.2010	complete flight	0.95	0.025
21.08.2010	complete flight	0.91	0.062
14.07.2011	complete flight	0.96	0.023
21.07.2011	complete flight	0.93	0.045

The flight tracks with a wide range of classes and crossover between these classes are deficient, with  $0.05 < E < 0.2$ . Flight tracks whose error could not be minimised after several iterations, were not evaluated for further use. The only way to classify them accurate enough is to classify the images manually, or to split the flight in more subflight tracks. Furthermore, images were sorted out when 0.05 or more pixels could not be classified. The visual result is very satisfying (Fig. 3.27).



**Figure 3.27:** Example image before and after the classification. Ice floe = yellow, melt pond = cyan, blue ice = blue and thin black ice and water = red. The image was taken on 7<sup>th</sup> June 2008 over thick FYI (MELTEX).

### 3.4.2 Geometric Distortion

Because there is no possibility to correct the images with GCPs, any geometric correction of the images was abandoned. But there is a possibility to estimate the dimension of geometric distortion by means of overlapping images. The change of the size of determined melt ponds at the center of the image was measured. Afterwards the size of these melt ponds at the image margin of the overlapping was measured. Most flight tracks did not contain overlapping images. The few available did not contain necessarily suitable images, where a melt pond occurred at the center and in the overlapping image at the margin. Therefore, only a dozen of images were suitable for this kind of estimation. The ponds at the image margin had on average  $83.3\% \pm 10.4\%$  of the size from the ponds at the center of the images.



# Chapter 4

## Discussion

In the following chapter the results of the investigations will be discussed in comparison to recent studies in the Arctic which described the melt stages and determined the different melt pond parameters. Furthermore, the sources of error and the quality assessment will be discussed.

### 4.1 Characterisation of sea ice melt stages

Perovich et al. (2002a) distinguished five melt stages based on the SHEBA campaign carried out from 20<sup>th</sup> May to 4<sup>th</sup> October 1998. These are the dry snow, melting snow, onset of melt pond formation, pond evolution and freeze-up stages. It is possible to split the melt pond evolution stage into the melt pond evolution and peak of melt pond evolution stage. The six stages can be separated using the reflection values of the aerial photographs, which is a good basis for the segmentation of the images.

The detection of the peak of melt pond evolution was only possible for MYI and FI, but not for FYI. The MELTEX data set ends during the melt season. It is difficult to illustrate an exact temporal process because the flight tracks of single campaigns do not overlap. Even during the same campaign flight tracks were different for each flight and additionally ice floes are moving. Hence, every flight track covered a different area.

In our data, nine surface classes could be distinguished. Dry snow, the merged weathering snow bare ice class, saturated snow for early melt stages, melt ponds,

melting blue ice, sediment, thin grey ice, thin black ice and water. Pixels that could not be identified by the maximum likelihood classifier with a probability threshold of 95% were not classified. Yackel et al. (2000) identified four surface cover types with an unsupervised cluster analysis of digital video data in the Canadian Archipelago. Snow, saturated snow, light and dark melt ponds were distinguished.

## 4.2 Survey of the melt ponds

As mentioned in chapter 3.2, only suitable images have been chosen for the survey of the melt ponds. These images were classified manually for higher accuracy. Therefore, the melt pond concentration calculated from these images can differ from the melt pond concentration calculated for all flight tracks. The minimum size of the investigated melt ponds amounts to  $1 \text{ m}^2$ . That is equivalent to 4 pixels for images with low resolution, and 16 pixels for the highest resolution images from lower flight tracks. The melt pond concentration and the melt pond density are defined in terms of ice floe. Here, water areas are not considered. The TIFAX 2010 flight level data was not accessible early enough, so the pond concentration is the only quantity that was calculated for the freeze-up stage.

### 4.2.1 Melt pond concentration

The investigated area showed a great range of melt pond fraction (Fig. 3.15). For the onset of melt pond formation, some images were still without ponds, while the maximum concentration went up to 18%. The range extended from 3% to 28% for the melt pond evolution stage, 0 to 75% for the peak of melt pond evolution of MYI and for some images of the peak of melt pond evolution, fast ice was ponded to 93%, while on others the relative pond area was low with 2.4%.

Perovich et al. (2002a) observed for the 30<sup>th</sup> June 1998 ice floes with melt pond fractions between 1% and 39% with a mean of 15%. By means of satellite data, Fetterer and Untersteiner (1998) observed a maximum pond concentration of 40% to 50% for flat FYI and 30% on deformed MYI in the Beaufort Sea during melt seasons from 1993 to 1995. Their measured pond fraction for FYI still increased with time, while the pond fraction for MYI decreased. A higher melt

pond fraction for first-year ice than for MYI ice was already observed by Naggar et al. (1998). Nazintsev (1964) observed over a time period of ten melt seasons an increase of melt pond fraction from June to July, and a decrease from July to August for MYI in the central Arctic.

Langleben and Maykut (1977) found a maximum melt pond coverage, a few days after the first appearance of the first melt pond, with a maximum extend of up to 50%. Perovich and Tucker (1997) observed pond coverage of 12% in the Beaufort Sea at the end of July. Under the SHEBA program from 8<sup>th</sup> to 26<sup>th</sup> July 1998 in the Beaufort- and eastern Chukchi Sea, Tschudi et al. (2001) investigated the melt pond coverage. Pond fraction was 24.6% on 8<sup>th</sup> July. It increased to 34.1% on 24<sup>th</sup> July and decreased during the next two days to 26.3% again. Tschudi et al. (2008) measured on 13<sup>th</sup> June 2004 a melt pond fraction of 16.4% in the Beaufort and Chukchi sea (70° N - 80° N). The melt pond fraction considering the underlying ice was classified by Lapp (1982) in the Canadian Archipelago and the Beaufort Sea during early August. He measured an average melt pond coverage of 28% on MYI and 36% on FYI. Holt (1985) observed a surface coverage of 85% to 95% with 3-5 cm of water and almost no snow in Mould Bay (near Beaufort Sea) from about June 25<sup>th</sup> to June 29<sup>th</sup>.

Sankelo et al. (2010) investigated the melt pond evolution in the High Arctic from 24<sup>th</sup> June to 21<sup>st</sup> July 2007. They computed the melt pond fraction by means of digital photographs from digital photographs automatically taken by a camera mounted in the mast of the drifting polar schooner "Tara". The melt pond fraction was about 3% on 24<sup>th</sup> June. On July 1<sup>st</sup> melt ponds already covered 14% of the sea ice surface. The melt pond fraction remained relatively constant with 12% until 15<sup>th</sup> July. Simultaneous temperature remained always below the freezing point. On 21<sup>st</sup> July the melt pond coverage reached its maximum with almost 15%. They estimated the melt pond coverage maximum for August with concentrations higher than 30%.

From Modis data, Rösel et al. (2011) estimated the average melt pond fraction for the two MELTEX flight tracks on 04<sup>th</sup> June and 07<sup>th</sup> June 2008. They used surface-based albedo values who were weighted with the fraction of the corresponding surface class. They determined the three surface classes water, melt

ponds and ice/snow with a spectral unmixing procedure of satellite images based on Tschudi et al. 2008. The average melt pond fraction for the 04<sup>th</sup> June is  $28.4\% \pm 2.5$  and  $21.6\% \pm 8.1$  for the 7<sup>th</sup> June. Their estimated melt pond fraction is much higher than our results. This could have two reasons. The first reason is the different spatial and slightly different temporal resolution. But it is not unlikely that the main overestimation came from the spectral similarity of blue melting ice and melt ponds. So it is possible that Rösel et al. (2011) classified blue melting ice as melt ponds.

Rösel et al. (2012) estimated also the spatial and temporal evolution of the melt pond fraction in the Arctic, between 9<sup>th</sup> May and 6<sup>th</sup> September 2011 by means of MODIS Data. Melt pond fractions with values below 20% are calculated for the northern Beaufort Sea, the Chukchi Sea, the Laptev Sea and the Central Arctic. The melt pond fractions in the Beaufort Sea increased strongly after 18<sup>th</sup> June. The highest melt pond fractions were measured for the Canadian Archipelago with values over 30%.

## 4.2.2 Melt pond size

The mean melt pond sizes fluctuated between  $24 m^2$  for the onset of melt pond formation and the melt pond evolution to  $43 m^2$  for the peak of melt pond evolution of MYI to  $142 m^2$  for the peak of evolution of FI. The median melt pond size was significantly smaller with  $7 m^2$  for the OMPF and MPES. Even smaller values were reached for the PMPE MYI and PMPE FI with  $4 m^2$ . This can be explained with the extreme interconnections of melt ponds and the influence of a few very large melt ponds in contrast to many small melt ponds. The biggest melt ponds were  $47,562 m^2$  for PMPE MYI and  $40,643 m^2$  for PMPE FI which is more than 1100 times the mean melt pond size of PMPE MYI and almost 300 times the mean melt pond size of PMPE FI.

The investigation of Perovich et al. (2002a) also revealed that the median of the investigated melt pond areas were up to seven times less than the mean pond areas. Their mean melt pond size for the 8<sup>th</sup> June 1998 was  $15 m^2$ . The melt pond coverage at this time was about 2%. The mean melt pond size and coverage increased to almost  $60 m^2$  and 20% on 22<sup>nd</sup> June. The mean size decreased again



**Table 4.1:** Comparison of the different melt pond quantities with preceding observations.

Author	Location	Date	Conc [%]	Size [ $m^2$ ]	Density [ $km^{-2}$ ]	Shape	$\alpha$
Own results (2013)	Beaufort Sea (FYI)	07.06.2008	10.7	24	4842	0.54	0.34-0.81
	Beaufort Sea (FI)	06.06.2008	39.2	142	2890	0.30	
	Northly of Greenland (MYI)	21.07.2011	19.1	43	4664	0.40	
Fetterer and Untersteiner (1998)	Beaufort Sea (FYI)	Summer	40-50	-	-	-	-
	Beaufort Sea (MYI)	1993-1995	30	-	-	-	-
Yackel et al. (2000)	Wellington Channel	30.07.1997	10-20	-	-	-	-
Perovich et al. (2002a; 2002b)	Beaufort Sea	07.08.1998	24	60	4600	0.31	0.4-0.9
Skyllingstad et al. (2007)	-	40 Days simulation	-	22	-	-	0.46-0.57
Tschudi et al. (2008)	Beaufort & Chukchi Sea	30.06.2004	16.4	-	-	-	-
Rösel et al. (2011)	Beaufort Sea	07.06.2008	28.4	-	-	-	-
Lüpkes et al. (2012)	Arctic Ocean	1999-2001	0-41	2.4 131	0	-	- 4000

to about  $39 m^2$  on 24<sup>th</sup> June (melt pond coverage about 13%). This decrease probably results from drainage of some melt ponds. On 5<sup>th</sup> August the mean melt pond size was almost  $60 m^2$  again. Melt pond coverage was about 25% at that time. The median melt pond size amounted to constantly under  $10 m^2$  for the measurements of Perovich et al. (2002a). The maximum median size was  $8.5 m^2$  on 30<sup>th</sup> June. Tschudi et al. (2008) measured median melt pond sizes between  $14.1 m^2$  to  $16.9 m^2$  from 8<sup>th</sup> July to 24<sup>th</sup> July during the SHEBA campaign. The median melt pond size decreased to  $9.2 m^2$  on 26<sup>th</sup> July.

Fig. 4.1 shows the observed mean melt pond size as points (Fetterer et al., 2008) and the parametrization assuming ponds as squares as line (Lüpkes et al., 2012). The smallest available melt pond sizes for the satellite data set was  $1 m^2$ .

The parametrization is as follows

$$D'_w = D_{min} \cdot A + D_{max} \cdot (1 - A), \quad (4.1)$$

with  $D_{min}$  the minimum ice floe length is equal to 2.26 m and  $D_{max}$  the maximum ice floe length is equal to 24.63 m (Lüpkes et al., 2012). Lüpkes et al. (2012) assumed the pond shape as a square. So  $S_P$  can be calculated from

$$S_P = (D'_w)^2. \quad (4.2)$$

That implies an average melt pond size of 12.19  $m^2$  for a melt pond concentration of 3.5% and a lead fraction of 2%. The mean melt pond size increases to 26.25  $m^2$  for melt pond concentration of 11.8% and a lead fraction of 1%. For a concentration of 20% the average melt pond size amounts to 45.35  $m^2$ . The melt pond size further increases to 131  $m^2$  for a concentration of 41%. For this calculation the lead fraction has to be involved.

It must be assumed that the melt ponds for the onset of melt pond formation stage are on average slightly smaller. They might be a little overestimated, because the investigation area contained images with a bit higher melt pond concentration for a better distinction of the melt pond from the surrounding ice (Section 3.2). The calculations of Lüpkes et al. (2012) substantiate this assumption. It has also to be considered that it is very difficult to mark down exactly the exact melt pond edges for the OMPF.

### 4.2.3 Melt pond size distribution

The melt pond size distribution affects the overall size of the melt pond edge length. The observed melt ponds showed a clear dominance of ponds with an area smaller than 100  $m^2$ . Their percentage amounted to about 90% for all melt stages. The melt pond distribution is positive skewed and extremely leptokurtic. Yackel et al. (2000) and Perovich et al. (2002a) also measured a highly skewed melt pond distribution with a significant greater amount of small ponds. A clear dominance of melt ponds which are smaller than 100  $m^2$  were observed by Tschudi et al. (2001).

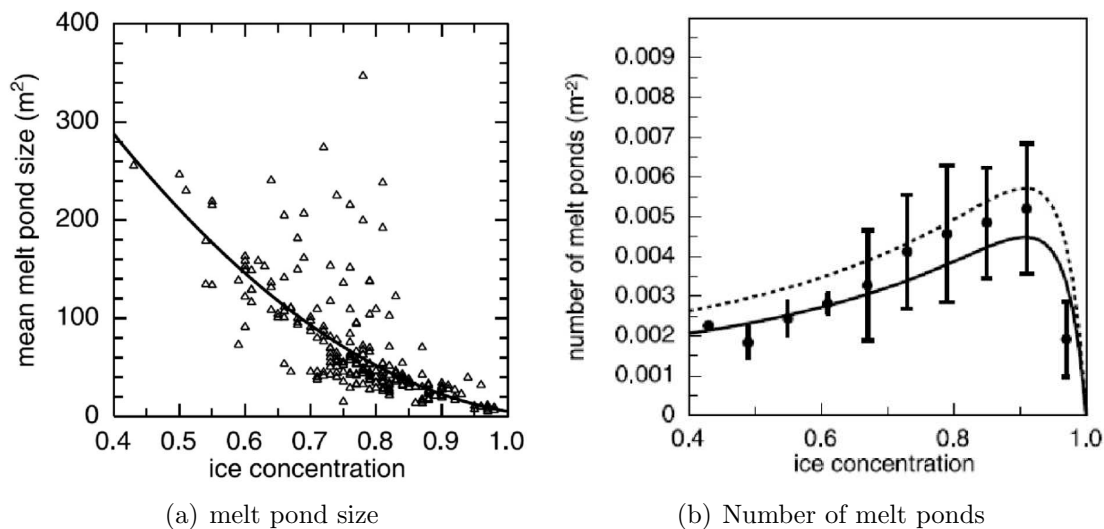


**Figure 4.1:** a) Observations (Fetterer et al., 2008) of mean pond size (area) and parametrization assuming ponds as squares. The solid line is calculated by equation 4.1 (Lüpkes et al., 2012). b) Number of melt ponds per square meter as calculated with equation (1.1) assuming quadratic (solid line) and circular (dashed line) ponds. Symbols represent NSIDC data (Fetterer et al., 2008), which were averaged in classes with 10% steps in ice concentration (Lüpkes et al., 2012).

#### 4.2.4 Melt pond density

Pond density is defined as the number of ponds divided by the area of ice and ponds, with units of ponds per  $km^2$ . It amounted to  $1497 km^{-2}$  for the OMPF for a melt pond coverage of 3.5%. It increased for the MPES to  $4842 km^{-2}$  for an average melt pond concentration of 11.8%. It decreased to  $4664 km^{-2}$  for PMPE MYI for an average melt pond concentration of 20% and further decreased to  $2886 km^{-2}$  for an average melt pond coverage of 41% during the PMPE FI.

Similar results were observed by Perovich et al. (2002a). They investigated four flight tracks on 10<sup>th</sup>, 22<sup>nd</sup>, 30<sup>th</sup> June and 7<sup>th</sup> August. 350,000 melt ponds were investigated. The melt pond number densities also showed considerable variation from  $1826 km^2$  to  $4318 km^2$  during this observation period. Lüpkes et al. (2012) calculated the melt pond density by means of NSIDC data (Fetterer et al., 2008) dependent on the ice concentration ( $A$ ) and the melt pond shape (Fig. 4.1b). The concentration melt ponds and leads ( $A_p$ ) was calculated by the following equation:

$$A_p = 1 - A. \quad (4.3)$$

Since the percentage of leads (water) is very small for the MPES, PMPE MYI and PMPE FI, one has

$$A_p \approx A_P, \quad (4.4)$$

with the melt pond concentration ( $A_P$ ) and therefore

$$A_P \approx 1 - A. \quad (4.5)$$

This approach is not valid for the onset of melt pond evolution, because the lead fraction preponderates for small melt pond fractions. Fig. 4.1b shows a melt pond density range from  $2000 \text{ km}^{-2}$  up to over  $5000 \text{ km}^{-2}$  for  $0 < A_P < 60\%$ . The maximum melt pond density were reached for a melt pond concentration of about 20%. It also shows that the melt pond density is higher for melt ponds with a circular shape than for melt ponds with a square shape.

### 4.2.5 Melt pond density distribution

The melt pond density distribution also shows the clear dominance of small melt ponds and only a small amount of large melt ponds (100 m - 10,000 m). Very large melt ponds with an area larger than  $10,000 \text{ m}^2$  only occurred very rarely and only for the peak of melt pond evolution stage of MYI and FI. But their influence of the mean melt pond size is substantial.

### 4.2.6 Melt pond shape

A problem for the shape determination, especially for small melt ponds, is the fact that the shape of a pixel corresponds to a square. So a  $1 \text{ m}^2$  small melt pond with a low resolution of 4 pixels can not get a higher circularity than a square. This problem declines for larger ponds. In the investigation area the average circularity decreased from 0.57 for the onset of melt pond formation to 0.54 (MPES), 0.4 (PMPE MYI) and 0.3 (PMPE FI). For comparison a rectangle with an aspect ratio of 1:2 has circularity of 0.7, a 1:4 rectangle 0.5 and a 1:8 rectangle 0.3. So, the shape got more complex throughout the melting season. Perovich (2002a) calculated the "Perovich circularity" ( $C_P$ ) with

$$C_P = \frac{U^2}{S_p}. \quad (4.6)$$

It is different from  $C$  calculated in eq. 2.10.  $C_P$  is  $4\pi$  for circle and increases for more a complex forms.  $C$  has a value range between 0 and 1 and it is easier to handle.  $C$  decreases for more complex forms and drops to zero for a line. The mean circularity ( $C_P$ ) indicated by Perovich et al. (2002a) for melt ponds ranged from 38.5 (10<sup>th</sup> June) to 41.2 (7<sup>th</sup> August). For comparison,  $C_P$  for a 1:8 rectangle is 40.5 (Perovich et al., 2002a). Converting  $C_P$  calculated by Perovich et al. (2002a) into  $C$ , one gets values between 0.31 and 0.33. So the shape observed by Perovich et al. (2002a) also got more complex throughout the melting season, but in a much smaller range.

#### 4.2.7 Melt pond shape distribution

The percentage and the absolute circularity distribution are shown in Fig. 3.24 and Fig. 3.23. Six shape class were defined (see 3.2.7). For the onset of melt pond formation and the melt pond evolution stage the shape class number three dominates. For the peak of melt pond evolution of MYI and FI most melt ponds are related to shape class number 4 which contains more complex shapes.

### 4.3 Albedo measurements

For the MPES equation 3.1 shows an albedo range from 0.63 for 100% sea ice coverage, to 0.45 for 100% melt pond coverage, described by a linear function. For PMPE FI equation 3.2 shows a albedo range from 0.49 for 100% sea ice coverage to 0.14 for 100% melt pond coverage. Eicken et al. (1994) measured melt pond albedo values between 0.14 for sediment covered melt ponds and 0.30 for clean melt ponds with depths smaller than 30 cm. Other albedo observations show values between 0.5-0.7 for bare ice, 0.2 to 0.4 for melt ponds and 0.1 for leads (Chernigovskiy, 1963; Langleben, 1971; Grenfell and Maykut, 1977).

The observed mean albedo was  $0.81 \pm 0.01$  for the dry snow stage (17<sup>th</sup> May 2008). The snow was probably already a little wet and therefore the grain size was slightly increased. Mainly dark and blue ice areas were responsible for a strong decrease to  $0.54 \pm 0.05$  for 26<sup>th</sup> May 2008. The small melt pond areas, with

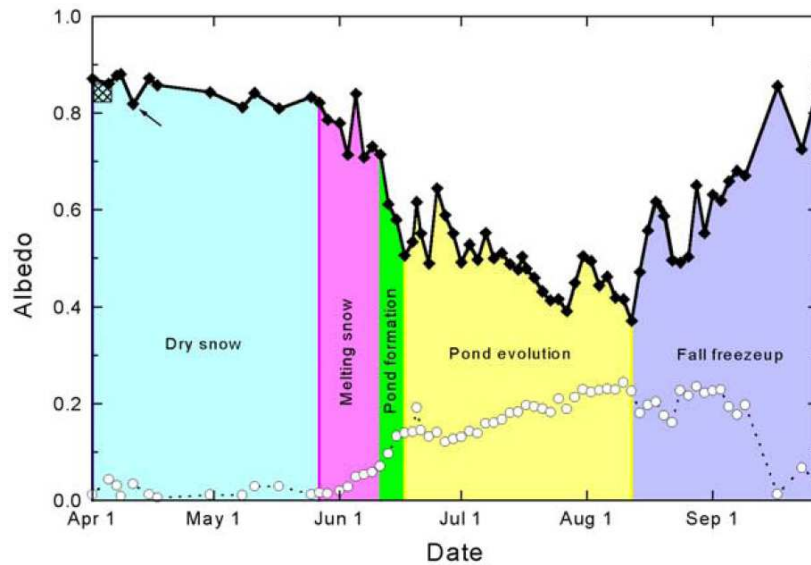


**Figure 4.2:** Time series of wavelength-integrated albedo from 1 April 1998 through 27 September 1998. Values are averaged over a 200-m-long albedo line. The arrow points to 17 April when the sky was clear. Also plotted is the albedo measured at the beginning of the experiment in October 1997 (solid squares). The standard deviation of albedo measured along the albedo line for each is plotted as open circles (Perovich, 2002b).

concentrations smaller than 2% had probably a very small influence. This assumption gets supported by the fact that the mean albedo is higher for the melt pond evolution stage of thick FYI, which was  $0.61 \pm 0.01$ . The melt pond coverage at this time was more than 11%, but this thicker ice contained less blue or dark ice floes. Very low albedo values ( $0.34 \pm 0.05$ ) were measured for the flight on 6<sup>th</sup> June 2008 over fast ice. The melt pond concentration was about 39.3% at this time and a lot of melt ponds and ice floes were covered with sediment. So, a crucial factor for the average broadband albedo beside the pond concentration is the underlying ice regime with its related ice thickness.

During the SHEBA campaign, Perovich et al. (2002b) measured albedo values between 0.8 to 0.9 for April and May with a small spatial variability (Fig. 4.2). A rainfall event at the end of May caused an increase of the snow grain size to about 1 mm diameter. Thus, the albedo decreased from 0.8 to 0.7. During the mid of June the albedo decreased from 0.7 to 0.5 within a week, due to melting. The smallest melt pond values were measured in August. The mean albedo amounted to 0.4 with a great spatial variability ranging from 0.1 to 0.65 with a standard deviation of 0.25. From time to time, when temperature fell under freezing point again, refrozen ponds caused an increase of 0.1 of the average albedo. Average

albedo returned to their springtime maxima of 0.8 to 0.9 and were spatially uniform again by the end of September (Perovich et al., 2002b). Skyllingstad et al. (2007) simulated total albedo values ranging from 0.57 to 0.46 in their 40 days simulation period.

## 4.4 Quality assessment

For the calculated melt pond statistics, only melt ponds were chosen whose sizes were bigger than  $1 \text{ m}^2$ . That implies a minimum of four pixels for the images with the worse resolution and minimum of 16 pixels for the low flight tracks with the best resolution. Perovich (2002a) eliminated all melt ponds that were smaller than 12 pixels, which means that the minimum size of his investigated melt ponds was  $2 \text{ m}^2$ . 4 Pixels should be accurate enough because the images for statistic calculation were classified manually.

### 4.4.1 Sources of error

A source of error for automated classification of the images of the three campaigns is the variable exposure of the Canon camera. Big dark areas, like water or very thin ice, are higher exposed than areas with a lot of snow or bare ice. Hence, it is possible to have different gray scale values for the same classes. This source of error could be minimised by sorting the images in flight tracks with similar conditions.

Another problem is the crossover of some classes. There are frequently crossovers from the snow to saturated snow to light ponds to dark ponds to thin black ice to water. Dark ponds and blue bare ice have a spectral similarity. For some flight tracks, especially over fast ice, there are sediments on the ice or in the melt ponds. The aerial fraction of sediment goes up to 10% and there is almost no difference in the spectral signature of sediment covered ice and sediment covered ponds. For the evaluation of the radiation, it is useful to treat the sediment class like dark melt ponds. Sometimes, mixed pixels are a problem, especially at the transition from water to an ice floe. A very small effect are shadows along the ridges. Shadowed bare ice areas are often wrongly classified as blue ice. But even for images with a high amount of ridges, maximal every hundredth pixel is

affected. So it is a negligible effect. An even much smaller effect are floe edges which are under water. They got classified as melt ponds, because there is no spectral difference. The NOGRAM and TIFAX images are much more homogeneous and the edges between the different classes are sharper so that the number of wrong classified pixel is much less.

#### 4.4.2 Geometric Distortion

The few images that were suitable for a estimation of the geometric distortion yield that melt ponds at the image margin had on average  $83.3\% \pm 10.4\%$  of the size from the ponds at the center of the images. So the mean melt pond size is probably underestimated because of geometric distortion and the fact that large melt ponds did not always get recorded on a image in their full size.



# Chapter 5

## Conclusions and Outlook

This study examined the sea ice melt stages in the melt season for the arctic summer over FI, thin and thick FYI and MYI. Furthermore, the determination of the melt pond fraction, melt pond area and perimeter, melt pond size distribution, the melt pond density and density distribution, the shape of the melt ponds and the melt pond shape distribution was accomplished. These parameters influence the momentum flux (Lüpkes et al., 2012) and are important to improve the simulation of melt pond evolution in sea ice models.

Three flight campaigns (MELTEX 2008, NOGRAM 2011 and TIFAX 2010) were chosen to accomplish that aim. Six different melt stages could be distinguished: the dry snow stage, the melting snow stage, the onset of melt pond formation stage, the melt pond evolution stage, the peak of melt pond evolution stage and the freeze-up stage. Every stage has its significant range of melt pond quantities and albedo values. The results confirm a great spatial and temporal variability for all observed sea ice melt stages and melt pond quantities. The average melt pond concentrations ranged from 1.6% to 39.3% for the different melt stages and ice regimes in the investigated areas. Melt pond concentrations from 2.4% to 92.6% per ice floe were measured during one flight track. Mean melt pond sizes varied between  $24 \text{ m}^2$  and  $142 \text{ m}^2$  in dependency of melt stage and ice regime with a huge standard deviation, especially for the late melt stages. The smallest observed melt ponds had a size of  $1 \text{ m}^2$ . That corresponds to the size of four to sixteen image pixels dependent on the flight level. The biggest observed melt pond had an extent of  $47,562 \text{ m}^2$ . The melt pond density (number of ponds per  $\text{km}^2$ ) ranged from  $1497 \text{ km}^{-2}$  to  $4842 \text{ km}^{-2}$ . The highest pond densities were

reached for an average pond concentration of 11.8%. There is a clear quantitative dominance of small ponds. Over 90% of the ponds are smaller than 100  $m^2$  for all melt evolution stages and types of ice. This quantitative dominance is also shown by the positive skewed and extremely leptokurtic melt pond size distribution. The mean calculated circularity lies in between 0.57 and 0.30. Larger melt ponds show on average a smaller circularity than smaller.

The broadband albedo measured during the MELTEX campaign ranged from  $0.81 \pm 0.01$  to  $0.34 \pm 0.05$  depending on the melt pond concentration, sediment cover and the underlying ice regime with its related ice thickness. This is in line with the results from Perovich et al. (2002a).

The results show that an automatic classification is practicable, but needs some time for the pre- and postprocessing. In further studies it will be important to determine the measured quantities also for leads and sea ice floes. It is necessary to investigate more cases of the late melt stages to verify the results.

Future work will be carried out using data of the MELTEX-II aircraft campaign planned for 2014. The focus will be set on both the initial and the peak period of melting. During that campaign, parameters that influence broadband and spectral albedo of ponded ice on FYI as well as MYI ice will be investigated. Therefore, the campaign will be performed over the Fram Strait and the Lincoln Sea. In addition to the melt pond fraction, the ice thickness and the melt pond depth as further key parameters influencing summer sea ice albedo will be measured. Further plans include the combined performance of aircraft and in situ ground based measurements (Birnbaum et al., 2012). Overlapping flight tracks would be very useful to get a real time series. That will be a good improvement of the work done until now.

# List of Figures

1.1	Spectral albedo observed over snow and melt ponds . . . . .	4
1.2	Spectral albedo observed over bare sea ice . . . . .	5
2.1	Investigation area MELTEX . . . . .	13
2.2	Example flight MELTEX . . . . .	15
2.3	2 m Temperature profile MELTEX 2008 . . . . .	17
2.4	Investigation area of NOGRAM 2011 . . . . .	18
2.5	2 m Temperature profile NOGRAM 2011 . . . . .	19
2.6	Example flight TIFAX . . . . .	20
2.7	2 m Temperature profile TIFAX 2010 . . . . .	21
2.8	The different ice regimes in the investigation areas . . . . .	23
2.9	Maximum likelihood classifier . . . . .	25
2.10	Scatter plot (region of interessts) . . . . .	27
2.11	Geometric Distortion . . . . .	30
3.1	Dry snow stage . . . . .	34
3.2	Dry snow stage class distribution . . . . .	35
3.3	Melting snow stage . . . . .	36
3.4	Melting snow stage class distribution . . . . .	37
3.5	Onset of melt pond formation . . . . .	38
3.6	Onset of melt pond formation class distribution . . . . .	39
3.7	Melt pond evolution stage . . . . .	40
3.8	Melt pond evolution stage class distribution . . . . .	41
3.9	Peak of melt pond evolution stage MYI . . . . .	42
3.10	Peak of melt pond evolution stage fast ice . . . . .	43
3.11	Peak of melt pond evolution stage MYI class distribution . . . . .	43
3.12	Peak of melt pond evolution stage fast ice class distribution . . . . .	44
3.13	Freeze-up stage . . . . .	45

3.14	Freeze-up stage class distribution . . . . .	46
3.15	Melt pond concentration . . . . .	48
3.16	Melt pond size . . . . .	50
3.17	Melt pond size distribution . . . . .	51
3.18	Melt pond size (accumulated frequency) . . . . .	52
3.19	Melt pond density . . . . .	53
3.20	Melt pond density distribution . . . . .	54
3.21	Average circularity . . . . .	56
3.22	Circularity in dependence of the melt pond perimeter . . . . .	57
3.23	Circularity absolute distribution . . . . .	60
3.24	Circularity percentage distribution . . . . .	61
3.25	Albedo measurements over FYI and FI . . . . .	62
3.26	Histogram plot for all melt stages . . . . .	63
3.27	Image classification . . . . .	65
4.1	Melt pond size and density . . . . .	73
4.2	Albedo melt stages . . . . .	76

# List of Tables

2.1	Aircraft instruments operated on POLAR 5 . . . . .	15
3.1	Dry snow stage class distribution . . . . .	34
3.2	Melting snow stage class distribution . . . . .	36
3.3	Onset of melt pond formation class distribution . . . . .	38
3.4	Melt pond evolution stage class distribution . . . . .	40
3.5	Peak of melt pond evolution MYI class distribution . . . . .	41
3.6	Peak of melt pond evolution fast ice class distribution . . . . .	42
3.7	Freeze-up stage class distribution . . . . .	45
3.8	Melt pond quantities . . . . .	47
3.9	Circularity absolut distribution . . . . .	59
3.10	Circularity percentage distribution . . . . .	59
3.11	Quality assessment of the classified flight tracks . . . . .	64
4.1	Comparison of the melt pond quantities . . . . .	71



# List of Abbreviations and Symbols

## Symbols

$\alpha$	broadband shortwave albedo
$\alpha_s$	spectral shortwave albedo
$a_c$	percent probability that any candidate pixel is a member of class c
$A$	sea ice concentration defined by Lüpkes et al. (2012) with $A = 1 - S_p$
$A_p$	concentration of melt ponds and leads
$A_P$	concentration of melt ponds
$C$	circularity ( $\frac{4\pi * S_p}{U^2}$ )
$C_P$	circularity ( $\frac{U^2}{S_p}$ ) calculated by Perovich et al. (2002a)
$c'_s$	shape parameter for floes and melt ponds
$D_{max}$	maximum ice floe length
$D_{min}$	mininum ice floe length
$D$	weighted distance
$D'_w$	cross wind dimension of a melt pond or floe
$E$	calculated classification error
$f_l$	focal length
$h$	fligth level
$h_p$	the elevation of ice surface relative to the water surface in ponds or leads
$I_{ps}$	image pixel size
$I_s$	image scale
$I_{si}$	image size
$I_l$	image length
$I_w$	image width
$M_c$	the mean vector of the sample of class c

$n_a$	number of all pixels
$n_c$	number of correct classified pixels
$N_P$	number of ponds and leads
$N_{mp}$	number of melt ponds
$n_{pl}$	number of pixel (length)
$n_{pw}$	number of pixels (width)
$P_d$	dynamic pressure, depending on the square of the wind velocity
$PD$	melt pond density (number of melt ponds per $km^2$ )
$S \downarrow$	downward short wave radiation
$S \uparrow$	upward shortwave radiation
$s_l$	camera sensor length
$S_P$	area of an individual pond or lead
$S_{pun}$	unscaled melt pond size
$S_t$	domain area with N floes or with ponds and leads
$s_w$	camera sensor width
$T$	transposition function
$\tau_d$	momentum flux
$U$	perimeter of melt pond
$U_{un}$	unscaled melt pond perimeter
$X$	the measurement vector of the candidate pixel
$y$	a particular class



## Abbreviations

**BRDF** Bidirectional reflectance distribution function

**DSS** Dry snow stage

**FI** Fast ice

**FUS** Freeze-up stage

**FYI** First-year ice

**GCP** Ground control point

**MELTEX** Aircraft campaign to investigate the impact of melt ponds on energy and momentum fluxes between atmosphere and sea ice. MELTEX was realized in the Beaufort Sea in 2008.

**MPES** Melt pond evolution stage

**MSS** Melting snow stage

**MYI** Multi-year ice

**NSIDC** National Snow and Ice Data Center

**NTM** National Technical Means

**NOGRAM** Campaign to investigate of the offshore magnetics and gravity anomalies in the easterly Morris Jessup Rise (2011)

**OMPF** Onset of melt pond formation

**PMPE FI** Peak of melt pond evolution for fast ice

**PMPE MYI** Peak of melt pond evolution for multi-year ice

**SHEBA** A coordinated project to investigate the role of arctic climate in global change in the year 1998 (65°N to 90°N latitude and 180°W to 120°W longitude).

**TIFAX** Campaign in the Fram Strait and in the area of north Greenland (2010). Main goal was to monitor the thickness of the sea ice which leaves the Arctic through the Fram Strait during summer months.



# Glossary of Ice Terminology

## Important terms and definitions (Carsey et al., 1994)

**Crack:** Any fracture that has not yet parted.

**Fast ice:** Sea ice of any origin that remains fast, attached with little horizontal motion, along a coast, or to some other fixed object.

**First-year ice:** Sea ice of not more than one winter's growth, developing from young ice and having a thickness of 0.3 m to 3 m. May be subdivided into thin first-year or white ice (0.3 m - 0.7 m), medium first-year ice (0.7 m - 1.2 m), and thick first-year ice (over 1.2 m)

**Flooded Ice:** Sea Ice that has been flooded by meltwater or river water and is heavily loaded with water and wet snow.

**Fracture:** Any break or rupture through very close, compact, or consolidated pack ice (see concentration), fast ice, or a single resulting from deformation processes cf. Lead). Fractures may contain brash ice and be covered with nilas or young ice. Their length may be a few meters or many kilometers.

**Frazil ice:** Fine spicules or plates of ice suspended in water. It also sometimes forms at some depth, at an interface between water bodies of different physical characteristics, and floats to the surface. It may rapidly cover wide areas of water.

**Freeboard:** The distance, measured normal to the sea surface, between the upper surface of the ice and the water level.

**Grease ice:** A stage of freezing, later than that of frazil ice, in which the crystalline have coagulated to form a soupy layer on the surface. Grease ice reflects little light, giving the sea a matte appearance.

**Gray ice:** Young ice, 10 - 15 cm thick. Less elastic than nilas, it breaks on swell. Usually it rafts under pressure.

**Gray-white ice** Young ice, 15 cm - 30 cm thick. Under pressure, it is more likely to ridge than to raft.

**Ice cake:** Any relatively flat piece of sea ice less than 20 m across (cf. Floe). If less than 2 across, it is small ice cake. **Ice cover:** The ratio of an area of ice of any concentration to the total sea surface within some large geographic locale; this local may be global, hemispheric, or prescribed by a specific oceanographic entity, such as Baffin Bay or the Barents Sea.

**Ice edge:** The demarcation at any given time between the open sea and sea ice of any kind, whether fast or drifting. Internationale Code:

**Lead:** Any fracture or passage through sea ice that is generally too wide to jump across. A lead may contain open water (open lead) or be ice-covered (frozen lead).

**Melt pond:** An accumulation of meltwater on the surface of sea ice that, because of appreciable melting of the ice surface, exceeds 20 cm in depth, is embedded in the ice (has distinct banks of ice), and may reach tens of meters in diameter.

**Pack ice:** Any accumulation of sea ice, other than fast ice, no matter what form it takes or how it is disposed (cf. concentration).

**Polynya:** Any nonlinear shaped opening enclosed in ice. Polynias may contain brash ice or be covered with new ice, nilas or young ice. If limited on one side by the coast, it is called shore polynia; if limited by fast ice, it is called a flaw polynia. If found in the same place every year, it is called a recurring polynia.

**Pressure ridge:** A general expression any elongated (in plan view) ridge like accumulation of broken ice caused by ice deformation.

**Rafting:** Process whereby one piece overrides another; most obvious in new and young ice (cf. Finger rafting), but common in ice of all thicknesses.

**Ridging:** The process whereby ice is deformed into ridges.

**Second-year ice:** Old ice that has survived only one summer's melt. Because it is thicker and less dense than first-year ice, it stands higher in the water. In contrast to multi-year ice, second-year ice during the summer melt shows a regular pattern of numerous small ponds. Bare patches and ponds are usually greenish blue.

**Slush:** Snow that is saturated and mixed with water on land or ice surfaces, or forms as a vicious mass floating in water after a heavy snowfall.

**Snow ice:** The equigranular ice that is produced when slush freezes completely.

**Young ice:** Ice in transition stage between nilas and first-year ice, 10 cm - 30 cm thickness. May be subdivided into gray ice and gray white ice. Young ice is also commonly used in a more general way to indicate the complete ice thickness between 0 - 30 cm (as in the formation and growth of young ice). Usually these differences in meaning are clear from the context of the discussion.



# Acknowledgements

Mein ganz besonderer Dank geht an Dr. Gerit Birnbaum und Dr. Wolfgang Dierking vom Alfred-Wegener-Institut Helmholtz-Zentrum für Polar- und Meeresforschung für die sehr gute und sehr umfangreiche Betreuung während meiner Diplomarbeit. Dem Alfred-Wegener-Institut danke ich für die Bereitstellung der Messdaten und der Software idl/envi. Des Weiteren möchte ich Herrn Prof. Dr. Günther Heinemann und Herrn Prof. Dr. Markus Casper für die Begutachtung und Betreuung meiner Arbeit danken.

Auch möchte ich mich bei Dr. Christof Lüpkes, Dr. Vladimir Gryanik, Dr. Thomas Krumpfen, Dr. Stefan Hendricks, Dr. Jörg Hartmann, Wolfgang Cohrs, Dr. Marcel Nicolaus, Paul Lehmann, Dr. Jennifer Sobiech und Dr. Daniel Steinhaage vom Alfred-Wegener-Institut für ihre Unterstützung bedanken. Ein besonderes Dankeschön geht an Basil Neff von der Universität Basel für die Optimierung der IDL-Skripte. Ich bedanke mich bei Daniel Kramer, Kora Mejer, Stephan Paul und Lena Neuhardt, die meine Arbeit ganz oder teilweise korrekturgelesen haben. Ein weiteres Dankeschön geht an Anne Menkhaus, unsere stets hilfsbereite Sekretärin der Umweltmeteorologie. Zu guter Letzt möchte ich meinen Eltern und meiner Schwester danken.

---

Special thanks go to my friend C.J. Snare.





# References

- Andreas, E. L., Horst, T. W., Grachev, A. A., Persson, P. O. G., Fairall, C. W., Guest, P. S., and Jordan, R. E. (2010). Parametrizing turbulent exchange over summer sea ice and the marginal ice zone. *Quarterly Journal of the Royal Meteorological Society*, 136(649):927–943.
- Barber, D., Hanesiak, J., Chan, W., and Piwowar, J. (2001). Sea ice and meteorological conditions in northern baffin bay and the north water polynya between 1979 and 1996. *Atmosphere-Ocean*, 39(3):343–359.
- Barber, D. G. and Yackel, J. (1999). The physical, radiative and microwave scattering characteristics of melt ponds on arctic landfast sea ice. *International Journal of Remote Sensing*, 20(10):2069–2090.
- Barry, R., Serreze, M., Maslanik, J., and Preller, R. (1993). The arctic sea ice-climate system: Observations and modeling. *Reviews of Geophysics*, 31(4):397–422.
- Barry, R. G. (1996). The parameterization of surface albedo for sea ice and its snow cover. *Progress in Physical Geography*, 20(1):63–79.
- Birnbaum, G., Dierking, W., Hartmann, J., Lüpkes, C., Ehrlich, A., Garbrecht, T., and Sellmann, M. (2009). The campaign meltex with research aircraft” polar 5” in the arctic in 2008. *Berichte zur Polar-und Meeresforschung (Reports on Polar and Marine Research)*, 593.
- Birnbaum, G., Ehrlich, A., Schwarz, P., Lüpkes, C., Dierking, W., and Hartmann, J. (2012). Aircraft observations of the evolution of ice surface conditions at the onset of the melt season in the beaufort sea. *AGU Fall Meeting, San Francisco*.

Carsey, F. (1985). Summer arctic sea ice character from satellite microwave data. *Journal of Geophysical Research*, 90(C3):5015–5034.

Carsey, F. D. (1992). *Microwave remote sensing of sea ice*, volume 68. American Geophysical Union.

Chernigovskiy, N. (1963). Radiational properties of the central arctic ice cover. *Trudy Arkticheskogo i Alztarkicheskogo Nauchno-Issledovatel'skogo Instituta*, 253:249–60.

Curry, J., Schramm, J., Alam, A., Reeder, R., Arbetter, T., and Guest, P. (2002). Evaluation of data sets used to force sea ice models in the arctic ocean. *Journal of Geophysical Research*, 107(C10):8027.

Derksen, C., Piwowar, J., and LeDrew, E. (1997). Sea-ice melt-pond fraction as determined from low level aerial photographs. *Arctic and Alpine Research*, pages 345–351.

DIGBY, S. A. (1985). Processes and imagery of first-year fast sea ice during the melt season. *Journal of Geophysical Research*, 90(C3):5045–5062.

Division, N. P. S. (2013). Image provided by the noaa/esrl physical sciences division, boulder colorado. *Digital Media*, <http://www.esrl.noaa.gov/psd/>.

Eicken, H. (1994). Structure of under-ice melt ponds in the central arctic and their effect on the sea-ice cover. *Limnology and oceanography*, pages 682–694.

El Naggar, S., Garrity, C., and Ramseier, R. (1998). The modelling of sea ice melt-water ponds for the high arctic using an airborne line scan camera, and applied to the satellite special sensor microwave/imager (ssm/i). *International Journal of Remote Sensing*, 19(12):2373–2394.

Fetterer, F., Wilds, S., and Sloan, J. (2008). Arctic sea ice melt pond statistics and maps, 1999–2001. *Digital Media (ftp)*, <http://nsidc.org/data/g02159.html>.

Friedl, M., McIver, D., Hodges, J., Zhang, X., Muchoney, D., Strahler, A., Woodcock, C., Gopal, S., Schneider, A., Cooper, A., et al. (2002). Global land cover mapping from modis: algorithms and early results. *Remote Sensing of Environment*, 83(1):287–302.

- Grenfell, T. and Maykutt, G. (1977). The optical properties of ice and snow in the arctic basin. *Journal of Glaciology*, 18(80).
- Grenfell, T. C. and Perovich, D. K. (1984). Spectral albedos of sea ice and incident solar irradiance in the southern beaufort sea. *Journal of Geophysical Research*, 89(C3):3573–3580.
- Hanesiak, J. M., Barber, D. G., De Abreu, R. A., and Yackel, J. J. (2001). Local and regional albedo observations of arctic first-year sea ice during melt ponding. *Journal of Geophysical Research: Oceans*, 106(C1):1005–1016.
- Hanson, A. M. (1965). Noctilucent clouds over the arctic in november. *Journal of Geophysical Research*, 70(18):4717–4718.
- Hanson, A. M. (1980). The snow cover of sea ice during the arctic ice dynamics joint experiment, 1975 to 1976. *Arctic and alpine research*, pages 215–226.
- Hildebrandt, G. (1996). *Fernerkundung und Luftbildmessung: Für Forstwirtschaft, Vegetationskartierung und Landschaftsökologie*. Wichmann.
- Imagine, E. (2012). Erdas imagine field guide. *ERDAS Inc., Atlanta, Georgia*.
- Inoue, J., Kikuchi, T., and Perovich, D. K. (2008). Effect of heat transmission through melt ponds and ice on melting during summer in the arctic ocean. *Journal of Geophysical Research: Oceans*, 113(C5).
- Jensen, J. (2008). *Introductory digital image processing: a remote sensing perspective*. Number Ed. 3. Prentice-Hall Inc.
- Krumpen, T. and Hendricks, S. (2010). Tifax hem campaign data report. Technical report, Alfred Wegener Institute for Polar and Marine Research.
- Langleben, M. (1969). Albedo and degree of puddling of a melting cover of sea ice. *Journal of Glaciology*, 8(54):407–412.
- Langleben, M. (1971). Albedo of remelting sea ice in the southern beaufort sea. *Journal of Glaciology*, 10(58).
- Lehmann, P. (2012). Geophysikalische messungen for nordostgrönland. Technical report, Alfred Wegener Institute for Polar and Marine Research.

- Lillesand, T. M., Kiefer, R. W., Chipman, J. W., et al. (2004). *Remote sensing and image interpretation*. Number Ed. 5. John Wiley & Sons Ltd.
- Lindsay, R. and Rothrock, D. (1993). The calculation of surface temperature and albedo of arctic sea ice from avhrr. *Annals of Glaciology*, 17:391–397.
- Lindsay, R. and Rothrock, D. (1994). Arctic sea ice albedo from avhrr. *Journal of Climate*, 7(11):1737–1749.
- Lüpkes, C., Gryanik, V. M., Hartmann, J., and Andreas, E. L. (2012). A parametrization, based on sea ice morphology, of the neutral atmospheric drag coefficients for weather prediction and climate models. *Journal of Geophysical Research: Atmospheres*, 117(D13).
- Markus, T., Cavalieri, D. J., Tschudi, M. A., and Ivanoff, A. (2003). Comparison of aerial video and landsat 7 data over ponded sea ice. *Remote Sensing of Environment*, 86(4):458–469.
- Maykut, G. A. and Grenfell, T. C. (1975). The spectral distribution of light beneath first-year sea ice in the arctic ocean. *Limnology and Oceanography*, pages 554–563.
- Maykut, G. A. and Perovich, D. K. (1987). The role of shortwave radiation in the summer decay of a sea ice cover. *Journal of Geophysical Research*, 92(C7):7032–7044.
- Mellor, M. (1965). Optical measurements on snow. Technical report, DTIC Document.
- Morasutti, M. P. and Ledrew, E. F. (1996). Albedo and depth of melt ponds on sea-ice. *International Journal of Climatology*, 16(7):817–838.
- Nadaraya, E. A. (1964). On estimating regression. *Theory of Probability & Its Applications*, 9(1):141–142.
- Nazintsev, Y. L. (1964). Some data on the calculation of thermal properties of sea ice. *Tr. Arkt. Antarkt. Nauchlo Issled Inst*, 267:31–47.
- Perovich, D., Roesler, C., and Pegau, W. (1998). Variability in arctic sea ice optical properties. *Journal of Geophysical Research*, 103(C1):1193–1208.

- Perovich, D., Tucker III, W., and Ligett, K. (2002a). Aerial observations of the evolution of ice surface conditions during summer. *Journal of Geophysical Research*, 107(C10):8048.
- Perovich, D. K. (1991). Seasonal changes in sea ice optical properties during fall freeze-up. *Cold regions science and technology*, 19(3):261–273.
- Perovich, D. K. (1993). A theoretical model of ultraviolet light transmission through antarctic sea ice. *Journal of geophysical research*, 98(C12):22579–22.
- Perovich, D. K. (1996). The optical properties of sea ice. Technical report, DTIC Document.
- Perovich, D. K., Grenfell, T. C., Light, B., and Hobbs, P. V. (2002b). Seasonal evolution of the albedo of multiyear arctic sea ice. *Journal of Geophysical Research: Oceans*, 107(C10).
- Perovich, D. K. and Maykut, G. A. (1990). Solar heating of a stratified ocean in the presence of a static ice cover. *Journal of Geophysical Research*, 95(C10):18233–18.
- Perovich, D. K. and Tucker III, W. B. (1997). Arctic sea-ice conditions and the distribution of solar radiation during summer. *Annals of Glaciology*, 25:445–450.
- Richard, M. (2012). Campaign : Surface heat budget of the arctic ocean (sheba). *Digital Media*, <http://www.arm.gov/campaigns/nsa1997sheba>.
- Robinson, D. A., Scharfen, G., Serreze, M. C., Kukla, G., and Barry, R. G. (1986). Snow melt and surface albedo in the arctic basin. *Geophysical research letters*, 13(9):945–948.
- Rösel, A. and Kaleschke, L. (2011). Comparison of different retrieval techniques for melt ponds on arctic sea ice from landsat and modis satellite data. *Annals of Glaciology*, 52(57):185–191.
- Rösel, A., Kaleschke, L., and Birnbaum, G. (2012). Exceptional melt pond occurrence in the years 2007 and 2011 on the arctic sea ice revealed from modis satellite data. *Journal of Geophysical Research: Oceans*, 117(C5).
- Rothrock, D. and Thorndike, A. (1984). Measuring the sea ice floe size distribution. *Journal of Geophysical Research*, 89(C4):6477–6486.

- Sankelo, P., Haapala, J., Heiler, I., and Rinne, E. (2010). Melt pond formation and temporal evolution at the drifting station tara during summer 2007. *Polar Research*, 29(3):311–321.
- Scharien, R. and Yackel, J. (2005). Analysis of surface roughness and morphology of first-year sea ice melt ponds: implications for microwave scattering. *Geoscience and Remote Sensing, IEEE Transactions on*, 43(12):2927 – 2939.
- Skyllingstad, E. D. and Paulson, C. A. (2007). A numerical study of melt ponds. *Collections*.
- Skyllingstad, E. D., Paulson, C. A., and Perovich, D. K. (2009). Simulation of melt pond evolution on level ice. *Journal of Geophysical Research: Oceans*, 114(C12).
- Steele, M. (1992). Sea ice melting and floe geometry in a simple ice-ocean model. *Journal of geophysical research*, 97(C11):17729–17.
- Taylor, P. D. and Feltham, D. L. (2004). A model of melt pond evolution on sea ice. *Journal of Geophysical Research: Oceans*, 109(C12).
- Tschudi, M. A., Curry, J. A., and Maslanik, J. (1997). Determination of areal surface-feature coverage in the beaufort sea using aircraft video data. *Annals of Glaciology*, 25:434–438.
- Tschudi, M. A., Curry, J. A., and Maslanik, J. A. (2001). Airborne observations of summertime surface features and their effect on surface albedo during fire/sheba. *Journal of Geophysical Research: Atmospheres*, 106(D14):15335–15344.
- Tschudi, M. A., Maslanik, J. A., and Perovich, D. K. (2008). Derivation of melt pond coverage on arctic sea ice using modis observations. *Remote Sensing of Environment*, 112(5):2605–2614.
- Tucker III, W., Gow, A., Meese, D., Bosworth, H., and Reimnitz, E. (1999). Physical characteristics of summer sea ice across the arctic ocean. *Journal of Geophysical Research*, 104(C1):1489–1504.
- Untersteiner, N. (1961a). Bemerkungen über die abkühlungsgrosse in den polargebieten. *Wetter und Leben*, 13(3-4):70–73.

- Untersteiner, N. (1961b). On the mass and heat budget of arctic sea ice. *Meteorology and Atmospheric Physics*, 12(2):151–182.
- Uttal, T., Curry, J. A., Mcphee, M. G., Perovich, D. K., Moritz, R. E., Maslanik, J. A., Guest, P. S., Stern, H. L., Moore, J. A., Turenne, R., et al. (2002). Surface heat budget of the arctic ocean. *Bulletin of the American Meteorological Society*, 83(2):255–275.
- Warren, S. G., Rigor, I. G., Untersteiner, N., Radionov, V. F., Bryazgin, N. N., Aleksandrov, Y. I., and Colony, R. (1999). Snow depth on arctic sea ice. *Journal of Climate*, 12(6):1814–1829.
- Wu, W. and Shao, G. (2002). Optimal combinations of data, classifiers, and sampling methods for accurate characterizations of deforestation. *Canadian Journal of Remote Sensing*, 28(4):601–609.
- Yackel, J. J. and Barber, D. G. (2000). Melt ponds on sea ice in the canadian archipelago: 2. on the use of radarsat-1 synthetic aperture radar for geophysical inversion. *Journal of Geophysical Research: Oceans*, 105(C9):22061–22070.
- Yackel, J. J., Barber, D. G., and Hanesiak, J. M. (2000). Melt ponds on sea ice in the canadian archipelago: 1. variability in morphological and radiative properties. *Journal of Geophysical Research: Oceans*, 105(C9):22049–22060.
- Zubov, N. (1945). Arctic ice. *Moskva, Izdatelstvo Glavsevmorputi*.







